Dipl.-Ing. Michael Rumetshofer

Quantum transport simulations of strongly correlated molecules

DOCTORAL THESIS

to achieve the university degree of

Doktor der Naturwissenschaften

submitted to

Graz University of Technology

Supervisor

Univ.-Prof. Dipl.-Phys. Dr.rer.nat. Wolfgang von der Linden

Institute of Theoretical and Computational Physics

Graz, October 2019

AFFIDAVIT

I declare that I have authored this thesis independently, that I have not used other than the declared sources/resources, and that I have explicitly indicated all material which has been quoted either literally or by content from the sources used. The text document uploaded to TUGRAZonline is identical to the present doctoral thesis.

Date

Signature

Abstract

Quantum transport simulations of single-molecule junctions offer the possibility to study very fundamental aspects of nonequilibrium many-body quantum physics and allow empirical confirmation due to sophisticated experimental techniques. State-of-the-art quantum transport simulation methods combine first-principle methods like density functional theory (DFT) with nonequilibrium Green's functions (NEGF). The DFT+NEGF method is well-established but strongly correlated molecules require a proper many-body treatment within, e.g., the Anderson impurity model (AIM) embedded in a noninteracting environment describing the residual system.

In this thesis, we apply the DFT+NEGF method with an embedded AIM to the benzenedithiolate (BDT) molecule contacted with monoatomic Au and Pt electrodes and the copper phthalocyanine (CuPc) molecule adsorbed on Ag(111) and Au(111). In the BDT system, we find that the conductance mechanism differs for Au and Pt electrodes due to symmetry. At the model level, we present the charge stability diagram for the BDT contacted with monoatomic Pt electrodes and discuss how monoatomic electrodes and many-body effects influence the transport properties. We successfully describe CuPc on Ag(111) with a three-orbital AIM problem that can be simplified into a two-orbital problem coupled to the localized spin of the third orbital. This results in a Kondo effect with a mixed character, displaying a symmetry between SU(2) and SU(4). While in CuPc on Ag(111) the computed Kondo temperature is in agreement with experimental values, in CuPc on Au(111) the Kondo temperature is far to low to see the Kondo effect in an experiment. We find that the transport properties depend on the detailed position of the scanning tunneling microscope tip above the CuPc molecule in good agreement with differential conductance measurements.

In quantum transport simulations of strongly correlated molecules, solving the many-body problem requires special numerical methods, as e.g. quantum Monte Carlo (QMC) which produces noisy imaginary-time Green's function data. Analytic continuation and Fourier transformation lead to the frequency-dependent Green's function needed in the NEGF method to calculate transport properties. We propose Bayesian parametric analytic continuation (BPAC) for solving this *ill-posed* inversion problem. In BPAC, the spectral function is inferred from a suitable set of parametrized basis functions and Bayesian model comparison allows to assess the reliability of different parametrizations. Compared to methods routinely used for the analytic continuation of QMC data, BPAC allows to infer whether the data support specific structures of the spectral function, which was especially important for solving the AIM describing CuPc on Ag(111).

Kurzfassung

Simulationen von Quantentransport über einzelne Moleküle bieten die Möglichkeit grundlegende Aspekte der Vielteilchen-Quantenphysik im Nichtgleichgewicht zu erforschen und erlauben eine empirische Bestätigung aufgrund moderner experimenteller Techniken. Aktuelle Methoden für die Simulation von Quantentransport kombinieren *ab initio* Methoden wie die Dichtefunktionaltheorie (DFT) mit Nichtgleichgewichts-Green-Funktionen (NEGF). Die DFT+NEGF-Methode ist etabliert, aber stark korrelierte Moleküle erfordern eine entsprechende Vielteilchenbehandlung, z.B. im Rahmen des Anderson-Impurity-Modells (AIM) eingebettet in eine nicht wechselwirkende Umgebung die das Restsystem beschreibt.

In dieser Arbeit wenden wir die DFT+NEGF-Methode mit eingebettetem AIM auf das Benzenedithiolate (BDT) Molekül kontaktiert mit einatomigen Au- und Pt-Elektroden und auf das Kupferphthalocyanin (CuPc) Molekül adsorbiert auf Ag(111) und Au(111) an. Im BDT-System stellen wir fest, dass sich der Leitfähigkeitsmechanismus für Au- und Pt-Elektroden aufgrund der Symmetrie unterscheidet. Auf Modellebene präsentieren wir das Ladungsstabilitätsdiagramm für BDT kontaktiert mit einatomigen Pt-Elektroden und diskutieren, wie einatomige Elektroden und Vielteilcheneffekte die Transporteigenschaften beeinflussen. Wir beschreiben CuPc auf Ag(111) erfolgreich mit einem Drei-Orbital-AIM welches in ein Zwei-Orbital-Problem, gekoppelt an den lokalisierten Spin des dritten Orbitals, vereinfacht werden kann. Dies führt zu einem Kondo-Effekt mit gemischtem Charakter, der eine Symmetrie zwischen SU(2) und SU(4) zeigt. Während in CuPc auf Ag(111) die berechnete Kondo-Temperatur mit experimentellen Werten übereinstimmt, ist in CuPc auf Au(111) die Kondo-Temperatur zu niedrig, um den Kondo-Effekt im Experiment beobachten zu können. In guter Übereinstimmung mit Messungen der differentiellen Leitfähigkeit stellen wir fest, dass die Transporteigenschaften von der detaillierten Position der Spitze des Rastertunnelmikroskops abhängen.

Bei der Simulation von Quantentransport über stark korrelierte Moleküle erfordert die Lösung des AIM spezielle numerische Methoden, wie z.B. Quanten-Monte-Carlo (QMC) Algorithmen, welche Green'sche Funktionen statistisch exakt in imaginärer Zeit berechnen. Analytische Fortsetzung und Fouriertransformation führen zu der frequenzabhängigen Green'schen Funktion, die in der NEGF-Methode zur Berechnung von Transporteigenschaften benötigt wird. Um dieses *schlecht gestellte* Inversionsproblem zu lösen, entwickeln wir die Bayes'sche parametrische analytische Fortsetzung (BPAC). In BPAC wird die Spektralfunktion mit einem geeigneten Satz parametrisierter Basisfunktionen dargestellt und Bayes'scher Modellvergleich erlaubt die Beurteilung verschiedener Parametrisierungen. Im Vergleich zu Methoden, die üblicherweise für die analytische Fortsetzung von QMC-Daten verwendet werden, erlaubt BPAC den Rückschluss, ob die QMC-Daten bestimmte Strukturen der Spektralfunktion unterstützen, was besonders für die Lösung des AIM, das CuPc auf Ag(111) beschreibt, wichtig war.

Acknowledgements

I would like to thank *Wolfgang von der Linden* for giving me the opportunity to do my PhD thesis in his group and for making himself available whenever I needed help. I am particularly thankful that I had the freedom to choose my main emphases and for the chance to participate in all the schools and conferences.

My sincere gratitude goes to *Markus Aichhorn* and *Enrico Arrigoni* for answering almost any question concerning many-body physics. A big thank you goes to *Daniel Bauernfeind*, *Gernot Kraberger* and *Robert Triebl* for discussing different perspectives on physics, life and everything. *Gernot Kraberger* came up with the idea of studying molecules well-known by colleagues at the *Institute of Solid State Physics*, especially by *Elisabeth Wruß*.

Thank you, all the members of the *Institute of Theoretical Physics* but especially *Gerhard Dorn*, *Lukas Bauer*, *Michael Eder*, *Viktor Eisler*, *Delia Fugger*, *Johanna Ganglbauer*, *Johannes Graspeuntner*, *Matthias Gruber*, *Florian Maislinger*, *Markus Richter*, *Franz Rohrhofer*, *Max Sorantin* and *Irakli Titvinitze* for the friendly working environment and entertaining lunch breaks. I also like to thank the very motivated students *Georg Elsinger*, *Andrei-Viorel Man* and *Fabian Klingberg* in whose bachelor thesis and master theses, respectively, I had the chance to be involved.

Especially I would like to thank *Pascal Heim*, *Markus Koch*, *Sascha Ranftl* and *Bernhard Thaler* for being part of our Bayesian task force for analyzing data of the femtosecond pump-probe photoelectron-photoion coincidence experiments performed at the *Institute of Experimental Physics*. Although this analysis could not be part of my written thesis, I am very glad for having been involved in this project.

I would also like to thank our system administrator *Andreas Hirczy* for solving my computational issues and our secretary *Brigitte Schwarz* for helping with bureaucratic work.

Thanks go to my friends *Markus Bainschab*, *Alexander Betzler*, *Michael Draxler*, *Fabian Huber*, *Paul Maierhofer*, *Ralf Meyer*, *Peter Pichler*, *Alexander Schiffmann*, *Alexander Schossmann* and *Leonhard Treiber* for motivating me to do a good job at work and for the exchange of ideas at our *Stammtische* and coffee breaks.

Special thanks go to my parents *Maria and Konrad Rumetshofer* for supporting me all the time. Thank you, *Johannes Rumetshofer*, for the many discussions about everything and anything. Last but not least I want to thank my girlfriend *Monika Hagauer* for her love and for pointing to the really essential in many situations.

Contents

Chapter 1

Introduction

Quantum transport simulations of single-molecule junctions are a fascinating topic of modern theoretical physics offering the possibility to study very fundamental aspects of nonequilibrium many-body quantum physics. Rapidly developing fields like *Nanoelectronics* and *Molecular electronics* [1–6] attempt to answer the question whether single molecules have a perspective as active elements in technological applications. Many transport phenomena attracted the scientist's attention, e.g., negative differential conductance, transistor- or diode-like behavior, quantum interference, Coulomb blockade, and the Kondo effect. Increasing research interest is due to progress in both, experimental techniques, allowing unprecedented control over single-molecule junctions, and numerical techniques, aiming to perform transport simulations from first principles. Challenges for quantum transport simulations are providing deep understanding of fundamental transport phenomena and improving numerical techniques to increase computable system sizes and to achieve predictive power for designing new experiments and electronic devices.

State-of-the-art quantum transport simulation methods combine first-principle methods, such as density functional theory (DFT) [7], with nonequilibrium Green's functions (NEGF) [8, 9]. The so-called DFT+NEGF method is well-established for quantum transport simulations of molecules well-described in an effective one-particle picture; strongly correlated molecules require a proper many-body treatment by resorting to methods going beyond DFT, e.g. by combining GW [10], which captures correlations only up to some extent, or dynamical mean field theory (DMFT) [11] with NEGF. In quantum dot experiments, where the central part of the transport system is weakly coupled to electrodes and electron correlations play a crucial role, master equation (ME) [12] approaches became advantageous over the NEGF method. The approach used in this thesis is based on the DFT+NEGF method but the strongly correlated parts of the transport system are described within an Anderson impurity model (AIM) [13] embedded in the noninteracting environment describing the residual system. The present thesis has two main focuses: First, we apply this DMFT-like approach to benzenedithiolate (BDT) contacted with monoatomic Au and Pt electrodes and to the copper phthalocyanine (CuPc) molecule adsorbed on Au(111) and Ag(111). Secondly, we propose a new method for the analytical continuation of noisy imaginary-time Green's function data, as e.g. produced

by continuous-time quantum Monte Carlo (CTQMC) [14] when solving an AIM. More details are given in the following paragraphs.

Although BDT became a benchmark molecule for quantum transport simulations, there always have been undeniable differences between experiment [15–21] and theory [22–24]; the reasons remained controversial [25–30]. Motivated by this, we study BDT contacted with monoatomic Au and Pt electrodes by employing DFT and using maximally localized Wannier functions (MLWF) [31, 32] to set up the transport Hamiltonian. The monoatomic electrodes allow to perform the Wannier transformation in a very controlled way and we can explain why the conductance mechanism is different for Au and Pt electrodes using symmetry arguments. We consider the BDT molecule as a multi-orbital AIM and solve the impurity problem within cluster perturbation theory (CPT) [33]. At the model level, we present the charge stability diagram for the BDT contacted with monoatomic Pt electrodes and discuss how low-dimensional electrodes and many-body effects influence the transport properties.

One of the cooperative many-body phenomena in solid state physics, the Kondo effect [34–37], receives increasing attention due to observation in scanning tunneling microscope (STM) experiments [38–40], e.g. in CuPc adsorbed on metal surfaces [41–44]. In this thesis, we study CuPc adsorbed on Au(111) and Ag(111) by employing DFT and the projection scheme suggested by Droghetti *et al.* [45] along with some modifications. In concerning CuPc adsorbed on Au(111) and Ag(111) surfaces, the CuPc molecule has essentially three localized orbitals close to the Fermi energy resulting in strong local Coulomb repulsion not accounted for properly in DFT calculations. The occupancy of these orbitals varies with the substrate on which CuPc is adsorbed. While correlation effects in CuPc on Au(111) are already properly described by a single-orbital AIM, for CuPc on Ag(111) the three-orbital AIM problem can be simplified into a two-orbital problem coupled to the localized spin of the third orbital. This results in a Kondo effect with a mixed character, displaying a symmetry between SU(2) and SU(4). The computed Kondo temperature is in agreement with experimental values. To solve the impurity problem, we use the recently developed fork tensor product state (FTPS) solver [46–48]. To obtain transport properties, an STM tip is added to the CuPc molecule absorbed on the surface. We find that the transmission depends on the detailed position of the STM tip above the CuPc molecule in good agreement with differential conductance measurements.

There exist various methods for solving the AIM; we already mentioned CPT and the FTPS solver. In contrast to these methods, CTQMC is an impurity solver working on the imaginary-time axis. The computed imaginary-time Green's function is related to the spectral function by a Laplace transform, the so-called analytic continuation. In this thesis, we propose Bayesian parametric analytic continuation (BPAC) where the spectral function is inferred from a suitable set of parametrized basis functions. BPAC is completely based on Bayesian probability theory [49–52] where Bayesian model comparison allows to assess the reliability of different parametrizations. The required evidence integrals of such a model comparison can be determined by employing methods like thermodynamic integration (TI) [53, 54] or nested sampling (NESA) [55]. Compared to the maximum entropy method (MEM) [56], routinely used for the analytic continuation of CTQMC data, the presented approach allows to infer

whether the data support specific structures of the spectral function. We demonstrate the capability of BPAC in terms of CTQMC data for an AIM closely related to the AIM of CuPc on Ag(111) and compare the BPAC reconstruction to the MEM, as well as to the spectral function obtained from the real-time FTPS impurity solver where no analytic continuation is required. Further, we present a combination of MEM and BPAC and its application to an AIM arising from the *ab initio* treatment of $SrVO_3$.

The content of this thesis is structured as follows. In Chpt. 2, we provide an overview of the theory used in quantum transport simulations and based on DFT and NEGF with special emphasis on the treatment of strong electron correlations. We would like to emphasize that the theoretical concepts presented in Chpt. 2 are common knowledge. We have nevertheless summarized them because they are important for understanding Chpts. 3, 4 and 5 which are the core of the present thesis. We present quantum transport simulations for BDT contacted with monoatomic Au and Pt electrodes in Chpt. 3 and for CuPc adsorbed on Au(111) and Ag(111) in Chpt. 4. In Chpt. 5, we propose BPAC as a new method for the analytic continuation of noisy imaginary-time Green's function data.

Chapter 2

Theoretical concepts

This chapter provides an overview of the theoretical concepts used in quantum transport simulations based on density functional theory (DFT) and nonequilibrium Green's functions (NEGF) with special emphasis on the treatment of strong electron correlations. While Sec. 2.1 gives a brief introduction to quantum transport simulations based on NEGF, Sec. 2.2 discusses the most commonly used first-principle method, DFT, and its combination with NEGF. The description of strongly correlated parts of the transport system with an Anderson impurity model (AIM) is discussed in Sec. 2.3. Because of its importance for strongly correlated molecules, Sec. 2.4 introduces one of the cooperative many-body phenomena, the Kondo effect. We would like to emphasize that the theoretical concepts presented in the present chapter are common knowledge; for instance, the theory of quantum transport is explained in detail in Refs. [1–4] and Refs. [57–61] are comprehensive books concerning many-body physics. Therefore, unless another reference is explicitly given, we refer to one of these books.

2.1 Nonequilibrium Green's functions

Green's functions are a convenient tool to solve linear differential equations, as e.g. the Schrödinger equation. Especially, NEGF are the basic tool in quantum transport simulations giving access to many transport properties, e.g., current, transmission, and differential conductance. The present section gives a brief introduction to the topic.

While Sec. 2.1.1 defines a very general Hamiltonian describing a quantum transport system, Sec. 2.1.2 briefly introduces NEGF for solving the Schrödinger equation in terms of the Keldysh formalism. Sec. 2.1.3 works out the connection between Green's functions and quantum transport and Secs. 2.1.4 and 2.1.5 introduce methods for calculating Green's functions. Formulas for calculating the current, the transmission, and the differential conductance are introduced in Secs. 2.1.6 and 2.1.7.

2.1.1 The Hamiltonian

The underlying equation for charge quantum transport simulations is the Schrödinger equation being a linear partial differential equation that describes the wave function of a quantum-mechanical system. In this section, we ignore time-dependency, and therefore, have

$$\hat{H}\Phi(\mathbf{r}_1, ..., \mathbf{r}_N) = E\Phi(\mathbf{r}_1, ..., \mathbf{r}_N) \tag{2.1.1}$$

although we discuss several aspects of time-dependency in Sec. 2.1.2. The many-particle wave function $\Phi(\mathbf{r}_1, ..., \mathbf{r}_N)$ depends on the coordinates of the N electrons. In assuming that the motion of atomic nuclei and electrons can be separated, the so-called Born-Oppenheimer approximation, and that the $N_\mathbf{R}$ nuclei positions $\{\mathbf{R}_j\}$ are fixed, the fully interacting Hamiltonian is

Hamiltonian:

$$\hat{H} = \left(\sum_{i=1}^{N} \left(-\frac{\hbar^2}{2m}\Delta_i + V(\mathbf{r}_i) \right) + \frac{1}{2} \sum_{\substack{i,j=1 \\ i \neq j}}^{N} U(\mathbf{r}_i, \mathbf{r}_j) \right) \tag{2.1.2}$$

with

$$V(\mathbf{r}_i) = -\frac{e^2}{4\pi\epsilon} \sum_{j=1}^{N_\mathbf{R}} \frac{Z_j}{|\mathbf{r}_i - \mathbf{R}_j|} \quad \text{and} \quad U(\mathbf{r}_i, \mathbf{r}_j) = \frac{e^2}{4\pi\epsilon} \frac{1}{|\mathbf{r}_i - \mathbf{r}_j|} \ .$$

$V(\mathbf{r}_i)$ is the one-particle potential energy for the ith particle and $U(\mathbf{r}_i, \mathbf{r}_j)$ is the interaction energy between the ith and the jth particle. By introducing the quantum field operators $\hat{\Psi}(\mathbf{r})$ and $\hat{\Psi}^\dagger(\mathbf{r})$, the Hamiltonian can be rewritten to $\hat{H} = \hat{T} + \hat{U}$ with

$$\begin{aligned} \hat{T} &= \int d^3r \ \hat{\Psi}^\dagger(\mathbf{r}) \left(-\frac{\hbar^2}{2m}\Delta + V(\mathbf{r}) \right) \hat{\Psi}(\mathbf{r}) \\ \hat{U} &= \frac{1}{2} \int d^3r \int d^3r' \ U(\mathbf{r}, \mathbf{r}') \hat{\Psi}^\dagger(\mathbf{r}) \hat{\Psi}^\dagger(\mathbf{r}') \hat{\Psi}(\mathbf{r}') \hat{\Psi}(\mathbf{r}) \ . \end{aligned} \tag{2.1.3}$$

$\hat{T}$ is the one-particle part including kinetics and a potential term and $\hat{U}$ is the interaction part accounting for the Coulomb repulsion between the electrons. Employing an orthonormal basis set spanned by the basis functions $\{\Psi_i(\mathbf{r})\}$, the field operators are defined by

$$\hat{\Psi}^\dagger(\mathbf{r}) := \sum_i \Psi_i^*(\mathbf{r}) \hat{a}_i^\dagger \quad \text{and} \quad \hat{\Psi}(\mathbf{r}) := \sum_i \Psi_i(\mathbf{r}) \hat{a}_i \ . \tag{2.1.4}$$

The operators $\hat{a}_i^\dagger$ and $\hat{a}_i$ denote creation and annihilation of particles in the quantum state described by the basis function $\Psi_i(\mathbf{r})$. Inserting these definitions of the field operators into Eq. 2.1.3 produces the convenient Hamiltonian in second quantization.

Hamiltonian (second quantization):

$$\hat{H} = \hat{T} + \hat{U} = \sum_{ij} t_{ij} \hat{a}_i^\dagger \hat{a}_j + \frac{1}{2} \sum_{ijkl} \tilde{U}_{ijkl} \hat{a}_i^\dagger \hat{a}_j^\dagger \hat{a}_k \hat{a}_l \tag{2.1.5}$$

with the parameters

$$t_{ij} = \int d^3r \; \Psi_i^*(\mathbf{r}) \left(-\frac{\hbar^2}{2m} \Delta + V(\mathbf{r}) \right) \Psi_j(\mathbf{r})$$
$$\tilde{U}_{ijkl} = \int d^3r \int d^3r' \; U(\mathbf{r}, \mathbf{r}') \Psi_i^*(\mathbf{r}) \Psi_j^*(\mathbf{r}') \Psi_k(\mathbf{r}') \Psi_l(\mathbf{r}) \; .$$

The determination of the parameters t_{ij} and $\tilde{U}_{ijkl}$ for realistic quantum transport systems from first principles is a long and difficult road and discussed in Secs. 2.2 and 2.3. In this thesis, we restrict ourselves in the interaction part of Eq. 2.1.5 to density-density terms only, and therefore,

$$\hat{U} = \frac{1}{2} \sum_{ij} U_{ij} \hat{n}_i \hat{n}_j \tag{2.1.6}$$

with

$$U_{ij} = \int d^3r \int d^3r' \; U(\mathbf{r}, \mathbf{r}') |\Psi_i(\mathbf{r})|^2 |\Psi_j(\mathbf{r}')|^2 \; .$$

This restriction is justified if non-density-density terms are negligible which requires that the orbitals are maximally localized.

Before introducing the Green's function formalism for solving the Hamiltonian, we briefly want to discuss important consequences of orthogonal and nonorthogonal basis systems. In the fermionic case, the field operators obey the canonical commutation relations

$$\{\hat{\Psi}(\mathbf{r}), \hat{\Psi}(\mathbf{r}')\} = \{\hat{\Psi}^\dagger(\mathbf{r}), \hat{\Psi}^\dagger(\mathbf{r}')\} = 0 \quad \text{and} \quad \{\hat{\Psi}(\mathbf{r}), \hat{\Psi}^\dagger(\mathbf{r}')\} = \delta(\mathbf{r} - \mathbf{r}') \tag{2.1.7}$$

which induce for the orthonormal basis defined in Eq. 2.1.4 the commutation relations

$$\{\hat{a}_i, \hat{a}_j\} = \{\hat{a}_i^\dagger, \hat{a}_j^\dagger\} = 0 \quad \text{and} \quad \{\hat{a}_i, \hat{a}_j^\dagger\} = \delta_{ij} \; . \tag{2.1.8}$$

These commutation relations change in the case of a nonorthogonal basis set. We refer to Refs. [62–65] for a comprehensive introduction to nonorthogonal basis sets in quantum transport simulations. Analogue to Eq. 2.1.4, we expand the field operators in the complete set of basis functions with the difference that now the basis functions $\{\varphi_i(\mathbf{r})\}$ are nonorthonormal and described by the symmetric overlap matrix

$$S_{ij} = \int d^3r \; \varphi_i(\mathbf{r}) \varphi_j^*(\mathbf{r}) \; . \tag{2.1.9}$$

The field operators in this nonorthonormal basis are defined by

$$\hat{\Psi}^\dagger(\mathbf{r}) := \sum_i \varphi_i^*(\mathbf{r}) \hat{b}_i^\dagger \quad \text{and} \quad \hat{\Psi}(\mathbf{r}) := \sum_i \varphi_i(\mathbf{r}) \hat{b}_i \tag{2.1.10}$$

where now the new operators $\hat{b}_i^\dagger$ and $\hat{b}_i$ denote creation and annihilation of particles in the quantum state described by the nonorthonormal basis function $\varphi_i(\mathbf{r})$. Hence, the commutation relations for the nonorthonormal basis are

$$\{\hat{b}_i, \hat{b}_j\} = \{\hat{b}_i^\dagger, \hat{b}_j^\dagger\} = 0 \quad \text{and} \quad \{\hat{b}_i, \hat{b}_j^\dagger\} = \left(S^{-1}\right)_{ij} \tag{2.1.11}$$

and can be proved by inserting the definitions of the field operators into the canonical commutation relations Eq. 2.1.7. Unless explicitly stated, we restrict ourselves to orthonormal basis systems in the following.

2.1.2 The Keldysh formalism

Originally, the Keldysh formalism was independently derived by Kadanoff and Baym [8] and Keldysh [9]. As an important result, the Keldysh formalism allows a systematic perturbative approach to derive NEGF. We won't discuss diagrammatic techniques in the present thesis but refer to the Refs. [57, 59, 66] for a comprehensive introduction.

We consider a transport system described by the Hamiltonian

$$\hat{H}(t) = \hat{T} + \underbrace{\hat{U} + \hat{h}(t)}_{\hat{V}(t)} \; . \tag{2.1.12}$$

In comparison to Hamiltonian 2.1.5, we introduce a time-dependent perturbation $\hat{h}(t)$ which drives the system out of equilibrium, e.g. by shifts in the chemical potential in the electrodes of a transport system. For the next step, we split Hamiltonian 2.1.12 into two parts: the unperturbed Hamiltonian $\hat{T}$, and the perturbation $\hat{V}(t)$ including both, the interaction part and the time-dependent perturbation. In quantum mechanics, the time evolution generated by the Hamiltonian can either be done in the states (Schrödinger picture) or in the operators (Heisenberg picture (H)). The Dirac picture, also called interaction representation (I), is an intermediate representation where only the time evolution of $\hat{T}$ is done in the operators; the time evolution of the typically more involved part $\hat{V}(t)$ is done in the states. The time-evolution operator

$$\hat{S}_\mathrm{I}(t_1, t_0) = \mathcal{T} e^{-\mathrm{i}\int_{t_0}^{t_1} dt\, \hat{V}_\mathrm{I}(t)} \tag{2.1.13}$$

is an exponential representation of the Dyson series and connects states at different times t_0 and t_1 in the interaction representation. $\mathcal{T}$ denotes the time-ordering operator which is defined as

$$\mathcal{T}\hat{A}(t_1)\hat{B}(t_2) := \begin{cases} \hat{A}(t_1)\hat{B}(t_2), & t_1 > t_2 \\ -\hat{B}(t_2)\hat{A}(t_1), & t_2 > t_1 \end{cases} \; . \tag{2.1.14}$$

where the sign accounts for fermionic operators. For the time-evolution operator the relations

$$\begin{aligned} &\hat{S}_\mathrm{I}(t_0, t_0) = 1 \\ &\hat{S}_\mathrm{I}(t_1, t_0) = \hat{S}_\mathrm{I}^{-1}(t_0, t_1) = \hat{S}_\mathrm{I}^\dagger(t_0, t_1) \\ &\hat{S}_\mathrm{I}(t_2, t_0) = \hat{S}_\mathrm{I}(t_2, t_1)\hat{S}_\mathrm{I}(t_1, t_0) \end{aligned} \tag{2.1.15}$$

hold.

Furthermore, we define the time-ordered Green's function, also called causal Green's function, by

$$G^{\mathcal{T}}_{\hat{A}\hat{B}}(t_1,t_2) := -\mathrm{i}\frac{\langle\Psi_\mathrm{H}|\,\mathcal{T}\hat{A}_\mathrm{H}(t_1)\hat{B}_\mathrm{H}(t_2)\,|\Psi_\mathrm{H}\rangle}{\langle\Psi_\mathrm{H}|\Psi_\mathrm{H}\rangle}\,. \tag{2.1.16}$$

In using this definition, we restrict ourselves to zero temperature. Let us first consider a system in equilibrium, and therefore $\hat{h}(t)=0$, in which the interaction part $\hat{U}$ is switched on and off adiabatically, $\hat{U}\to\hat{U}(t)=\hat{U}e^{-0^+|t|}$, and therefore, there is no interaction for $t\to\pm\infty$ and the interaction attains its full strength at $t=0$. Hence, at $t=\pm\infty$ the perturbation $\hat{V}(t)$ vanishes and the system is in the unperturbed ground state $|\Phi_0\rangle$ of $\hat{T}$, whereas at $t=0$ we have $|\Psi_\mathrm{H}\rangle=\hat{S}_\mathrm{I}(0,-\infty)\,|\Phi_0\rangle$. This procedure is not completely well-defined, since the Gell-Mann and Low theorem states that the evolution of the ground state from $-\infty$ to 0 acquires a phase, see Ref. [60] for details. But these phase factors cancel for expectation values like the Green's function, and we obtain

Time-ordered Green's function (equilibrium):

$$G^{\mathcal{T}}_{\hat{A}\hat{B}}(t_1,t_2) = -\mathrm{i}\frac{\langle\Phi_0|\,\mathcal{T}\hat{A}_\mathrm{I}(t_1)\hat{B}_\mathrm{I}(t_2)\hat{S}_\mathrm{I}(\infty,-\infty)\,|\Phi_0\rangle}{\langle\Phi_0|\,\hat{S}_\mathrm{I}(\infty,-\infty)\,|\Phi_0\rangle} \tag{2.1.17}$$

where we used $\hat{X}_\mathrm{H}(t)=\hat{S}_\mathrm{I}(0,t)\hat{X}_\mathrm{I}(t)\hat{S}_\mathrm{I}(t,0)$, the time-ordering property of $\mathcal{T}$, and the properties of $\hat{S}_\mathrm{I}$ listed in Eqs. 2.1.15. A systematic perturbative scheme for calculating the Green's function in terms of Feynman diagrams can be obtained by expanding $\hat{S}_\mathrm{I}(\infty,-\infty)$.

In the nonequilibrium case, we use the adiabatic hypothesis for the interaction part as in equilibrium and assume additionally that $\hat{h}(t)$ is switched on at time t_0. We take the limit $t_0\to-\infty$ at the end of the calculation to account for $\hat{h}(t)$ at every finite time t. Due to switching on $\hat{h}(t)$ at time t_0, the system is in the ground state $|\Phi_0\rangle$ only at $t=-\infty$ but not anymore at $t=\infty$. Since this symmetry is broken, the time-ordered Green's function has to be written as

$$G^{\mathcal{T}}_{\hat{A}\hat{B}}(t_1,t_2) = -\mathrm{i}\frac{\langle\Phi_0|\,\hat{S}_\mathrm{I}(-\infty,\infty)\mathcal{T}\hat{A}_\mathrm{I}(t_1)\hat{B}_\mathrm{I}(t_2)\hat{S}_\mathrm{I}(\infty,-\infty)\,|\Phi_0\rangle}{\langle\Phi_0|\,\hat{S}_\mathrm{I}(-\infty,\infty)\hat{S}_\mathrm{I}(\infty,-\infty)\,|\Phi_0\rangle}\,. \tag{2.1.18}$$

Keldysh showed that one can still order the time arguments along a modified time contour $\tau_i=\{t_i,c_i\}$ where in addition to the time, the side of the contour $c_i\in\{+,-\}$ has to be specified, see Fig. 2.1.

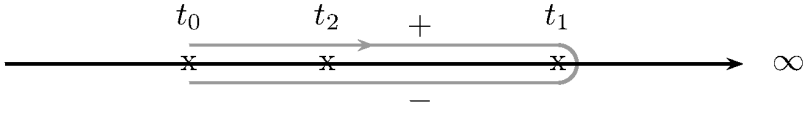

Figure 2.1: The Keldysh contour (gray line).

In analogy to the time-ordering operator $\mathcal{T}$, we define the contour-ordering operator $\mathcal{T}_\mathrm{c}$ which orders along a given contour, e.g. the Keldysh contour. In using the evolution operator

$$\hat{S}_\mathrm{I}^\mathrm{c}(\infty,-\infty) = \mathcal{T}_\mathrm{c} e^{-\mathrm{i}\int_\mathrm{c} d\tau\, \hat{V}_\mathrm{I}(\tau)} \tag{2.1.19}$$

we have

Contour-ordered Green's function:

$$G_{\hat{A}\hat{B}}^{\mathcal{T}_\mathrm{c}}(\tau_1,\tau_2) = -\mathrm{i}\frac{\langle\Phi_0|\,\mathcal{T}_\mathrm{c}\,\hat{A}_\mathrm{I}(\tau_1)\hat{B}_\mathrm{I}(\tau_2)\hat{S}_\mathrm{I}^\mathrm{c}(\infty,-\infty)\,|\Phi_0\rangle}{\langle\Phi_0|\,\hat{S}_\mathrm{I}^\mathrm{c}(\infty,-\infty)\,|\Phi_0\rangle} \tag{2.1.20}$$

in analogy to the equilibrium case in Eq. 2.1.17 but taking into account contour ordering rather than time ordering. Depending on the order along the contour, four different Green's functions are generated and defined as

$$\begin{aligned}
G_{ij}^{\mathcal{T}}(t,t') &:= G_{\hat{a}_i\hat{a}_j^\dagger}^{\mathcal{T}_\mathrm{c}}(\{t,+\},\{t',+\}) &&= -\mathrm{i}\left\langle \mathcal{T}\left\{\hat{a}_i(t)\hat{a}_j^\dagger(t')\right\}\right\rangle && \text{time-ordered,}\\
G_{ij}^{>}(t,t') &:= G_{\hat{a}_i\hat{a}_j^\dagger}^{\mathcal{T}_\mathrm{c}}(\{t,+\},\{t',-\}) &&= -\mathrm{i}\left\langle \hat{a}_i(t)\hat{a}_j^\dagger(t')\right\rangle && \text{greater,}\\
G_{ij}^{<}(t,t') &:= G_{\hat{a}_i\hat{a}_j^\dagger}^{\mathcal{T}_\mathrm{c}}(\{t,-\},\{t',+\}) &&= \mathrm{i}\left\langle \hat{a}_j^\dagger(t')\hat{a}_i(t)\right\rangle && \text{lesser,}\\
G_{ij}^{\bar{\mathcal{T}}}(t,t') &:= G_{\hat{a}_i\hat{a}_j^\dagger}^{\mathcal{T}_\mathrm{c}}(\{t,-\},\{t',-\}) &&= -\mathrm{i}\left\langle \bar{\mathcal{T}}\left\{\hat{a}_i(t)\hat{a}_j^\dagger(t')\right\}\right\rangle && \text{and anti-time-ordered.}
\end{aligned} \tag{2.1.21}$$

Here, we already used annihilation and creation operators $\hat{a}_i$ and $\hat{a}_j^\dagger$ as the operators $\hat{A}$ and $\hat{B}$, respectively. These four Green's functions are linearly dependent due to

$$\begin{aligned}
G^\mathrm{k} &:= G^{>} + G^{<} = G^{\mathcal{T}} + G^{\bar{\mathcal{T}}}\\
G^\mathrm{r} &:= G^{\mathcal{T}} - G^{<} = G^{>} - G^{\bar{\mathcal{T}}}\\
G^\mathrm{a} &:= G^{\mathcal{T}} - G^{>} = G^{<} - G^{\bar{\mathcal{T}}}
\end{aligned} \tag{2.1.22}$$

where we suppressed the time arguments for the sake of readability. G^k is called the Keldysh, G^r the retarded, and G^a the advanced Green's function. According to Eqs. 2.1.22, the retarded and the advanced Green's function are given by

$$\begin{aligned}
G_{ij}^\mathrm{r}(t,t') &= G_{\hat{a}_i\hat{a}_j^\dagger}^\mathrm{r}(t,t') = -\mathrm{i}\theta(t-t')\left\langle\left\{\hat{a}_i(t),\hat{a}_j^\dagger(t')\right\}\right\rangle\\
G_{ij}^\mathrm{a}(t,t') &= G_{\hat{a}_i\hat{a}_j^\dagger}^\mathrm{a}(t,t') = \mathrm{i}\theta(t'-t)\left\langle\left\{\hat{a}_i(t),\hat{a}_j^\dagger(t')\right\}\right\rangle
\end{aligned} \tag{2.1.23}$$

where the curly brackets denote the anticommutator, $\{\hat{A},\hat{B}\} = \hat{A}\hat{B}+\hat{B}\hat{A}$. If the Hamiltonian does not depend explicitly on the time, the Green's functions depend only on the time difference $(t-t')$. This is the case with the stationary solutions in which we are exclusively interested, and hence, we can Fourier transform the Green's functions defined so far. It turns

out that the retarded and the advanced Green's function, respectively, contain properties like the spectrum

$$A_{ij}(\omega) := \frac{\mathrm{i}}{2\pi}\left(G^{\mathrm{r}}_{ij}(\omega) - G^{\mathrm{a}}_{ij}(\omega)\right) \tag{2.1.24}$$

and level broadening, while the Keldysh Green's function describes kinetic properties, e.g., distribution function, charge, and current. Therefore, it is advantageous to define Keldysh space in terms of a 2×2 matrix structure:

$$\mathbf{G} := \begin{pmatrix} G^{\mathrm{r}} & G^{\mathrm{k}} \\ 0 & G^{\mathrm{a}} \end{pmatrix} \quad \text{or} \quad \hat{\mathbf{G}} := \begin{pmatrix} G^{\mathcal{T}} & G^{<} \\ G^{>} & G^{\bar{\mathcal{T}}} \end{pmatrix}. \tag{2.1.25}$$

The two different definitions of the Keldysh space $\mathbf{G}$ and $\hat{\mathbf{G}}$ are connected by a linear transformation given by the relations 2.1.22.

The perturbative expansion in terms of Feynman diagrams for calculating NEGF is very similar to the equilibrium case, but one has to keep track of the structure of the Keldysh space. In equilibrium, the lesser, the greater, and therefore, the Keldysh Green's function are determined by the retarded and the advanced Green's function by the fluctuation-dissipation theorem.

Fluctuation-dissipation theorem:

$$\begin{aligned} G^{<}_{ij}(\omega) &= 2\pi\mathrm{i} f(\omega) A_{ij}(\omega) \\ G^{>}_{ij}(\omega) &= -2\pi\mathrm{i}\left(1 - f(\omega)\right) A_{ij}(\omega) \end{aligned} \tag{2.1.26}$$

$A_{ij}(\omega)$ is the spectral function defined in Eq. 2.1.24 by use of the retarded and the advanced Green's function and $f(\omega)$ is the Fermi function in thermodynamical equilibrium. By inserting the definitions of lesser and greater Green's function and taking care of the Fourier transformation,

$$\begin{aligned} \left\langle \hat{a}^{\dagger}_j(t')\hat{a}_i(t) \right\rangle &= \int_{-\infty}^{\infty} d\omega\; e^{\mathrm{i}\omega(t-t')} f(\omega) A_{ij}(\omega) \\ \left\langle \hat{a}_i(t)\hat{a}^{\dagger}_j(t') \right\rangle &= \int_{-\infty}^{\infty} d\omega\; e^{\mathrm{i}\omega(t-t')} \left(1 - f(\omega)\right) A_{ij}(\omega)\ , \end{aligned} \tag{2.1.27}$$

we see immediately that the fluctuation-dissipation theorem directly links a correlation functions describing fluctuations, with the dissipative part of the retarded and the advanced response functions described by $A_{ij}(\omega)$. To proof the fluctuation-dissipation theorem, we use the definitions of greater and lesser Green's function at finite temperature and the exact many-particle eigenstates $|m\rangle$ and $|n\rangle$ to obtain the spectral representations

$$\begin{aligned} G^{>}_{ij}(t,t') &= -\frac{\mathrm{i}}{Z}\sum_{mn} e^{-\beta E_n} e^{\mathrm{i}(E_n - E_m)(t-t')} \langle n|\, \hat{a}_i\, |m\rangle \langle m|\, \hat{a}^{\dagger}_j\, |n\rangle \\ G^{<}_{ij}(t,t') &= \frac{\mathrm{i}}{Z}\sum_{mn} e^{-\beta E_n} e^{\mathrm{i}(E_m - E_n)(t-t')} \langle n|\, \hat{a}^{\dagger}_j\, |m\rangle \langle m|\, \hat{a}_i\, |n\rangle\ . \end{aligned} \tag{2.1.28}$$

A subsequent Fourier transformation leads to

$$G_{ij}^{>}(\omega) = -\frac{2\pi\mathrm{i}}{Z}\sum_{mn} e^{-\beta E_n}\langle n|\,\hat{a}_i\,|m\rangle\langle m|\,\hat{a}_j^\dagger\,|n\rangle\,\delta\left(E_m - E_n + \omega\right) \tag{2.1.29}$$
$$G_{ij}^{<}(\omega) = \frac{2\pi\mathrm{i}}{Z}\sum_{mn} e^{-\beta E_n}\langle n|\,\hat{a}_j^\dagger\,|m\rangle\langle m|\,\hat{a}_i\,|n\rangle\,\delta\left(E_n - E_m + \omega\right)\ .$$

Exchanging the indices n and m in the lesser Green's function and the comparison of the equations thus obtained yields

$$G_{ij}^{>}(\omega) = -e^{\beta\omega}G_{ij}^{<}(\omega)\ . \tag{2.1.30}$$

Combining Eqs. 2.1.22 and Eq. 2.1.24 produces

$$A_{ij}(\omega) = \frac{\mathrm{i}}{2\pi}\left(G_{ij}^{>}(\omega) - G_{ij}^{<}(\omega)\right)\ . \tag{2.1.31}$$

Finally, inserting Eq. 2.1.30 produces Eqs. 2.1.26.

2.1.3 Quantum transport

In the present section, we want to sketch the link between NEGF and a charge current caused by electron flow. The current can be calculated by splitting the transport system into two parts, so-called cluster I and cluster II, between which the current flows. Therefore, we split Hamiltonian 2.1.5 into three parts: cluster I, cluster II, and the remaining part connecting the clusters. The charge current between cluster I and cluster II is proportional to the time derivative of the number-of-particle operator in one of the clusters, e.g. for cluster I we have

$$j = -e\frac{d}{dt}\left\langle\hat{N}_\mathrm{I}\right\rangle = -\frac{\mathrm{i}e}{\hbar}\left\langle\left[\hat{H},\hat{N}_\mathrm{I}\right]\right\rangle \tag{2.1.32}$$

where we already used Heisenberg's equation of motion. The square brackets denote the commutator, $[\hat{A},\hat{B}] = \hat{A}\hat{B} - \hat{B}\hat{A}$. By use of the commutation relations

$$[\hat{a}_i,\hat{n}_j] = \delta_{ij}\hat{a}_i \quad\text{and}\quad \left[\hat{a}_i^\dagger,\hat{n}_j\right] = -\delta_{ij}\hat{a}_i^\dagger \tag{2.1.33}$$

which follow from Eqs. 2.1.8, we see that the number-of-particle operator of cluster I, $\hat{N}_\mathrm{I} = \sum_{i\in\mathrm{I}}\hat{n}_i$, commutes with the isolated Hamiltonians of both clusters, I and II, but not with the hopping Hamiltonian connecting the clusters, and therefore

$$\left[\hat{H},\hat{N}_\mathrm{I}\right] = \sum_{\substack{i\in\mathrm{I}\\ j\in\mathrm{II}}}\sum_{l\in\mathrm{I}}\left[\left(t_{ij}\hat{a}_i^\dagger\hat{a}_j + t_{ij}^*\hat{a}_i\hat{a}_j^\dagger\right),\hat{n}_l\right]\ . \tag{2.1.34}$$

In evaluating this commutator, we restricted ourselves to density-density interaction terms only. Inserting this commutator in Eq. 2.1.32 produces

$$j = \frac{e}{\hbar}\sum_{\substack{i\in\mathrm{I}\\ j\in\mathrm{II}}}\left(t_{ij}\mathrm{i}\left\langle\hat{a}_i^\dagger\hat{a}_j\right\rangle - t_{ij}^*\mathrm{i}\left\langle\hat{a}_j^\dagger\hat{a}_i\right\rangle\right)\ . \tag{2.1.35}$$

It turns out that the current depends on the lesser Green's function defined in Eq. 2.1.21. By use of the definition of the lesser Green's function and a subsequent Fourier transformation, the current formula can be rewritten to

$$\begin{aligned} j &= \frac{e}{\hbar} \sum_{\substack{i\in \mathrm{I} \\ j\in \mathrm{II}}} \left(t_{ij} G^<_{\widehat{ji}}(t=0,t'=0) - t^*_{ij} G^<_{\widehat{ij}}(t=0,t'=0) \right) \\ &= \frac{e}{\hbar} \int_{-\infty}^{\infty} d\omega \sum_{\substack{i\in \mathrm{I} \\ j\in \mathrm{II}}} \left(t_{ij} G^<_{\widehat{ji}}(\omega) - t^*_{ij} G^<_{\widehat{ij}}(\omega) \right) . \end{aligned} \tag{2.1.36}$$

Due to the definitions of the Green's functions in Eq. 2.1.21, $G^<_{\widehat{ij}} = -G^{<*}_{\widehat{ji}}$ holds, and by the use of Eqs. 2.1.22, we get an expression for the current depending on the Keldysh Green's function in frequency space,

Current formula:

$$j = \frac{e}{h} \int_{-\infty}^{\infty} d\omega \sum_{\substack{i\in \mathrm{I} \\ j\in \mathrm{II}}} 2\,\mathrm{Re}\left(t_{ij} G^<_{\widehat{ji}}(\omega) \right) = \frac{e}{h} \int_{-\infty}^{\infty} d\omega \sum_{\substack{i\in \mathrm{I} \\ j\in \mathrm{II}}} \mathrm{Re}\left(t_{ij} G^{\mathrm{k}}_{\widehat{ji}}(\omega) \right) . \tag{2.1.37}$$

2.1.4 Equation-of-motion method and the Dyson equation

According to Eq. 2.1.37, we need the Keldysh or the lesser Green's function between the clusters I and II for calculating the current. The aim of the present section is to introduce the equation-of-motion (EOM) method for calculating Green's functions. Furthermore, we introduce the coupling equation and Dyson's equation.

In a first step, we use the EOM method to derive the time evolution of the retarded Green's function. By derivating the definition of the retarded Green's function in Eq. 2.1.23,

$$\begin{aligned} \mathrm{i}\frac{\partial}{\partial t} G^{\mathrm{r}}_{\hat{a}_i \hat{a}_j^\dagger}(t,t') &= \frac{\partial}{\partial t}\theta(t-t') \left\langle \left\{ \hat{a}_i(t), \hat{a}_j^\dagger(t') \right\} \right\rangle \\ &= \delta(t-t') \left\langle \left\{ \hat{a}_i(t), \hat{a}_j^\dagger(t') \right\} \right\rangle - \mathrm{i}\theta(t-t') \left\langle \left\{ \left[\hat{a}_i(t), \hat{H} \right], \hat{a}_j^\dagger(t') \right\} \right\rangle \\ &= \delta(t-t') \left\langle \left\{ \hat{a}_i(t), \hat{a}_j^\dagger(t') \right\} \right\rangle + G^{\mathrm{r}}_{[\hat{a}_i,\hat{H}]\hat{a}_j^\dagger}(t,t') , \end{aligned} \tag{2.1.38}$$

we obtain an equation of motion. This equation also holds for the corresponding advanced Green's function, but in the present derivation, we restrict ourselves to the retarded Green's function. Retarded and advanced Green's function only obey different boundary conditions. The Fourier transformation of Eq. 2.1.38 produces

$$\omega G^{\mathrm{r}}_{\hat{a}_i \hat{a}_j^\dagger}(\omega) = \left\langle \left\{ \hat{a}_i, \hat{a}_j^\dagger \right\} \right\rangle + G^{\mathrm{r}}_{[\hat{a}_i,\hat{H}]\hat{a}_j^\dagger}(\omega) \tag{2.1.39}$$

where the boundary conditions must be inserted additionally by replacing ω by $\omega + \mathrm{i}0^+$ for the retarded Green's function and by replacing ω by $\omega - \mathrm{i}0^+$ for the advanced Green's function.

In case of an interacting Hamiltonian, the equation of motion leads to a series of higher-order Green's functions. The series aborts itself when considering only a one-particle Hamiltonian leading to

$$(\omega + \mathrm{i}0^+)G^{0,\mathrm{r}}_{ij}(\omega) = \left\{S^{-1}\right\}_{ij} + \sum_{kl}\left\{S^{-1}\right\}_{ik} t_{kl} G^{0,\mathrm{r}}_{lj}(\omega) \tag{2.1.40}$$

where we accounted for nonorthogonality of the basis set by using the commutation relations Eqs. 2.1.11. The superscript 0 denotes a noninteracting Green's function. To be more general, this equation also holds in Keldysh space defined in Eq. 2.1.25 and is therefore applicable to nonequilibrium situations. Suppressing the frequency dependence and the superscripts, in matrix notation the equation becomes

$$G = \left((\omega + \mathrm{i}0^+)S - H\right)^{-1} \ . \tag{2.1.41}$$

We will now show how to calculate the Green's function of a subsystem, a so-called cluster. Let us assume that we have two clusters, labeled by the subscripts 0 and 1. Then, the involved matrices have a 2×2 block structure. We want to calculate the Green's function of cluster 0, G_{00}, which is defined by Eq. 2.1.41 using the block-matrix structure,

$$\begin{pmatrix} G_{00} & G_{01} \\ G_{10} & G_{11} \end{pmatrix} = \begin{pmatrix} (\omega + \mathrm{i}0^+)S_{00} - H_{00} & (\omega + \mathrm{i}0^+)S_{01} - H_{01} \\ (\omega + \mathrm{i}0^+)S_{10} - H_{10} & (\omega + \mathrm{i}0^+)S_{11} - H_{11} \end{pmatrix}^{-1} \ . \tag{2.1.42}$$

It is advisable to take advantage of the Schur complement for doing the block matrix inversion. Finally, the full Green's function of cluster 0 is determined by

Coupling equation:

$$G_{00}(\omega) = g_{00}(\omega) + g_{00}(\omega)\Delta_{00}(\omega)G_{00}(\omega) \tag{2.1.43}$$

with the hybridization function

$$\Delta_{00}(\omega) = ((\omega + \mathrm{i}0^+)S_{01} - H_{01})g_{11}(\omega)((\omega + \mathrm{i}0^+)S_{10} - H_{10})$$

describing the influence of the neighboring cluster and the cluster Green's functions $g_{\nu\nu} = (S_{\nu\nu}(\omega + \mathrm{i}0^+) - H_{\nu\nu})^{-1}$ for $\nu \in \{0, 1\}$.

Let us now consider electron-electron interactions. We mentioned in Sec. 2.1.2 that it is possible to do systematic perturbation theory in terms of Feynman diagrams for calculating the contour-ordered Green's function. Furthermore, it is possible to sum formally the diagrams up to infinite order leading to Dyson's equation [67]

Dyson equation:

$$G(\omega) = G^0(\omega) + G^0(\omega)\Sigma(\omega)G(\omega) \ . \tag{2.1.44}$$

Here, G^0 denotes the Green's function without electron-electron interactions, while G includes interactions. All interaction contributions are formally described with the electron self-energy Σ. Importantly, Eqs. 2.1.43 and 2.1.44 show that hybridization and correlation effects can be treated formally in a similar way. We present numerical techniques for calculating G and therefore Σ in the following section and especially in Sec. 2.3.4.

2.1.5 Lehmann representation and cluster perturbation theory

In the present section, we derive the Lehmann representation which enables to calculate interacting Green's functions for *small* systems in equilibrium and we present cluster perturbation theory (CPT) as a first approximation to deal with strong electron correlations. We refer to Ref. [33] for a general introduction to quantum cluster methods for strongly correlated systems.

The noninteracting Green's function G^0 can be calculated by use of Eq. 2.1.41. In equilibrium, the interacting Green's function G can be determined by inserting Eqs. 2.1.28 in the definition of the retarded Green's function,

$$G^{\mathrm{r}}_{ij}(t,t') = \Theta(t-t')\left(G^{>}_{ij}(t,t') - G^{<}_{ij}(t,t')\right) \ , \tag{2.1.45}$$

and then calculating the Fourier transform. This produces the so-called Lehmann representation

Lehmann representation:

$$G^{\mathrm{r}}_{ij}(\omega) = \frac{1}{Z}\sum_{mn} e^{-\beta E_n}\left(\frac{\langle n|\,\hat{a}_i\,|m\rangle\langle m|\,\hat{a}_j^\dagger\,|n\rangle}{\omega + \mathrm{i}0^+ - (E_m - E_n)} + \frac{\langle n|\,\hat{a}_j^\dagger\,|m\rangle\langle m|\,\hat{a}_i\,|n\rangle}{\omega + \mathrm{i}0^+ - (E_n - E_m)}\right) . \tag{2.1.46}$$

The formula shows very clearly that the retarded Green's function has resonances at the differences of the many-particle eigenenergies. The Lehmann representation can be used to calculate the Green's function of systems with a limited number of degrees of freedom, e.g. by employing the band Lanczos algorithm as presented in Ref. [33].

Let us again assume that we have two clusters labeled by the subscripts 0 and 1 and we suppress frequency dependence for the sake of readability. Then, Dyson's equation involves matrices of 2×2 block structure. The approximation used in CPT [68] is to replace the electron self-energy Σ by the electron self-energy of the isolated clusters Σ^{cl}. In our two-cluster example we have

$$\begin{pmatrix} g_{00} & 0 \\ 0 & g_{11} \end{pmatrix} = \begin{pmatrix} g^0_{00} & 0 \\ 0 & g^0_{11} \end{pmatrix} + \begin{pmatrix} g^0_{00} & 0 \\ 0 & g^0_{11} \end{pmatrix} \Sigma^{\mathrm{cl}} \begin{pmatrix} g_{00} & 0 \\ 0 & g_{11} \end{pmatrix} \tag{2.1.47}$$

defining the cluster electron self-energy. For calculating g^0_{ii} and g_{ii} for each cluster $i \in \{0,1\}$ we could use Eq. 2.1.41 and the Lehmann representation, respectively. CPT can be viewed as

a cluster extension of strong-coupling perturbation theory, although limited to lowest order. Using the definition of the cluster self-energy produces for each cluster $i \in \{0, 1\}$

$$\Sigma_{ii}^{\mathrm{cl}} = \left(g_{ii}^{0}\right)^{-1} - \left(g_{ii}\right)^{-1} \ . \tag{2.1.48}$$

This shows that the cluster self-energy obtained in CPT is hermitian if we neglect terms in the order of 0^+.

2.1.6 Current formulas and the transmission

In the present section, we derive the Meir-Wingreen formula [69] and gain the well-known Landauer-Büttiker formula [70, 71] by splitting the Meir-Wingreen formula into coherent and incoherent contributions. This approach also leads to the definition of a coherent and an incoherent transmission function.

We consider a quantum transport system consisting of the left electrode (L), the central region (C) and the right electrode (R) schematically drawn in Fig. 2.2.

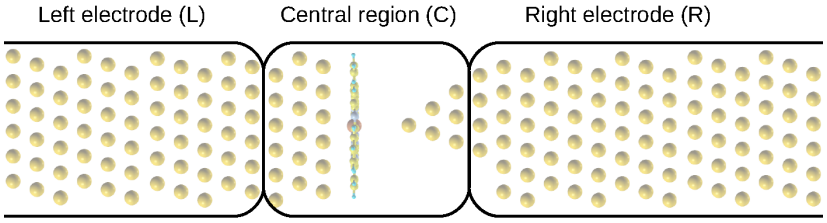

Figure 2.2: Schematic representation of a quantum transport system consisting of the central region (C) and the left (L) and the right (R) electrodes.

In a first step, we aim to calculate the charge current flowing from the left electrode into the central region which leads to the Meir-Wingreen formula. We just briefly outline the derivation and refer to Ryndyk *et al.* [72] for the details. In absence of interactions in the electrodes, the Dyson equation and Langreth's theorem [59] lead to

$$G_{ij}^{<}(\omega) = \sum_{l \in \mathrm{C}} t_{jl}^{*} \left[G_{il}(\omega) g_{j}^{<}(\omega) + G_{il}^{<}(\omega) g_{j}^{\dagger}(\omega) \right] \tag{2.1.49}$$

for the lesser Green's function with $i \in \mathrm{C}$ and $j \in \mathrm{L}$. For the sake of readability, we suppress the superscript r for retarded quantities and reintroduce it when required. The advanced quantities can always be calculated by taking the hermitian adjoint of the retarded ones. Inserting Eq. 2.1.49 into Eq. 2.1.37 produces

$$I_{\mathrm{L}} = \frac{2e}{h} \int_{-\infty}^{\infty} d\omega \ \mathrm{Re} \left(\sum_{\substack{i,l \in \mathrm{C} \\ j \in \mathrm{L}}} t_{ji} t_{jl}^{*} \left[G_{il}(\omega) g_{j}^{<}(\omega) + G_{il}^{<}(\omega) g_{j}^{\dagger}(\omega) \right] \right) \tag{2.1.50}$$

for the current between left electrode and central region. Assuming equilibrium in the leads, and therefore, $g_j^< = 2\pi \mathrm{i} f(\epsilon_j)\delta(\omega-\epsilon_j)$ and $g_j^\dagger(\omega) = (\omega - \mathrm{i}0^+ - \epsilon_j)^{-1}$ according to Eqs. 2.1.26 and 2.1.41, and using $\{\Gamma^\mathrm{L}\}_{il} = 2\pi \sum_{j\in\mathrm{L}} t_{ji}t_{jl}^*\delta(\omega-\epsilon_j)$ produces the well-known Meir-Wingreen formula

Meir-Wingreen formula:

$$I_\mathrm{L} = \frac{\mathrm{i}e}{h}\int_{-\infty}^{\infty} d\omega \;\; \mathrm{Tr}\left\{\Gamma^\mathrm{L}(\omega)\left(G^<(\omega) + f_\mathrm{L}(\omega)\left[G(\omega) - G^\dagger(\omega)\right]\right)\right\} \; . \tag{2.1.51}$$

The Meir-Wingreen formula calculates the current by use of the Green's functions of the central region and is exact in the case of noninteracting leads being in equilibrium. The physical interpretation is achieved when rewriting the Meir-Wingreen formula by use of $\Delta^{\mathrm{L},<}(\omega) = \mathrm{i}f_\mathrm{L}(\omega)\Gamma^\mathrm{L}(\omega)$ and $\Delta^{\mathrm{L},>}(\omega) = -\mathrm{i}(1-f_\mathrm{L}(\omega))\Gamma^\mathrm{L}(\omega)$ following from the fluctuation-dissipation theorem.

$$I_\mathrm{L} = \frac{e}{h}\int_{-\infty}^{\infty} d\omega \;\; \mathrm{Tr}\left\{\Delta^{\mathrm{L},<}(\omega)G^>(\omega) - \Delta^{\mathrm{L},>}(\omega)G^<(\omega)\right\} \tag{2.1.52}$$

Since lesser and greater quantities are proportional to occupied and unoccupied states, respectively, the first term in Eq. 2.1.52 gives the current flowing from the left electrode towards the central region and the second term gives the current flowing from the central region to the left electrode.

In the next step, we want to separate the Meir-Wingreen formula into a coherent and an incoherent contribution. We can rewrite the difference between retarded and advanced Green's function with

$$\begin{aligned} G^\dagger(\omega) &= G(\omega)(G(\omega))^{-1}G^\dagger(\omega) \\ &= G(\omega)((\omega+\mathrm{i}0^+)S - H - \Delta^\mathrm{L}(\omega) - \Delta^\mathrm{R}(\omega) - \Sigma(\omega))G^\dagger(\omega) \\ &= G(\omega)((\omega+\mathrm{i}0^+)S - H)G^\dagger - G(R^\mathrm{L}(\omega) + R^\mathrm{R}(\omega) + R^\mathrm{ee}(\omega))G^\dagger(\omega) \\ &\quad + \frac{\mathrm{i}}{2}G(\omega)(\Gamma^\mathrm{L}(\omega) + \Gamma^\mathrm{R}(\omega) + \Gamma^\mathrm{ee}(\omega))G^\dagger(\omega) \end{aligned} \tag{2.1.53}$$

to

$$G(\omega) - G^\dagger(\omega) = -\mathrm{i}G(\Gamma^\mathrm{L}(\omega) + \Gamma^\mathrm{R}(\omega) + \Gamma^\mathrm{ee}(\omega))G^\dagger(\omega) \; . \tag{2.1.54}$$

Here, we neglected a term $\mathrm{i}2^+G(\omega)SG^\dagger(\omega)$ proportional to 0^+, and the hybridizations and the self-energy are decomposed in hermitian (R) and antihermitian ($\mathrm{i}\Gamma$) parts. Using again Langreth's theorem, the lesser Green's function for steady-state systems becomes

$$\begin{aligned} G^<(\omega) &= G(\omega)\left(\Delta^{\mathrm{L},<}(\omega) + \Delta^{\mathrm{R},<}(\omega) + \Sigma^<(\omega)\right)G^\dagger(\omega) \\ &= G(\omega)(\mathrm{i}f_\mathrm{L}(\omega)\Gamma^\mathrm{L}(\omega) + \mathrm{i}f_\mathrm{R}(\omega)\Gamma^\mathrm{R}(\omega) + \mathrm{i}F(\omega)\Gamma_{ee}(\omega))G^\dagger(\omega) \; . \end{aligned} \tag{2.1.55}$$

Here, we used $\Delta^{x,<}(\omega) = \mathrm{i}f_x(\omega)\Gamma^x(\omega)$ for $x \in \{\mathrm{L},\mathrm{R}\}$ which holds for leads being in equilibrium and $\Sigma^<(\omega) = \mathrm{i}F(\omega)\Gamma^\mathrm{ee}(\omega)$ where $F(\omega)$ is the nonequilibrium occupation matrix. Setting

Eqs. 2.1.54 and 2.1.55 into Eq. 2.1.51 leads to

$$I_L = \underbrace{\frac{e}{h}\int_{-\infty}^{\infty} d\omega\ (f_{\mathrm{L}}(\omega) - f_{\mathrm{R}}(\omega))\ \mathrm{Tr}\left[\Gamma^{\mathrm{L}}(\omega)G(\omega)\Gamma^{\mathrm{R}}(\omega)G^{\dagger}(\omega)\right]}_{I_{\mathrm{coh}}} + \underbrace{\frac{e}{h}\int_{-\infty}^{\infty} d\omega\ \ \mathrm{Tr}\left[(f_{\mathrm{L}}(\omega) - F(\omega))\Gamma^{\mathrm{ee}}(\omega)G^{\dagger}(\omega)\Gamma^{\mathrm{L}}(\omega)G(\omega)\right]}_{I_{\mathrm{L,inc}}} \tag{2.1.56}$$

separating the current into a coherent part and an incoherent part due to the electron-electron correlations. By ignoring correlations by setting the electron self-energy to zero, just the coherent part remains and the current formula becomes the well-known Landauer-Büttiker formula.

Landauer-Büttiker formula:

$$I_{\mathrm{coh}} = \frac{e}{h}\int_{-\infty}^{\infty} d\omega\ (f_{\mathrm{L}}(\omega) - f_{\mathrm{R}}(\omega))\ T_{\mathrm{coh}}(\omega) \tag{2.1.57}$$

$$T_{\mathrm{coh}}(\omega) = \ \mathrm{Tr}\left[\Gamma^{\mathrm{L}}(\omega)G(\omega)\Gamma^{\mathrm{R}}(\omega)G^{\dagger}(\omega)\right]$$

$T_{\mathrm{coh}}(\omega)$ denotes the coherent part of the transmission. Since the self-energy is hermitian in CPT, see Eq. 2.1.48, Γ^{ee} becomes zero and the Landauer-Büttiker formula stays exact within CPT.

To calculate the incoherent current in Eq. 2.1.56, the nonequilibrium occupation matrix $F(\omega)$ is needed. In the following paragraph, we report two ways for determining the occupation matrix. In the case of a single impurity with $\Gamma^{\mathrm{L}} = \lambda\Gamma^{\mathrm{R}}$, one can substitude $F(\omega)$ by using the current conservation condition leading to

$$I_{\mathrm{L,inc}} = \frac{e}{h}\int_{-\infty}^{\infty} d\omega\ (f_{\mathrm{L}}(\omega) - f_{\mathrm{R}}(\omega))\ \Gamma^{\mathrm{ee}}(\omega)G^{\dagger}(\omega)\frac{\Gamma^{\mathrm{L}}(\omega)\Gamma^{\mathrm{R}}(\omega)}{\Gamma^{\mathrm{L}}(\omega) + \Gamma^{\mathrm{R}}(\omega)}G(\omega)\ . \tag{2.1.58}$$

For the case of having more than one impurity orbital, Ness *et al.* [73] discuss the applicability of a generalized Landauer-Büttiker formula for a nonequilibrium current in the presence of interactions and suggest to rewrite Eq. 2.1.56 to

$$I_{\mathrm{L}} = \frac{2e}{h}\int_{-\infty}^{\infty} d\omega\ (f_{\mathrm{L}}(\omega) - f_{\mathrm{R}}(\omega))\ \mathrm{Tr}\left[\Gamma^{\mathrm{L}}(\omega)G(\omega)\Upsilon^{\mathrm{R}}(\omega)G^{\dagger}(\omega)\right] \tag{2.1.59}$$

with $\Upsilon^{\mathrm{R}}(\omega) = \Gamma^{\mathrm{R}}(\omega)\Lambda(\omega)$ and

$$\Lambda(\omega) = 1 + \Gamma^{\mathrm{R}}(\omega)^{-1}\frac{f_{\mathrm{L}}(\omega) - F(\omega)}{f_{\mathrm{L}}(\omega) - f_{\mathrm{R}}(\omega)}\Gamma^{\mathrm{ee}}(\omega)\ . \tag{2.1.60}$$

The formula shows that interactions do not only affect the Green's functions but also renormalize the coupling to the contact through $\Upsilon^{\mathrm{R}}(\omega)$. Ng [74] proposed approximating $\Lambda(\omega)$ by

using the ansatz

$$\begin{aligned}\Sigma^{>}_{\Delta}(\omega) &= \Delta^{>}(\omega)\Lambda(\omega) \\ \Sigma^{<}_{\Delta}(\omega) &= \Delta^{<}(\omega)\Lambda(\omega)\ .\end{aligned} \tag{2.1.61}$$

$\Delta^i(\omega)$ is the total hybridization, therefore the tunneling self-energy of the left and the right lead, and $\Sigma^i_\Delta(\omega)$ denotes the self-energy including tunneling and interaction,

$$\begin{aligned}\Delta^i(\omega) &= \Delta^{\mathrm{L},i}(\omega) + \Delta^{\mathrm{R},i}(\omega) \\ \Sigma^i_\Delta(\omega) &= \Delta^{\mathrm{R},i}(\omega) + \Delta^{\mathrm{R},i}(\omega) + \Sigma^i(\omega)\ ,\end{aligned} \tag{2.1.62}$$

with $i \in \{\mathrm{r}, \mathrm{a}, <, >\}$. According to Ref. [75], we define the retarded and advanced self-energies and hybridizations $X \in \{\Sigma, \Delta\}$ as

$$\begin{aligned}X^{\mathrm{r}}(\omega) &:= R(\omega) - \frac{\mathrm{i}}{2}\Gamma(\omega) - \mathrm{i}\delta^+ \\ X^{\mathrm{a}}(\omega) &:= R(\omega) + \frac{\mathrm{i}}{2}\Gamma(\omega) + \mathrm{i}\delta^+\end{aligned} \tag{2.1.63}$$

consisting of an hermitian and an antihermitian part, R and $\mathrm{i}\Gamma$, respectively. We added the $\mathrm{i}\delta^+$ term to regularize the inverse of the hybridization when $\Gamma(\omega)$ vanishes. For the various self-energies and hybridizations defined so far, the relation $X^{>}(\omega) - X^{<}(\omega) = X^{\mathrm{r}}(\omega) - X^{\mathrm{a}}(\omega)$ holds and by subtracting the two lines in Eq. 2.1.61, we can write

$$\begin{aligned}\Lambda(\omega) &= \left(\Delta^{\mathrm{r}}(\omega) - \Delta^{\mathrm{a}}(\omega)\right)^{-1}\left(\Sigma^{\mathrm{r}}_{\Delta}(\omega) - \Sigma^{\mathrm{a}}_{\Delta}(\omega)\right) \\ &= \left(\Gamma^{\mathrm{R}}(\omega) + \Gamma^{\mathrm{L}}(\omega) + 2\delta^+\right)^{-1}\left(\Gamma^{\mathrm{R}}(\omega) + \Gamma^{\mathrm{L}}(\omega) + \Gamma^{\mathrm{ee}}(\omega) + 2\delta^+\right) \\ &\approx 1 + \left(\Gamma^{\mathrm{R}}(\omega) + \Gamma^{\mathrm{L}}(\omega) + 2\delta^+\right)^{-1}\Gamma^{\mathrm{ee}}(\omega)\ .\end{aligned} \tag{2.1.64}$$

We see that $\Lambda(\omega)$ differs from one only for weak coupling to the leads ($|\Gamma^{\mathrm{L}}(\omega) + \Gamma^{\mathrm{R}}(\omega)| \lesssim |\Gamma^{\mathrm{ee}}(\omega)|$). As shown in Ref. [75] and in the following, the $\Lambda(\omega)$ obtained from this ansatz is an approximation for the $\Lambda(\omega)$ in Eq. 2.1.60 and is exact for *nonequilibrium mean-field theory* and for the *equilibrium many-body* case. To show this, we deduce two equations similar to Eqs. 2.1.54 and 2.1.55, first

$$-\mathrm{i}G(\omega)\left(\Gamma^{\mathrm{L}}(\omega) + \Gamma^{\mathrm{R}}(\omega)\right)\Lambda(\omega)G^\dagger(\omega) = G(\omega) - G^\dagger(\omega) \tag{2.1.65}$$

which is exact, and second

$$G(\omega)\left(\Delta^{\mathrm{L},<}(\omega) + \Delta^{\mathrm{R},<}(\omega)\right)\Lambda(\omega)G^\dagger(\omega) = G(\omega)\big(\Delta^{\mathrm{L},<}(\omega) + \Delta^{\mathrm{R},<}(\omega) + \sigma^{<}(\omega)\big)G^\dagger(\omega)$$

with

$$\sigma^{<}(\omega) = \left(\Delta^{\mathrm{L},<}(\omega) + \Delta^{\mathrm{R},<}(\omega)\right)\left(\Gamma^{\mathrm{R}}(\omega) + \Gamma^{\mathrm{L}}(\omega) + 2\delta^+\right)^{-1}\Gamma^{\mathrm{ee}}(\omega) \tag{2.1.66}$$

which becomes $G^<(\omega)$ if $\sigma^< = \Sigma^<$. This happens in the two limiting cases. Either the system is uncorrelated (*nonequilibrium mean-field*), then trivially $\Sigma^< = \sigma^< = 0$, or in the *equilibrium many-body* case where $f_{\mathrm{L}}(\omega) = f_{\mathrm{R}}(\omega) = F(\omega)$ and $\Sigma^<(\omega) = \mathrm{i}f(\omega)\Gamma(\omega)$ and therefore

$$\begin{aligned}\sigma^{<}(\omega) &= \mathrm{i}\left(f_{\mathrm{L}}(\omega)\Gamma^{\mathrm{L}}(\omega) + f_{\mathrm{R}}(\omega)\Gamma^{\mathrm{R}}(\omega)\right)\left(\Gamma^{\mathrm{L}}(\omega) + \Gamma^{\mathrm{R}}(\omega) + 2\delta^+\right)^{-1}\Gamma^{\mathrm{ee}}(\omega) \\ &= \left(\Gamma^{\mathrm{L}}(\omega) + \Gamma^{\mathrm{R}}(\omega)\right)\left(\Gamma^{\mathrm{L}}(\omega) + \Gamma^{\mathrm{R}}(\omega) + 2\delta^+\right)^{-1}\mathrm{i}F(\omega)\Gamma^{\mathrm{ee}}(\omega) \\ &\approx \Sigma^{<}(\omega)\ .\end{aligned} \tag{2.1.67}$$

Thus, we can finally rewrite the incoherent part of the current to

Incoherent current contribution (Ng approximation):

$$I_{\mathrm{L,inc}} = \frac{e}{h}\int_{-\infty}^{\infty} d\omega\, \left(f_{\mathrm{L}}(\omega) - f_{\mathrm{R}}(\omega)\right) T_{\mathrm{L,inc}}(\omega) \tag{2.1.68}$$

$$T_{\mathrm{L,inc}}(\omega) = \mathrm{Tr}\left[\Gamma^{\mathrm{L}}(\omega)G(\omega)\Gamma^{\mathrm{R}}(\omega)\left(\Gamma^{\mathrm{L}}(\omega)+\Gamma^{\mathrm{R}}(\omega)+2\delta^{+}\right)^{-1}\Gamma^{\mathrm{ee}}(\omega)G^{\dagger}(\omega)\right] .$$

The total current is $I = I_{\mathrm{coh}} + I_{\mathrm{L,inc}}$, and therefore, the total transmission is given by $T(\omega) = T_{\mathrm{coh}}(\omega) + T_{\mathrm{L,inc}}(\omega)$. Within this thesis either CPT is used, and therefore the Landauer-Büttiker formula is exact, or calculations are done at equilibrium, and therefore we can use the Ng approximation.

The main task for calculating incoherent current contributions is to find a *good* approximation for the self-energies $\Sigma^{<}$ and $\Sigma^{>}$. In the present section, we presented the Ng approximation which is based on the ansatz 2.1.61 but we want to refer to Refs. [73, 76] for further approaches. A criterium to judge the approximation for the self-energies is the current conservation condition [77],

$$\int_{-\infty}^{\infty} d\omega\ \mathrm{Tr}\left[\Sigma^{<}(\omega)G^{>}(\omega) - \Sigma^{>}(\omega)G^{<}(\omega)\right] = 0 . \tag{2.1.69}$$

Alternatively, by exchanging the subscripts L and R in Eqs. 2.1.57 and 2.1.68, it can be seen immediately that the current is conserved, first, if CPT is used and therefore $\Gamma^{\mathrm{ee}} = 0$, and second, if all quantities are scalar functions or matrices with a dominant diagonal, respectively. These are the cases where we applied the current formulas in the present thesis.

2.1.7 Differential conductance

For our purposes, a remaining task is to relate the transmission $T(\omega)$ to the differential conductance, as e.g. measured by an scanning tunneling microscope (STM). As the STM tip usually couples weakly to the molecule, it is reasonable that the voltage u only affects the Fermi function of the right lead describing the STM tip via a shift of the energy axis. At small temperatures and close to equilibrium ($T(\omega)$ is independent of u) we find:

$$\begin{aligned}\frac{d}{du}I(u) &\approx \frac{d}{du}\frac{e}{h}\int_{-\infty}^{\infty} d\omega\, \left(f_{\mathrm{L}}(\omega) - f_{\mathrm{R}}(\omega-u)\right) T(\omega) \\ &\approx \frac{d}{du}\frac{e}{h}\int_{0}^{u} d\omega\, T(\omega) \propto T(u) ,\end{aligned} \tag{2.1.70}$$

i.e., for small temperatures and voltages, the differential conductance is proportional to the transmission itself.

2.2 Density functional theory

A very popular method for the calculation of electronic properties in solid-state physics is DFT. In combination with NEGF, DFT has become the state-of-the-art method for performing quantum transport simulations from first principles. The present section gives a brief introduction to DFT, basis functions, the combination with NEGF, and discusses the success and limitations of DFT in quantum transport simulations.

In Sec. 2.2.1, we present the basic concepts of DFT. Sec. 2.2.2 briefly introduces maximally localized Wannier functions (MLWF) and atomic orbitals. We present the interface between DFT and NEGF in Sec. 2.2.3 and discuss success and limitations of the DFT+NEGF method in Sec. 2.2.4.

2.2.1 Basic concepts

This section is a brief introduction to the basic concepts of DFT adapted from Refs. [78, 79]. We aim to solve the time-independent Schrödinger equation with the Hamiltonian 2.1.2. DFT introduces a great simplification since DFT is based on the ground-state density

$$n_0(\mathbf{r}) = \int d^3r_1 ... \int d^3r_N \; \Phi_0^*(\mathbf{r}_1, ..., \mathbf{r}_N) \sum_{i=1}^{N} \delta(\mathbf{r} - \mathbf{r}_i) \Phi_0(\mathbf{r}_1, ..., \mathbf{r}_N) \tag{2.2.1}$$

instead of the full ground-state many-body wave function $\Phi_0(\mathbf{r}_1, ..., \mathbf{r}_N)$. While $\Phi_0(\mathbf{r}_1, ..., \mathbf{r}_N)$ depends on the coordinates of the N electrons, the ground-state density $n_0(\mathbf{r})$ depends just on the spatial coordinates. The Hohenberg-Kohn theorem [80] states that the ground-state energy is a unique functional of the ground-state particle density. Given the energy functional $E[n(\mathbf{r})]$, the variational principle

$$E_0[n_0(\mathbf{r})] = \min_{n(\mathbf{r})} E[n(\mathbf{r})] \tag{2.2.2}$$

with the constraint $\int d^3r \; n(\mathbf{r}) = N$ can be used to obtain the ground-state energy and particle density of the system. In order to determine the energy functional, we can split it into three contributions: the kinetic energy, the one-particle potential energy, and the interaction energy.

$$E[n(\mathbf{r})] = T[n(\mathbf{r})] + V[n(\mathbf{r})] + U[n(\mathbf{r})] \tag{2.2.3}$$

Kohn and Sham [81] achieved a major breakthrough by introducing an auxiliary noninteracting reference system with the same ground-state density as the interacting one; the so-called Kohn-Sham orbitals $\Phi_i(\mathbf{r})$ have been invented. For noninteracting electrons the kinetic energy functional is

$$T[n(\mathbf{r})] = \sum_{i=1}^{N} \int d^3r \; \Phi_i^*(\mathbf{r}) \left(-\frac{\hbar^2}{2m} \Delta \right) \Phi_i(\mathbf{r}) \tag{2.2.4}$$

with the particle density being

$$n(\mathbf{r}) = \sum_{i=1}^{N} |\Phi_i(\mathbf{r})|^2 \tag{2.2.5}$$

where the sum is over all occupied orbitals. Since Eq. 2.2.4 is for noninteracting electrons rather than interacting ones, we assume that the difference in the kinetic functional is accounted for in the exchange correlation functional $E_{\mathrm{xc}}[n(\mathbf{r})]$ which we introduce shortly. The one-particle potential energy depends on the particle density as

$$V[n(\mathbf{r})] = \int d^3r \; V(\mathbf{r}) n(\mathbf{r}) \; . \tag{2.2.6}$$

In comparison with Hartree-Fock theory the interacting functional is

$$U[n(\mathbf{r})] = \frac{1}{2} \int d^3r \; V_{\mathrm{h}}(\mathbf{r}) n(\mathbf{r}) + E_{\mathrm{xc}}[n(\mathbf{r})] \tag{2.2.7}$$

where $V_{\mathrm{h}}(\mathbf{r})$ denotes the Hartree potential

$$V_{\mathrm{h}}(\mathbf{r}) = \phi(\mathbf{r}) = \int d^3r' \frac{e^2}{4\pi\epsilon \, |\mathbf{r} - \mathbf{r}'|} n(\mathbf{r}') \tag{2.2.8}$$

resulting from solving Poisson's equation,

$$\Delta\phi(\mathbf{r}) = \frac{e n(\mathbf{r})}{\epsilon} \; . \tag{2.2.9}$$

Applying the variational principle in the Kohn-Sham orbitals produces the Kohn-Sham equations.

Kohn-Sham equations:

$$\left\{ -\frac{\hbar^2}{2m}\Delta + V(\mathbf{r}) + V_{\mathrm{h}}(\mathbf{r}) + \frac{\delta E_{\mathrm{xc}}[n(\mathbf{r})]}{\delta n(\mathbf{r})} \right\} \Phi_i(\mathbf{r}) = \epsilon_i \Phi_i(\mathbf{r}) \tag{2.2.10}$$

Importantly, the Kohn-Sham equations must be solved self-consistently in combination with Eq. 2.2.5 giving the connection between the wave functions and the particle density. Finally, this leads to the Kohn-Sham energies ϵ_i and the Kohn-Sham wave functions $\Phi_i(\mathbf{r})$. In DFT, the difficulties arising when directly solving the N electron problem defined in Eq. 2.1.2 are shifted to the problem of finding a good approximation for exchange correlation functional $E_{\mathrm{xc}}[n(\mathbf{r})]$. A widely used approximation for this functional is the local density approximation (LDA) where the exchange correlation functional depends only on the local density coordinates. In the generalized gradient approximation (GGA), the functional depends additionally on the gradient of the electron density. We refer to Sec. 2.2.4 for a brief discussion about generic problems of approximating the functional and the success story and limitations of DFT.

Usually, the Kohn-Sham equations are solved numerically using a finite set of basis functions to reduce the differential equations to a set of algebraic equations. We discuss two types of localized basis functions commonly used in transport calculations in Sec. 2.2.2.

2.2.2 Atomic basis and maximally localized Wannier functions

Although charge current is a scalar quantity, we need to define at least two volumes in position space, e.g. drain and source, where the current is flowing in between. We already used this concept to derive the current formula between two systems in Sec. 2.1.3. Spatial resolution is obtained by using a localized wave function basis. In DFT there are at least two established approaches to achieve localized basis functions: (i) using a plane-wave DFT code in combination with MLWF, and (ii), using finite-range pseudo-atomic orbitals. Both concepts are briefly summarized in the following sections. Benchmark calculations for the coherent transmission function of five representative single-molecule junctions using the two different approaches based on independent DFT codes are for instance presented in Ref. [82].

Maximally localized Wannier functions

This section is mainly adopted from Ref. [79] and a brief introduction to MLWF can also be found in Ref. [83]. DFT codes developed in solid-state physics take advantage of Bloch's theorem. Solving the Kohn-Sham equations in k space results in Bloch states $\Phi_{n\mathbf{k}}(\mathbf{r})$ and the corresponding energies $\epsilon_{n\mathbf{k}}$ with the band index n and the momentum $\mathbf{k}$. The Bloch states are spreaded out over the crystal structure by definition. With the unitary transformation $U_{mn}^{(\mathbf{k})}$, the system can be transformed to a localized basis using MLWF $\Psi_{n\mathbf{R}}(\mathbf{r})$ where $\mathbf{R}$ is the lattice vector. The transformation can be written as

$$\Psi_{n\mathbf{R}}(\mathbf{r}) = \frac{V}{(2\pi)^3} \int_{\mathrm{BZ}} d\mathbf{k}\, e^{-\mathrm{i}\mathbf{k}\mathbf{R}} \left(\sum_m U_{mn}^{(\mathbf{k})} \Phi_{m\mathbf{k}}(\mathbf{r}) \right) \tag{2.2.11}$$

with V as the unit cell volume. The unitary transformation $U_{mn}^{(\mathbf{k})}$ between Bloch and Wannier functions is not unique and several methods have been designed to find an optimal recipe. The method of Marzari and Vanderbilt [31] is minimizing the sum of the second moments of the Wannier functions, the so-called spread,

$$\Omega = \sum_n \left[\langle \Psi_{n\mathbf{0}}(\mathbf{r}) |\, r^2 \,| \Psi_{n\mathbf{0}}(\mathbf{r}) \rangle - \left(\langle \Psi_{n\mathbf{0}}(\mathbf{r}) |\, \mathbf{r} \,| \Psi_{n\mathbf{0}}(\mathbf{r}) \rangle \right)^2 \right] , \tag{2.2.12}$$

to obtain $U_{mn}^{(\mathbf{k})}$. One can split Ω into a gauge invariant term Ω_{I} and a term $\tilde{\Omega}$ that depends on the choise of $U_{mn}^{(\mathbf{k})}$, and therefore, the method of Marzari and Vanderbilt is minimizing only the term $\tilde{\Omega}$.

The procedure described above is sufficient to obtain MLWFs from an isolated group of bands which means that there is a finite gap to the remaining bands. For a group of bands which is not isolated, so-called entangled bands, one needs an extra procedure as presented in Ref. [32]. This procedure is needed to disentangle the s and d bands from the p bands in Au and Pt in Secs. 3.3 and 3.4, respectively. To do so, one has to define an energy window which includes at least the N Wannier bands of interest. All the bands inside this window are part of the Hilbert space $\mathcal{F}(\mathbf{k})$. Minimizing Ω_{I}, which turns out to measure the *change of character* of the bands, is used to get the right N dimensional subspace $\mathcal{S}(\mathbf{k}) \subseteq \mathcal{F}(\mathbf{k})$.

Additionally, a second energy window, the so-called inner window, can be defined to force the algorithm to keep the bands in the inner window in the subspace $\mathcal{S}(\mathbf{k})$. Having defined the subspace $\mathcal{S}(\mathbf{k})$, minimizing $\tilde{\Omega}$ leads to the MLWFs.

Atomic basis functions

DFT codes like SIESTA [84] employ a localized basis set from the beginning, which circumvents a Wannier transformation but demands effort in designing the basis functions properly. Commonly used basis functions are finite-range pseudo-atomic wave functions that split up into an angular component, e.g. described by spherical harmonics, and a radial component, e.g. approximated by slater type orbitals (STOs) or Gaussian type orbitals (GTOs). These basis functions are strongly localized around the center of the atoms and mutually nonorthogonal.

2.2.3 Combining DFT and NEGF

In this section, we sketch how Kohn-Sham (KS) DFT is combined with NEGF theory in software packages like TranSIESTA [85, 86]. First of all, it seems likely to use the KS Hamiltonian with the eigenenergies ϵ_i and eigenstates Φ_i obtained by solving the KS equation to build up Green's functions. In the present section, we assume that approximating the Hamiltonian by the KS Hamiltonian is justified but we discuss possible consequences in Sec. 2.2.4.

TranSIESTA uses separate electrode calculations of a periodic system for calculating the KS Hamiltonians of the infinite left and right electrodes. The method of Sancho *et al.* [87–89] is used for calculating surface Green's functions and hybridization functions of the semi-infinite electrodes. Since we assume the electrodes to be in equilibrium, the hybridization functions $\Delta^{\mathrm{L}}(\omega)$ and $\Delta^{\mathrm{R}}(\omega)$ in combination with the Fermi functions $f_{\mathrm{L}}(\omega)$ and $f_{\mathrm{R}}(\omega)$ include all information about the electrodes. This allows to perform the DFT calculation of the full transport system by solving the KS equations just for the central region and to include the electrodes in terms of hybridization functions and Fermi functions. There are two main differences to the standard equilibrium DFT approach introduced in the previous section which we discuss in the following paragraphs.

First, in applying a bias voltage at the electrodes, e.g. by shifting their chemical potentials, the central region is driven into nonequilibrium. The KS orbitals in the central region are not filled with N electrons according to Eq. 2.2.5 anymore because, first, the left and right electrodes include dissipative terms and may change the filling of the central region, and second, in nonequilibrium the central region does not obey Fermi-Dirac statistics anymore. Therefore the electron density needs to be connected to a density matrix D_{ij} by

$$n(\mathbf{r}) = \sum_{ij} \Phi_i(\mathbf{r}) \Re\{D_{ij}\} \Phi_j(\mathbf{r}) \; . \tag{2.2.13}$$

Here, we imply a basis set with real basis functions to neglect the imaginary part of D_{ij}. The density matrix is connected to the lesser Green's function by

$$D_{ij} = \langle \hat{a}_j^\dagger \hat{a}_i \rangle = \frac{1}{2\pi \mathrm{i}} \int_{-\infty}^{\infty} d\omega \; G_{ij}^<(\omega) \; . \tag{2.2.14}$$

Obviously, the calculation of $G_{ij}^<(\omega)$ requires the KS Hamiltonian of the central region and the hybridization functions and Fermi functions of the electrodes. To simplify Eq. 2.2.14, we use Eqs. 2.1.54 and 2.1.55 in the noninteracting case ($\Gamma_{ee}(\omega) = 0$) to write

$$G^<(\omega) = -f_\mathrm{L}(\omega) \left(G(\omega) - G^\dagger(\omega) \right) + \mathrm{i} \left(f_\mathrm{R}(\omega) - f_\mathrm{L}(\omega) \right) G(\omega) \Gamma^\mathrm{R} G^\dagger(\omega) \; . \tag{2.2.15}$$

This is justified since the KS system is an effective system of noninteracting particles by construction. By inserting Eq. 2.2.15 into Eq. 2.2.14, the density matrix becomes

$$\begin{aligned} D_{ij} = & \underbrace{\frac{\mathrm{i}}{2\pi} \int_{-\infty}^{\infty} d\omega \; f_\mathrm{L}(\omega) \left(G_{ij}(\omega) - G_{ij}^\dagger(\omega) \right)}_{D_{ij}^\mathrm{L}} \\ & + \underbrace{\frac{1}{2\pi} \int_{-\infty}^{\infty} d\omega \; \left(f_\mathrm{R}(\omega) - f_\mathrm{L}(\omega) \right) \left\{ G(\omega) \Gamma^\mathrm{R}(\omega) G^\dagger(\omega) \right\}_{ij}}_{\mathcal{D}_{ij}^\mathrm{R}} \; . \end{aligned} \tag{2.2.16}$$

In the equilibrium case, $\mathcal{D}_{ij}^\mathrm{R}$ is zero due to having the same Fermi function for the whole transport system, $f_\mathrm{R}(\omega) = f_\mathrm{L}(\omega)$. The integrand of the D_{ij}^L term includes the Green's functions $G(z)$ and $G^\dagger(z)$ where all poles lie on the real axis and the functions are analytic otherwise. Therefore, the residue theorem and the poles of the Fermi function $f_\mathrm{L}(z)$ at $z_\nu = \mathrm{i}(2\nu + 1)\pi k_\mathrm{B} T$ can be used for performing the integration on a contour where the integrand is smooth. In nonequilibrium, the computation of $\mathcal{D}_{ij}^\mathrm{R}$ involves the triple product $G(\omega)\Gamma^\mathrm{R}(\omega)G^\dagger(\omega)$ which is not analytic anymore and the integration has to be done on a fine grid and using finite level broadening of the poles in the Green's functions. Unfortunately, this integration can be problematic even at small bias voltages.

Secondly, in the DFT calculations for the central region, we have open boundary conditions and the Hartree potential must be chosen consistently at the boundaries to the electrodes. This can be done by taking

$$V_h(\mathbf{r}) = \phi(\mathbf{r}) + \mathbf{a}\mathbf{r} + b \; . \tag{2.2.17}$$

where $\phi(\mathbf{r})$ is a solution of the Poisson equation in the central region and the remaining term, which is not determined by the Poisson equation, can be chosen according to the electrostatic potential at the electrode boundaries.

2.2.4 Success story, limitations and perspectives

Perspectives about quantum transport simulations from first principles can for instance be found in Refs. [4, 5, 90, 91]. The DFT+NEGF method is, compared to other methods, computationally feasible and is able to explain many transport effects occurring in experiments

qualitatively. Famous examples are the exponentially decaying conductance with the length of molecules like alkanes, oligophenylenes and oligothiophenes [92] and the increasing conductance with the length of oligoacenes [93]. As demonstrated by these examples, for many transport systems the DFT+NEGF method gives the qualitative picture of the transport properties but fails in calculating the conductance quantitatively. Calculated conductance values tend to be up to a factor of two orders of magnitude higher than the measured ones. There are at least two reasons for this discrepancy; first, the conductance depends sensitively on the geometry which is often not known very well, and secondly, the approximations done in the DFT+NEGF method which we will discuss more in detail in the present section.

DFT - a ground state theory

A consequence of the Hohenberg-Kohn theorem is that the ground-state energy is a functional of the ground-state particle density. In this paragraph, we assume that we know the exact energy functional. Quantities being a functional of the ground-state particle density can in principle be obtained in DFT if their functional form is known. Applying the variational principle for minimizing the energy functional leads to the KS Hamiltonian which describes a fictitious system of noninteracting particles that generates the same ground-state density as the given system of interacting particles. A rigorous interpretation of eigenenergies of the KS Hamiltonian is very difficult; an exception is the energy of the HOMO which is the negative of the ionization potential of the system [94]. In the DFT+NEGF method, transport calculations are done using this KS Hamiltonian. To see whether doing so is justified, in the spirit of DFT, one has to derive the conductance functional $G[n]$. For the single impurity Anderson model (SIAM) at $T = 0$ K and zero bias, this functional is known [95–98] and the DFT+NEGF calculation yields the exact zero-bias conductance provided that the exact ground-state functional has been used. This is the main argument why using the KS Hamiltonian in the DFT+NEGF method could lead to the correct conductance even if the KS Hamiltonian and thus Green's functions are, in general, not physical. Generalization for the observations on the SIAM to multi-level models is discussed but Schmitteckert *et al.* [99] showed that the deviations of KS transport to the exact conductance can be sizable.

DFT - approximating the functional

Doing exact DFT implies knowing the exact exchange correlation functional, which is in general not the case and approximated functionals are used instead. In the case of finite-bias calculations there is even a dynamical contribution to the exchange correlation functional [91, 100] and there is no hint that these contributions are generically small. The approximate nature of the exchange correlation functional leads to the so-called level misalignment of the eigenenergies of the KS Hamiltonian. The quality of a given functional is often judged by comparing the local spectral function, e.g. the width and position of the resonances, to higher level theories or experiments. Known problems within KS DFT are: i) In open-shell systems, the Kondo effect and the Coulomb blockade are not captured by GGA and

hybrid functionals due to the missing derivative discontinuity. Consequently, there is no Abrikosov-Suhl resonance and the HOMO-LUMO gap is underestimated. ii) The HOMO-level is estimated usually to high in energy with respect to the vacuum level. This is caused by a self-interaction error [29] resulting from a spurious interaction of an electron with the Hartree and exchange correlation potentials generated by itself. iii) The screening effect of the electrodes is ignored in GGAs and hybrid functionals and therefore the HOMO-LUMO gap is not reduced. Strategies to overcome these problems are developements by the surface science community, such as the scissor operator and image charge corrections, and the use of higher level theories, such as GW [101, 102]. The first strategies are often criticized for being *ad hoc*. The latter suffers from converging problems, is computationally more demanding, and does not guarantee better results. Kondo effect and Coulomb blockade remain out of the range of both strategies.

DFT+NEGF - technical issues

Beside the problems in the foundation of the DFT+NEGF method, there are some technical issues leading to deviations in the calculated results. There are small differences in the numerical implementations of the codes [5]. Deviations in calculated results are caused by, e.g., variations in the positions where the system is separated into electrodes and central region, and the way how the semi-infinite leads are calculated. Another important factor is the basis set chosen in the DFT calculation. For instance, Ref. [82] compares codes using Wannier and atomic basis sets, respectively.

Perspectives

There exist several concepts to overcome the limitations of the DFT+NEGF method. First, TDDFT [91] and steady-state DFT [103] are both giving nonequilibrium contributions to the exchange correlation functional. Secondly, there are approaches avoiding DFT in general such as the configuration interaction (CI) formalism [104] which suffers from the finite CI expansion and the use of scattering boundary conditions. Also dynamical mean-field theory (DMFT) has become a promising technique for calculating transport [11]. One can take advantage of the power of the DFT+NEGF method in the uncorrelated parts of the transport system and use many-body methods and modeling for the correlated parts. The present thesis is in the spirit of the latter approach and we present details in the following Sec. 2.3.

2.3 Embedded many-body systems

Since strongly correlated molecules require a proper many-body treatment, the present section introduces a projection scheme to obtain an AIM describing the strongly correlated parts of the transport system embedded in the environment describing the residual system. We refer to Refs. [105–107] for a general overview to quantum embedding theories. Furthermore, in the present section, we briefly discuss the impurity solver employed within this thesis.

While Secs. 2.3.1 and 2.3.2 introduce the projection scheme for the case of orthogonal and nonorthogonal basis functions, Sec. 2.3.3 defines the multi-orbital AIM, and Sec. 2.3.4 briefly discusses the impurity solver employed within this thesis. Finally, in Sec. 2.3.5, we present how to separate the coherent transmission into contributions from different channels.

2.3.1 Projection onto the correlated subspace

In this section, we briefly discuss the projection onto the correlated subspace in case the effective one-particle KS Hamiltonian is given in a basis of orthogonal orbitals, e.g. MLWF. The AIM then allows to study the influence of correlation effects on quantum transport in addition to those effects already covered by standard DFT+NEGF. We apply the projection scheme presented in the present section to the case of BDT between monoatomic Au and Pt electrodes in Chpt. 3.

We consider an LCR transport system as already drawn schematically in Fig. 2.2. We transform the Hamiltonian of the central region H by use of the unitary transformation matrix M to obtain

$$\bar{H} = M^\dagger H M = \begin{pmatrix} \bar{H}_{\mathrm{AI}} & \bar{H}_{\mathrm{AI,NI}} \\ \bar{H}^\dagger_{\mathrm{AI,NI}} & \bar{H}_{\mathrm{NI}} \end{pmatrix} . \tag{2.3.1}$$

In the transformed space, the Hamiltonian separates in a noninteracting (NI) part, the Anderson impurity (AI), and coupling terms. M defines whether orbitals belong to AI or NI. The very difficult and challenging task is choosing M, and therefore, the correlated subspace. Two commonly used approaches for defining the correlated subspace are (i) choosing a subset of the localized orbitals, e.g. MLWF or atomic orbitals, or (ii) selecting eigenorbitals or molecular orbitals. Criteria like localization and filling of the transformed basis orbitals - sometimes paired with physical intuition - are essential for defining the correlated subspace. Comparison of the relevant energy scales, $\bar{\Gamma}_{\mathrm{AI}} \lesssim U$, shows whether a proper many-body treatment is required.

The noninteracting retarded Green's function in transformed space is given by

$$\bar{G}^0(\omega) = \frac{1}{(\omega + \mathrm{i}0^+)1 - \bar{H} - \bar{\Delta}^{\mathrm{L}}(\omega) - \bar{\Delta}^{\mathrm{R}}(\omega)} \tag{2.3.2}$$

where the transformed hybridizations of the electrodes are $\bar{\Delta}^i(\omega) = M^\dagger \Delta^i(\omega) M$ for $i \in \{\mathrm{L}, \mathrm{R}\}$.

The AI hybridization caused by the NI part and the electrodes is given by

$$\bar{\Delta}_{\mathrm{AI}}(\omega) = \bar{H}_{\mathrm{AI,NI}}\Big((\omega + \mathrm{i}0^+)1_{\mathrm{NI}} - \bar{H}_{\mathrm{NI}} - (\bar{\Delta}^{\mathrm{L}})_{\mathrm{NI}}(\omega) - (\bar{\Delta}^{\mathrm{R}})_{\mathrm{NI}}(\omega)\Big)^{-1}\bar{H}_{\mathrm{NI,AI}}\,. \tag{2.3.3}$$

$(\bar{\Delta}^{i})_{\mathrm{NI}}(\omega)$ for $i \in \{\mathrm{L},\mathrm{R}\}$ denotes the NI part of the hybridization. Eq. 2.3.3 assumes that there is no direct coupling between electrode orbitals and the AI which can be fulfilled in any case by choosing the size of the central region appropriate. The Hamiltonian $\bar{H}_{\mathrm{AI}}$ and the hybridization $\bar{\Delta}_{\mathrm{AI}}(\omega)$ are the ingredients to the AIM which we discuss in Sec. 2.3.3.

2.3.2 The case of nonorthogonal basis functions

In this section, we present the projection formalism to construct an AIM in a basis set of orthogonal orbitals starting from the KS Hamiltonian given in a basis set of nonorthogonal orbitals, e.g. pseudo-atomic orbitals. We apply the scheme presented in this section to the case of CuPc on Au(111) and Ag(111) in Chpt. 4. The present section is mainly adopted from Ref. [108] and includes a concise introduction to the approach proposed by Droghetti *et al.* [45] along with some modifications.

In a first step, the system is separated into a noninteracting (coherent) part and a strongly correlated part described by the AIM. Therefore, Droghetti *et al.* [45] divide the system into several regions (see Fig. 2.3). The left lead (L) couples to the so-called extended molecule (EM) which in turn is coupled to the right lead (R). The extended molecule is often also referred to as the central region. The leads are chosen such that there is no one-particle overlap between them. In our case, we choose the left lead being on the metal surface side and the right lead on the tip side of the system. The EM is further subdivided into: extended region (ER), interacting region (IR), and the Anderson impurity (AI), with EM $\supseteq$ ER $\supseteq$ IR $\supseteq$ AI.

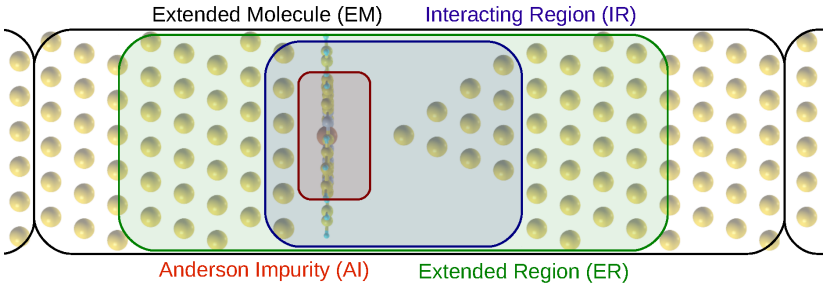

Figure 2.3: The schematic representation of the transport region consisting of left and right lead (only the surface layer are shown) and the extended molecule (EM, black), or rather the central region, with its subsystems: the extended region (ER, green), the interacting region (IR, blue), and the Anderson impurity (AI, red).

The IR includes all orbitals that may contribute to the AI. From the IR, we determine the AI by diagonalizing H_{IR} and selecting the correlated orbitals depending on their localization

and filling. Hence, the AI describes the strongly correlated orbitals for which a Hubbard interaction is taken into account. In addition to the actual molecule, we include orbitals from the tip as well as the first surface layer of the substrate to the IR. This allows the orthogonal correlated orbitals to extend into the tip or the surface. In the following, we have to construct an AI with basis functions orthonormal to the rest of the system. Therefore, we define the ER as consisting of all orbitals with finite overlap with the IR, including the IR itself. The set of remaining orbitals (which we denote as EM\ER) are split into two parts that couple to the left (α) or the right (β) lead, respectively.

Since DFT codes like SIESTA [84] use atomic orbitals, we have to take their nonorthogonality into account. The overlap matrix S and the one-particle Hamiltonian H of the EM have the structure

$$X = \begin{pmatrix} X_{\alpha\alpha} & X_{\alpha\mathrm{ER}} & X_{\alpha\beta} \\ X_{\alpha\mathrm{ER}}^\dagger & X_{\mathrm{ER}} & X_{\beta\mathrm{ER}}^\dagger \\ X_{\alpha\beta}^\dagger & X_{\beta\mathrm{ER}} & X_{\beta\beta} \end{pmatrix} \tag{2.3.4}$$

with X denoting either S or H. $X_{ij}^\dagger$ is the conjugate transpose of the block matrix X_{ij}. To project onto an AI that is orthogonal to all remaining orbitals, we have to find a transformation W that divides the ER into a noninteracting (NI) and an AI part such that

$$\bar{S} = W^\dagger S W = \begin{pmatrix} 1_{N_{\mathrm{AI}}} & 0 & 0 & 0 \\ 0 & S_{\alpha\alpha} & \bar{S}_{\alpha\mathrm{NI}} & S_{\alpha\beta} \\ 0 & \bar{S}_{\alpha\mathrm{NI}}^\dagger & \bar{S}_{\mathrm{NI}} & \bar{S}_{\beta\mathrm{NI}}^\dagger \\ 0 & S_{\alpha\beta}^\dagger & \bar{S}_{\beta\mathrm{NI}} & S_{\beta\beta} \end{pmatrix} \tag{2.3.5}$$

and

$$\bar{H} = W^\dagger H W = \begin{pmatrix} \bar{H}_{\mathrm{AI}} & 0 & \bar{H}_{\mathrm{AI,NI}} & 0 \\ 0 & H_{\alpha\alpha} & \bar{H}_{\alpha\mathrm{NI}} & H_{\alpha\beta} \\ \bar{H}_{\mathrm{AI,NI}}^\dagger & \bar{H}_{\alpha\mathrm{NI}}^\dagger & \bar{H}_{\mathrm{NI}} & \bar{H}_{\beta\mathrm{NI}}^\dagger \\ 0 & H_{\alpha\beta}^\dagger & \bar{H}_{\beta\mathrm{NI}} & H_{\beta\beta} \end{pmatrix}. \tag{2.3.6}$$

The block in the upper left corner describes the AI in basis functions orthogonal to each other and to the noninteracting (NI) orbitals describing the rest of the ER. Note that Hamiltonian and overlap matrix of EM\ER are unaffected by the transformation W, hence $\bar{X}_{ij} = X_{ij}$ for $i, j \in \{\alpha, \beta\}$.

W is neither unitary nor uniquely defined. One possibility to obtain it is the following procedure using three consecutive transformations W_1, W_2, and W_3 with $W = W_1 W_2 W_3$:

$$W = \begin{pmatrix} 0 & 1_{N_\alpha} & 0 & 0 \\ W_{\mathrm{AI}} & 0 & W_{\mathrm{NI}} & 0 \\ 0 & 0 & 0 & 1_{N_\beta} \end{pmatrix}. \tag{2.3.7}$$

In the first step, the AI is projected out using

$$W_1 = \begin{pmatrix} 0 & 1_{N_\alpha} & 0 & 0 \\ U_{\mathrm{ER}} & 0 & U_{\mathrm{NI}} & 0 \\ 0 & 0 & 0 & 1_{N_\beta} \end{pmatrix} \tag{2.3.8}$$

where U_{ER} consists of the contributions of the orbitals in IR to the impurity orbitals. U_{NI} is the identity matrix with removed columns at the indices of the impurity orbitals. The second step orthogonalizes the AI to all other orbitals in ER by changing the orbitals in NI.

$$W_2 = \begin{pmatrix} 1_{N_{\mathrm{AI}}} & 0 & -W_{\mathrm{SB}} & 0 \\ 0 & 1_{N_\alpha} & 0 & 0 \\ 0 & 0 & 1_{N_{\mathrm{NI}}} & 0 \\ 0 & 0 & 0 & 1_{N_\beta} \end{pmatrix} \tag{2.3.9}$$

with $W_{\mathrm{SB}} = \tilde{S}_{\mathrm{AI}}^{-1}\tilde{S}_{\mathrm{AI,NI}}$, $\tilde{S}_{\mathrm{AI}} = U_{\mathrm{ER}}^{\dagger}S_{\mathrm{ER}}U_{\mathrm{ER}}$, and $\tilde{S}_{\mathrm{AI,NI}} = U_{\mathrm{ER}}^{\dagger}S_{\mathrm{ER}}U_{\mathrm{NI}}$. To be precise, $\tilde{X} = \{\tilde{S}, \tilde{H}\}$ are the matrices after the first transformation step, i.e., $\tilde{X} = W_1^{\dagger}XW_1$, and $\tilde{S}_{\mathrm{AI}}$, $\tilde{S}_{\mathrm{AI,NI}}$, and $\tilde{H}_{\mathrm{AI}}$ are block matrices of $\tilde{S}$ and $\tilde{H}$, respectively. The third step diagonalizes $\tilde{S}_{\mathrm{AI}}$ and $\tilde{H}_{\mathrm{AI}}$. The AI basis functions are orthogonalized via a Löwdin transformation and $\tilde{H}_{\mathrm{AI}}$ is diagonalized by solving the eigenvalue problem

$$\tilde{S}_{\mathrm{AI}}^{-1/2}\tilde{H}_{\mathrm{AI}}\tilde{S}_{\mathrm{AI}}^{-1/2}U_{\mathrm{AI},\psi} = U_{\mathrm{AI},\psi}\bar{H}_{\mathrm{AI}} \, . \tag{2.3.10}$$

This results in the transformation

$$W_3 = \begin{pmatrix} W_{3,\mathrm{AI}} & 0 & 0 & 0 \\ 0 & 1_{N_\alpha} & 0 & 0 \\ 0 & 0 & 1_{\mathrm{NI}} & 0 \\ 0 & 0 & 0 & 1_{N_\beta} \end{pmatrix} \tag{2.3.11}$$

with $W_{3,\mathrm{AI}} = \tilde{S}_{\mathrm{AI}}^{-1/2}U_{\mathrm{AI},\psi}$.

The noninteracting retarded Green's function projected in the EM subspace is given by

$$G^0(\omega) = \frac{1}{(\omega + \mathrm{i}0^+)S - H - \Delta^{\mathrm{L}}(\omega) - \Delta^{\mathrm{R}}(\omega)} \, . \tag{2.3.12}$$

As the Green's functions are the inverse of the noninteracting Hamiltonian H in a one-particle basis, they have the same block-matrix structure given by either Eq. 2.3.4 in the original space or Eq. 2.3.6 in the transformed space. Under transformation W of the Hamiltonian, Green's functions transform with the inverse of W and therefore $\bar{G}(\omega) = W^{-1}G(\omega)W^{-1^{\dagger}}$. Hybridizations on the other hand transform like H, i.e., according to $\bar{\Delta} = W^{\dagger}\Delta W$. Especially, the Green's function of the ER transforms like

$$G_{\mathrm{ER}} = \left(W_{\mathrm{AI}}^{\dagger}, W_{\mathrm{NI}}^{\dagger}\right)\bar{G}_{\mathrm{ER}}\begin{pmatrix} W_{\mathrm{AI}} \\ W_{\mathrm{NI}} \end{pmatrix} \, . \tag{2.3.13}$$

For our analysis, we need the DOS projected on orbital ν of the nonorthonormal atomic basis of the ER obtained from TranSIESTA.

$$A_{\mathrm{ER},\nu}(\omega) = -\frac{1}{\pi}\Im\left(G_{\mathrm{ER}}(\omega)S_{\mathrm{ER}}\right)_{\nu\nu} \tag{2.3.14}$$

The atomic-element resolved DOS is obtained by summation over all basis functions belonging to the corresponding atom. Similarly, the total DOS is the sum over all projections, $A_{\mathrm{ER}}(\omega) = \sum_\nu A_{\mathrm{ER},\nu}(\omega)$.

The AI hybridization caused by NI, α, β and the electrodes is given by

$$\bar{\Delta}_{\mathrm{AI}}(\omega) = \bar{H}_{\mathrm{AI,NI}}\bar{g}_{\mathrm{NI}}(\omega)\bar{H}_{\mathrm{NI,AI}} \tag{2.3.15}$$

with $\bar{g}_{\mathrm{NI}}(\omega)$ being the NI part of the Green's function

$$\bar{g}_{\mathrm{B}}(\omega) = \left((\omega + \mathrm{i}0^+)\bar{S}_{\mathrm{B}} - \bar{H}_{\mathrm{B}} - (\bar{\Delta}^{\mathrm{L}})_{\mathrm{B}}(\omega) - (\bar{\Delta}^{\mathrm{R}})_{\mathrm{B}}(\omega)\right)^{-1} \tag{2.3.16}$$

where B = α+NI+β. $(\bar{\Delta}^i)_{\mathrm{B}}(\omega)$ for $i \in \{\mathrm{L}, \mathrm{R}\}$ denotes the B part of the electron hybridization. The Hamiltonian $\bar{H}_{\mathrm{AI}}$ and the hybridization $\bar{\Delta}_{\mathrm{AI}}(\omega)$ are the ingredients to the AIM which we discuss in the following section.

2.3.3 The Anderson impurity model

In the present section, we discuss the strongly correlated part, the AIM, more in detail. The Hamiltonian of the isolated impurity is

Anderson impurity:

$$\hat{H}_{\mathrm{AI}} = \sum_{ij\sigma}\left(\bar{H}_{\mathrm{AI},ij\sigma} - \delta_{ij}H^{\mathrm{dc}}_{i\sigma}\right)\hat{a}^\dagger_{i\sigma}\hat{a}_{j\sigma} + \hat{H}_{\mathrm{int}}, \tag{2.3.17}$$

where

$$\hat{H}_{\mathrm{int}} = \frac{1}{2}\sum_{ij\sigma}U_{ij}\hat{n}_{i\sigma}\hat{n}_{j\bar{\sigma}} + \frac{1}{2}\sum_{i\neq j,\sigma}V_{ij}\hat{n}_{i\sigma}\hat{n}_{j\sigma}\ .$$

Above, $\hat{n}_{i\sigma} = \hat{a}^\dagger_{i\sigma}\hat{a}_{i\sigma}$ is the particle number operator of orbital i and spin σ in second quantization with creation (annihilation) operators $\hat{a}^\dagger_{i\sigma}$ ($\hat{a}_{i\sigma}$). We also assumed that non-density-density terms are negligible. In the AIM, the impurity is coupled to a bath of noninteracting fermions:

Anderson impurity model:

$$\hat{H}_{\mathrm{AIM}} = \hat{H}_{\mathrm{AI}} + \sum_{ik\sigma}\tilde{V}_{ik}\left(\hat{a}^\dagger_{i\sigma}\hat{c}_{ik\sigma} + h.c.\right) + \sum_{ik\sigma}\epsilon_{ik}\hat{n}_{ik\sigma}\ . \tag{2.3.18}$$

$\hat{c}^\dagger_{ik\sigma}$ ($\hat{c}_{ik\sigma}$) are the creation (annihilation) operators of the kth bath state of orbital i with spin σ.

We have already determined $\bar{H}_{\mathrm{AI}}$ by use of the KS Hamiltonian via the transformation schemes presented in Secs. 2.3.1 and 2.3.2. Also the interaction parameters U_{ij} and V_{ij} can in principle be calculated from first principles, e.g. by employing CRPA or CLDA [109], respectively, but in the present thesis, we restrict ourselves to values from literature, existing

theoretical studies, and experimental evidence. For the double counting term $H^{\mathrm{dc}}_{i\sigma}$, we used the around mean field (AMF) double counting [110],

$$H^{\mathrm{dc}}_{i\sigma} = x_i \sum_j U_{ij} n^0_j + x_i \sum_{j \neq i} V_{ij} n^0_j \,, \tag{2.3.19}$$

where we introduced an orbital dependent factor x_i according to Ref. [111]. x_i is set to be one if not stated otherwise and n^0_j is the occupation of orbital j obtained from DFT. The hybridization function $\bar{\Delta}_{\mathrm{AI}}(\omega)$ given in Eq. 2.3.3 or Eq. 2.3.15, respectively, defines the bath parameters ϵ_{ik} and $\tilde{V}_{ik}$ via

$$\left\{\bar{\Delta}_{\mathrm{AI}}(\omega)\right\}_{ii} \stackrel{!}{=} \sum_k \frac{\tilde{V}^2_{ik}}{\omega + \mathrm{i}0^+ - \epsilon_{ik}} \,. \tag{2.3.20}$$

In this example, we neglect off-diagonal hybridizations $\left\{\bar{\Delta}_{\mathrm{AI}}(\omega)\right\}_{ij}$ for $i \neq j$. To clarify, for any given hybridization function $\bar{\Delta}_{\mathrm{AI}}(\omega)$, we have to find bath parameters such that Eq. 2.3.20 is satisfied.[1]

2.3.4 Solving the many-body problem

There are Hamiltonian based methods, such as exact diagonalization (ED) [112] and renormalization group techniques (e.g. NRG [113], DMRG [114]), and impurity Green's function based methods, such as perturbative approaches (e.g. NCA [115], IPA [116]) and continuous-time quantum Monte Carlo (CTQMC) methods [14].

In the next sections, we briefly introduce three selected impurity solver employed in the present thesis: (i) a solver based on ED and CPT, (ii) a CTQMC solver based on the strong-coupling hybridization expansion (CTHYB) [117], and (iii) the fork tensor product state (FTPS) solver [46].

Exact diagonalization

The basic principle of ED methods [112, 118] is to restrict the number of interacting and noninteracting sites such that the remaining system can be diagonalized numerically in many-body space, e.g. as presented in Sec. 2.1.5. Typically, the AIM consists of a few correlated sites coupled to an infinite bath of noninteracting fermions which is approximated in the ED method by a finite-size bath. Due to the truncated bath, ED suffers from finite-size artifacts.

In this thesis, we use the following ED approach. We calculate the atomic Green's function of the impurity sites by completely neglecting the bath and couple the bath afterwards using the coupling equation 2.1.43. This approximation, also known as CPT approximation, is justified close to equilibrium if the impuritiy sites couple weakly to the bath and is exact in the noninteracting case.

[1] We obtain the actual values of ϵ_{ik} and $\tilde{V}_{ik}$ by the following procedure. Starting from the hybridization $\left\{\bar{\Delta}_{\mathrm{AI}}(\omega)\right\}_{ii}$, we define equally spaced energy intervals I_k and represent each interval using a single bath site. ϵ_{ik} is then given by the center of this interval, while $\tilde{V}^2_{ik}$ is the area of $\left\{\bar{\Delta}_{\mathrm{AI}}(\omega)\right\}_{ii}$ in the given interval.

Continuous-time Quantum Monte Carlo in hybridization expansion

We give a brief summary of the CTHYB algorithm following Refs. [14, 119]. CTHYB is based on the expansion of the partition function

$$\mathcal{Z} = \mathrm{Tr}\left\{e^{-\beta\hat{H}_{\mathrm{AIM}}}\right\} = \mathrm{Tr}\left\{\mathcal{T}e^{-\beta\hat{H}_0}e^{-\int_0^\beta d\tau\hat{H}_{\mathrm{hyb}}(\tau)}\right\} . \tag{2.3.21}$$

Here, we use the interaction picture for $\hat{H}_{\mathrm{hyb}}$ in imaginary time τ, and therefore,

$$\hat{H}_{\mathrm{hyb}}(\tau) = e^{\tau\hat{H}_0}\hat{H}_{\mathrm{hyb}}e^{-\tau\hat{H}_0} . \tag{2.3.22}$$

The partition function can be expanded in a power series,

$$\mathcal{Z} = \sum_{n=0}^{\infty}\int_0^\beta d\tau_1 \ldots \int_{\tau_{n-1}}^\beta d\tau_n \ \mathrm{Tr}\left\{e^{-\beta\hat{H}_0}\hat{H}_{\mathrm{hyb}}(\tau_n)\ldots\hat{H}_{\mathrm{hyb}}(\tau_1)\right\} . \tag{2.3.23}$$

Writing $\hat{H}_{\mathrm{hyb}}(\tau)$ in terms of annihilation and creation operator and subsequently integrating out the noninteracting bath operators produces

$$\mathcal{Z} = \mathcal{Z}_{\mathrm{bath}}\sum_n\int d\tau_1\ldots d\tau_n \sum_{l_1\ldots l_n} \mathrm{Tr}\left\{e^{-\beta\hat{H}_0}\mathcal{T}o_{l_n}(\tau_n)\ldots o_{l_1}(\tau_1)\right\}\det\Delta . \tag{2.3.24}$$

The noninteracting bath partition function $\mathcal{Z}_{\mathrm{bath}}$ can be calculated analytically. The remaining bath contribution is in terms of the determinant of the hybridization function. The operators o_l are the creation and annihilation operators, respectively.

Now the problem lies in evaluating the sums and integrals which can be done by employing importance sampling. Let a configuration be one of the terms in the sums and integrals given by the information which operator acts at which time. In importance sampling, we want to sum up configurations with high contribution to the total sum. If we interpret the contribution to the total partition function divided by the total partition function as a probability density function (PDF), we can perform a Markov chain Monte Carlo process. Unfortunately, in general the single contributions to the total partition function are not positive. If a contribution is negative, it cannot be interpreted as a PDF. The trick to overcome this problem is to sample the modulus of the contribution and treat the sign in the observables. This approach suffers from the *sign problem* which can lead to exponentially scaling of the algorithm.

It turns out that the Green's function can be measured by reweighting the determinant. Within this thesis, we used the CTHYB implementation of the TRIQS/CTHYB package [120]. In summary, CTHYB is able to solve multi-orbital AIMs at finite temperature β statistically exact on the imaginary-time axis. For obtaining the Green's function on the real-time axis the analytic continuation (AC) has to be performed. We discuss the AC of imaginary-time Green's function data and the standard approach, the maximum entropy method (MEM), in Sec. 5.2. Within this thesis, we invented a novel approach called Bayesian parametric analytic continuation (BPAC) which we present in Chpt. 5.

Fork tensor product states

An impurity solver directly working in real time is the recently developed FTPS multi-orbital impurity solver [46, 47]. The algorithm was developed by Daniel Bauernfeind who also did the FTPS calculations for the AIM in this thesis. As the author of this thesis was not directly involved in applying the FTPS solver, we only introduce the most important aspects of this approach and refer the interested reader to Ref. [48] for a detailed explanation of the FTPS algorithm.

The FTPS solver uses a special tensor network representation of the many-body ground state:

$$|\Psi\rangle = \sum_{s_1,\ldots,s_N} c_{s_1,\ldots,s_N} |s_1,\ldots,s_N\rangle \ . \tag{2.3.25}$$

Tensor networks in general represent the rank-N tensor $c_{s_1\cdots s_N}$ as a product of tensors of much smaller rank. Matrix product states (MPS) are the simplest decomposition and represent the coefficient in a linear arrangement of tensors. FTPS reduce to MPS for a single orbital model, but are a more involved tensor network in the multi-orbital case. To solve the AIM it is necessary (i) to discretize the bath on the real-frequency axis with a large number of bath sites and (ii) to set up the tensor product operator encoding the many-body Hamiltonian. Then, density matrix renormalization group (DMRG) [114] is used to find the many-body ground state $|\psi_0\rangle$ by minimizing

$$E_0 = \min_{|\Psi\rangle} \frac{\langle\Psi|\,\hat{H}\,|\Psi\rangle}{\langle\Psi|\Psi\rangle} \ . \tag{2.3.26}$$

By real-time evolution, we obtain the retarded Green's function as

$$G_{ij}^{\mathrm{FTPS}}(t) = -i\Theta(t)\,\langle\psi_0|\,\{\hat{a}_i(t), \hat{a}_j^\dagger(0)\}\,|\psi_0\rangle\,. \tag{2.3.27}$$

Note that this implies that FTPS is a zero-temperature method. A subsequent Fourier transform to energy space gives access to the impurity spectral function

$$A_i^{\mathrm{FTPS}}(\omega) = -\frac{1}{\pi}\Im G_{ii}^{\mathrm{FTPS}}(\omega) \tag{2.3.28}$$

with

$$G_{ij}^{\mathrm{FTPS}}(\omega) = \int dt\ e^{i\omega t - \eta t} G_{ij}^{\mathrm{FTPS}}(t) \ . \tag{2.3.29}$$

The artificial broadening $\eta > 0$ is necessary to avoid finite size effects. In ω space such a broadening corresponds to a convolution with a Lorentzian of width η. Although this can have similar effects as a finite temperature, we emphasize that FTPS is a zero temperature method to calculate the $T = 0$ spectrum with broadened peaks.

2.3.5 Channel-resolved transmission

This section is mainly adopted from Ref. [108] and discusses how to separate the coherent part of the current, described by the Landauer-Büttiker formula, into three parts: (i) the

transmission T_{NI} of the NI region, (ii) the coherent transmission T_{AI} of the AI, and (iii) an interference term T_{I} between these two. We consider the transport system with the structure presented in Sec. 2.3.2 consisting of L, R, and the EM with its subdivisions. Obviously, the Landauer-Büttiker formula also holds in the transformed space obtained by the transformation matrix W and T_{coh} simplifies to

$$\begin{aligned} T_{\mathrm{coh}}(\omega) = &\ \mathrm{Tr}\left[\bar{\Gamma}^{\mathrm{L}}(\omega)\bar{G}(\omega)\bar{\Gamma}^{\mathrm{R}}(\omega)\bar{G}^{\dagger}(\omega)\right] \\ = &\ \mathrm{Tr}\left[\bar{\Gamma}^{\mathrm{L}}_{\mathrm{ER}}(\omega)\bar{G}_{\mathrm{ER}}(\omega)\bar{\Gamma}^{\mathrm{R}}_{\mathrm{ER}}(\omega)\bar{G}^{\dagger}_{\mathrm{ER}}(\omega)\right] \\ = &\ \mathrm{Tr}\left[\bar{\Gamma}^{\mathrm{L}}_{\mathrm{NI}}(\omega)\bar{G}_{\mathrm{NI}}(\omega)\bar{\Gamma}^{\mathrm{R}}_{\mathrm{NI}}(\omega)\bar{G}^{\dagger}_{\mathrm{NI}}(\omega)\right]. \end{aligned} \tag{2.3.30}$$

The second line holds since the block matrices $H_{\alpha\beta}$ and $S_{\alpha\beta}$ are negligible as α and β are spatially separated because the ER includes tip, molecule, and surface of the STM configuration. We can obtain the third line because the block matrices $\bar{H}_{x,\mathrm{AI}}$ and $\bar{S}_{x,\mathrm{AI}}$ with $x \in \{\alpha, \beta\}$ in Eqs. 2.3.5 and 2.3.6 are zero by construction, see W_2 in Eq. 2.3.9. $\bar{\Gamma}^{x}_{\mathrm{NI}}$ with $x \in \{\mathrm{L}, \mathrm{R}\}$ are obtained from their respective hybridization functions given by

$$\begin{aligned} \bar{\Delta}^{\mathrm{L}}_{\mathrm{NI}}(\omega) &= (\omega^{+}\bar{S}_{\mathrm{NI},\alpha} - \bar{H}_{\mathrm{NI},\alpha})(\omega^{+}\bar{S}_{\alpha\alpha} - \bar{H}_{\alpha\alpha} - \bar{\Delta}^{\mathrm{L}}_{\alpha\alpha}(\omega))^{-1}(\omega^{+}\bar{S}_{\alpha,\mathrm{NI}} - \bar{H}_{\alpha,\mathrm{NI}}) \\ \bar{\Delta}^{\mathrm{R}}_{\mathrm{NI}}(\omega) &= (\omega^{+}\bar{S}_{\mathrm{NI},\beta} - \bar{H}_{\mathrm{NI},\beta})(\omega^{+}\bar{S}_{\beta\beta} - \bar{H}_{\beta\beta} - \bar{\Delta}^{\mathrm{R}}_{\beta\beta}(\omega))^{-1}(\omega^{+}\bar{S}_{\beta,\mathrm{NI}} - \bar{H}_{\beta,\mathrm{NI}})\,. \end{aligned} \tag{2.3.31}$$

Here, we used the abbreviation $\omega^{+} = (\omega + \mathrm{i}0^{+})$. The Green's function

$$\bar{G}_{\mathrm{NI}}(\omega) = \bar{g}_{\mathrm{NI}}(\omega) + \underbrace{\bar{g}_{\mathrm{NI}}(\omega)\bar{H}_{\mathrm{NI,AI}}\bar{G}_{\mathrm{AI}}(\omega)\bar{H}_{\mathrm{AI,NI}}\bar{g}_{\mathrm{NI}}(\omega)}_{\Delta\bar{G}_{\mathrm{NI}}} \tag{2.3.32}$$

consists of two parts: the noninteracting Green's function $\bar{g}_{\mathrm{NI}}(\omega)$ and the hybridization with the interacting Green's function $\bar{G}_{\mathrm{AI}}(\omega)$. Inserting $\bar{G}_{\mathrm{NI}}(\omega)$ into Eq. 2.3.30 gives

$$\begin{aligned} T_{\mathrm{coh}}(\omega) = &\ \underbrace{\mathrm{Tr}\left[\bar{\Gamma}^{\mathrm{L}}_{\mathrm{NI}}(\omega)\bar{g}_{\mathrm{NI}}(\omega)\bar{\Gamma}^{\mathrm{R}}_{\mathrm{NI}}(\omega)\bar{g}^{\dagger}_{\mathrm{NI}}(\omega)\right]}_{T_{\mathrm{NI}}} + \underbrace{\mathrm{Tr}\left[\bar{\Gamma}^{\mathrm{L}}_{\mathrm{NI}}(\omega)\Delta\bar{G}_{\mathrm{NI}}(\omega)\bar{\Gamma}^{\mathrm{L}}_{\mathrm{NI}}(\omega)(\Delta\bar{G}_{\mathrm{NI}})^{\dagger}(\omega)\right]}_{T_{\mathrm{AI}}} \\ &+ \mathrm{Tr}\left[\bar{\Gamma}^{\mathrm{L}}_{\mathrm{NI}}(\omega)(\Delta\bar{G}_{\mathrm{NI}})^{\dagger}(\omega)\bar{\Gamma}^{\mathrm{R}}_{\mathrm{NI}}(\omega)\bar{g}_{\mathrm{NI}}(\omega)\right] + \mathrm{Tr}\left[\bar{\Gamma}^{\mathrm{L}}_{\mathrm{NI}}(\omega)\bar{g}^{\dagger}_{\mathrm{NI}}(\omega)\bar{\Gamma}^{\mathrm{R}}_{\mathrm{NI}}(\omega)\Delta\bar{G}_{\mathrm{NI}}(\omega)\right] \\ = &\ T_{\mathrm{NI}}(\omega) + T_{\mathrm{AI}}(\omega) + T_{\mathrm{I}}(\omega)\,. \end{aligned} \tag{2.3.33}$$

As claimed above, Eq. 2.3.33 separates the coherent transmission into the three parts $T_{\mathrm{NI}}(\omega)$, $T_{\mathrm{AI}}(\omega)$, and $T_{\mathrm{I}}(\omega)$. Additionally, we can rewrite the coherent transmission over the AI as

$$T_{\mathrm{AI}}(\omega) = \mathrm{Tr}\left[\bar{\Gamma}^{\mathrm{L}}_{\mathrm{AI}}(\omega)\bar{G}_{\mathrm{AI}}(\omega)\bar{\Gamma}^{\mathrm{R}}_{\mathrm{AI}}(\omega)\bar{G}^{\dagger}_{\mathrm{AI}}(\omega)\right] \tag{2.3.34}$$

with

$$\begin{aligned} \bar{\Gamma}^{\mathrm{L}}_{\mathrm{AI}}(\omega) &= \bar{H}_{\mathrm{AI,NI}}\bar{g}_{\mathrm{NI}}(\omega)\bar{\Gamma}^{\mathrm{L}}_{\mathrm{NI}}(\omega)\bar{g}^{\dagger}_{\mathrm{NI}}(\omega)\bar{H}_{\mathrm{NI,AI}} \\ \bar{\Gamma}^{\mathrm{R}}_{\mathrm{AI}}(\omega) &= \bar{H}_{\mathrm{AI,NI}}\bar{g}^{\dagger}_{\mathrm{NI}}(\omega)\bar{\Gamma}^{\mathrm{R}}_{\mathrm{NI}}(\omega)\bar{g}_{\mathrm{NI}}(\omega)\bar{H}_{\mathrm{NI,AI}}\,. \end{aligned} \tag{2.3.35}$$

2.4 The Kondo effect

One of the cooperative many-body phenomena in solid-state physics, the Kondo effect, receives increasing attention due to experimental techniques allowing unprecedented control over single-molecule junctions, as e.g. in STM experiments. In the present section, we work out some basics of the Kondo effect.

While Sec. 2.4.1 gives a historical introduction to the Kondo effect, we introduce the Anderson model in Sec. 2.4.2. In Sec. 2.4.3, we obtain the Kondo model, describing the low-energy physics of the Anderson model, by applying the Schrieffer-Wolff transformation. In Sec. 2.4.4, we summarize Anderson's scaling idea and obtain a formula for the Kondo temperature. We discuss the SU(4) Kondo effect in Sec. 2.4.5.

2.4.1 Introduction

At the beginning of this section, we give a brief introduction to the history of the Kondo effect composed of Refs. [35, 57, 61, 121]. In 1933 at Leiden University, de Haas *et al.* [122] found a curious resistance minimum at non-zero temperature in gold, copper and silver. In contrast, most metals have a monotonically decreasing resistivity with decrease of temperature due to phonon scattering. It turns out that the Kondo temperature - roughly speaking the temperature at the resistance minimum - completely describes the low-temperature electronic properties of the material. In 1964 the Japanese theorist Kondo [34] could explain this resistance minimum by considering the scattering from a magnetic ion that interacts with the spins of the conduction electrons. In calculating the scattering rate in perturbation theory, he derived that the resistance in the metal increases logarithmically when temperature is lowered which explains the upturn of the resistance at low temperatures. It turns out that his description is only correct above a certain temperature which became known as the Kondo temperature T_K. At zero temperature his solution shows an unphysical divergence, which became known as the Kondo problem. In 1969 Anderson and Yuval [123] came up with the idea of *scaling* in the Kondo problem and were able to predict properties of a real system close to zero temperature. Scaling means eliminating the higher order excitations perturbatively to give an effective model valid on a lower energy scale. In 1975 Wilson [113] found that numerical renormalization overcomes the shortcomings of conventional perturbation theory and confirmed Anderson's scaling ansatz. He proved that at temperatures well below T_K the magnetic moment of the impurity is screened entirely by the spins of the conduction electrons. In 1980 Andrei and Wiegmann [124, 125] discovered exact solutions to the Kondo model using the Bethe ansatz [126].

Nowadays, the Kondo effect receives increasing attention due to experimental techniques, e.g. STM experiments, allowing unprecedented control over Kondo systems. First STM measurements on the Kondo effect have been done in 1998 [38, 39]. In the meantime some spectacular experiments have been realized, e.g. the observation of the mirror image of the Kondo resonance of a Co impurity in one focal point of an ellipse of atoms [40]. Further-

more, there have been several suggestions and attempts to observe the Kondo cloud by STM experiments, e.g. by measuring Friedel oscillations [127] or by using quantum size effects by placing the molecules on the top of metal islands [128].

2.4.2 The Anderson model

In 1961 Anderson [13] proposed the simplest model of a magnetic impurity in a metal, the so-called Anderson model:

$$\hat{H}_{\text{Anderson}} = \underbrace{\sum_{\mathbf{k}\sigma} \epsilon_k \hat{n}_{k\sigma} + \overbrace{\sum_{\sigma} \epsilon \hat{n}_{f\sigma} + U \hat{n}_{f\uparrow} \hat{n}_{f\downarrow}}^{\hat{H}_{\text{AL}}}}_{\hat{H}_1} + \underbrace{\sum_{\mathbf{k}\sigma} \left[V(\mathbf{k}) \hat{c}^{\dagger}_{\mathbf{k}\sigma} \hat{f}_{\sigma} + V^*(\mathbf{k}) \hat{f}^{\dagger}_{\sigma} \hat{c}_{\mathbf{k}\sigma} \right]}_{\lambda \mathcal{V}} . \tag{2.4.1}$$

In Eq. 2.3.18, we already defined a multi-orbital version of the Anderson model. Remarkably, the Anderson model has widely spaced energy scales, e.g. the local-moment formation in the f electrons is at the energy scale $U = \mathcal{O}(1)$ eV and the Kondo effect is at the energy scale $k_{\text{B}}T_{\text{K}} = \mathcal{O}(1)$ meV. We want to discuss these two important aspects of the Anderson model, the local-moment formation and the Kondo effect, in the following paragraphs.

To understand first the formation of a localized magnetic moment, we take a look at the atomic-limit Hamiltonian $\hat{H}_{\text{AL}}$ defined in Eq. 2.4.1. The atomic-limit approximation is justified if the hybridization to the surrounding conduction electrons is rather small. $\hat{H}_{\text{AL}}$ preserves both, the number and the spin of the electrons, and therefore, we have the eigenstates $|0\rangle$, $|\uparrow\rangle$, $|\downarrow\rangle$ and $|\uparrow\downarrow\rangle$ with the corresponding eigenenergies 0, ϵ, ϵ and $2\epsilon + U$. If we consider the case $\epsilon < 0$ and $U > |\epsilon|$, the ground state is in the one-electron sector and we have a localized magnetic moment. The cost of removing or adding an electron from the magnetic state is given by the differences of the eigenenergies and gives rise to energy levels at ϵ and $\epsilon + U$, respectively. These resonances broadened by the hybridization of the surrounding conduction electrons can be seen in Fig. 2.4.

The Kondo effect only arises when there is hybridization of such a local moment with the surrounding conduction electrons. So-called exchange processes can take place that effectively flip the localized spin while simultaneously creating a spin excitation in the surrounding conduction electrons. Fig. 2.5 schematically shows one of those exchange processes. In the initial state (a) there is a spin-up electron on the localized impurity. Heisenberg's uncertainty principle allows the existence of the virtual state (b) for a very short time where an electron is taken from the localized impurity state and put onto an unoccupied state right above the Fermi level. Within this time scale another electron must tunnel from the Fermi sea to the localized impurity which leads to the final state (c) having an electron with opposite spin on the localized impurity. When such spin exchange processes happen, one finds that a new state - the Kondo resonance, also called Abrikosov-Suhl resonance [129, 130] - is generated right at the Fermi level, see Fig. 2.4.

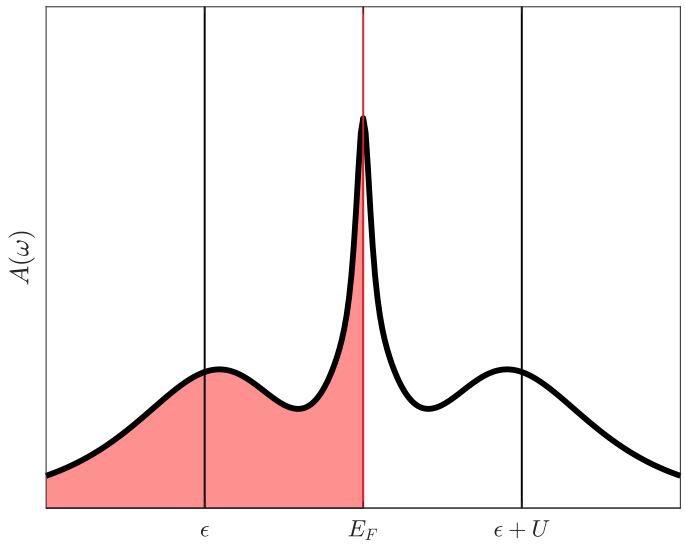

Figure 2.4: Spectral function of the Anderson model with the parameters $\epsilon = -1$ eV, $U = 2$ eV and $\Gamma = 0.5$ eV and at the temperature $k_{\mathrm{B}}T = 25$ meV. The spectral function shows resonances at ϵ and $\epsilon + U$ and the Fermi level E_{F}.

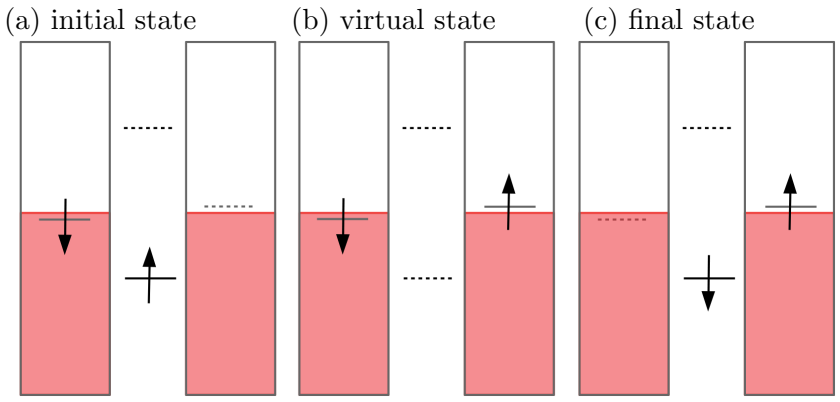

Figure 2.5: The magnetic impurity of the Anderson model (middle) contacted with metal (left and right). The atomic-limit solution of the localized impurity results in an occupied level with energy ϵ below the Fermi energy and a second level above the Fermi energy prohibited by the Coulomb energy U. In the initial state (a) the impurity is occupied with an spin-up electron which may tunnel outside the impurity by generating a classically forbidden virtual state (b) and then be replaced by a spin-down electron from the metal. In the final state (c) the impurity spin has effectively flipped compared to the initial state. This figure is redrawn from Ref. [121].

2.4.3 Schrieffer-Wolff transformation

In 1966 Schrieffer and Wolff [131] introduced a transformation to separate low- from high-energy physics. This is done by a one-step renormalization process to integrate out high-energy degrees of freedom and ends up at the Kondo model describing the low-energy physics of the AIM. In this section, we only offer the basic concept of the Schrieffer-Wolff transformation but refer to Refs. [35, 57, 131] for the detailed derivation of the Kondo model.

First, we divide the Hamiltonian into two terms:

$$\hat{H} = \hat{H}_1 + \lambda\mathcal{V} \qquad \text{with} \qquad \hat{H}_1 = \begin{pmatrix} \hat{H}_\mathrm{L} & 0 \\ 0 & \hat{H}_\mathrm{H} \end{pmatrix} \qquad \text{and} \qquad \mathcal{V} = \begin{pmatrix} 0 & \hat{V}^\dagger \\ \hat{V} & 0 \end{pmatrix} . \tag{2.4.2}$$

The Schrieffer-Wolff transformation is a canonical transformation that returns the Hamiltonian $\hat{H}$ to a block-diagonal form

$$\mathcal{U} \begin{pmatrix} \hat{H}_\mathrm{L} & \lambda\hat{V}^\dagger \\ \lambda\hat{V} & \hat{H}_\mathrm{H} \end{pmatrix} \mathcal{U}^\dagger = \begin{pmatrix} \hat{H}'_\mathrm{L} & 0 \\ 0 & \hat{H}'_\mathrm{H} \end{pmatrix} . \tag{2.4.3}$$

The renormalized Hamiltonian consists of the separated low-energy Hamiltonian $\hat{H}'_\mathrm{L}$ and high-energy Hamiltonian $\hat{H}'_\mathrm{H}$. Since $\mathcal{U}$ is unitary, we can write $\mathcal{U}$ in terms of an antihermitian action operator S with $\mathcal{U} = e^S$. Developing S in a power series in λ gives

$$S = \lambda S_1 + \lambda^2 S_2 + \dots . \tag{2.4.4}$$

Using this definition of S reduces Eq. 2.4.3 to

$$\begin{aligned} e^S \left(\hat{H}_1 + \lambda\mathcal{V}\right) e^{-S} =& \hat{H}_1 + \lambda\left(\mathcal{V} + [S_1, \hat{H}_1]\right) \\ &+ \lambda^2 \left(\frac{1}{2}[S_1, [S_1, \hat{H}_1]] + [S_1, \mathcal{V}] + [S_2, \hat{H}_1]\right) + \dots . \end{aligned} \tag{2.4.5}$$

By performing the transformation, we want to get the block-diagonal form of Eq. 2.4.3. $\hat{H}_1$ is already block-diagonal per definition, see Eq. 2.4.2. We eliminate the off-diagonal elements in leading order λ by requiring

$$[\hat{H}_1, S_1] = \mathcal{V} . \tag{2.4.6}$$

Since $[S_1, \mathcal{V}]$ is block-diagonal, we can choose $S_2 = 0$ to eliminate the off-diagonal elements up to second order λ^2, and therefore, the renormalized low-energy Hamiltonian becomes

$$\hat{H}'_\mathrm{L} = \hat{H}_\mathrm{L} + \Delta\hat{H}_\mathrm{L} + \mathcal{O}(\lambda^3) \quad \text{with} \quad \Delta\hat{H}_\mathrm{L} = \frac{1}{2}\lambda^2 P_\mathrm{L}[S_1, \mathcal{V}]P_\mathrm{L} \tag{2.4.7}$$

where P_L projects onto the low-energy subspace. Hence, by defining S from Eq. 2.4.6 we are able to calculate the low-energy Hamiltonian of the Anderson model which is the Kondo model.

Kondo model:

$$H_{\text{Kondo}} = \sum_{k\sigma} \epsilon_k \hat{c}^\dagger_{k\sigma} \hat{c}_{k\sigma} + J\,(\mathbf{s}\cdot\mathbf{S}) \qquad \text{with} \qquad \mathbf{s} = \sum_{\substack{kk'\\ \sigma\sigma'}} \hat{c}^\dagger_{k\sigma} \boldsymbol{\sigma}_{\sigma\sigma'} \hat{c}_{k'\sigma'} \tag{2.4.8}$$

Here, $\mathbf{S}$ is the impurity spin and $\mathbf{s}$ the local spin density of the conduction electrons and we assumed the coupling constant J to be k independent,

$$J = |V|^2 \left[\frac{1}{\epsilon + U} + \frac{1}{-\epsilon}\right] = -|V|^2 \frac{U}{(\epsilon + U)\epsilon}\,. \tag{2.4.9}$$

2.4.4 Poor man's scaling

The scaling concept was carried out by Anderson and Yuval [123] in 1969. This section very briefly introduces the crucial steps for deriving the Kondo temperature following Anderson's *poor man's* approach [132]. A detailed derivation is given in Ref. [57].

In a first step, we write the Kondo model as

$$H_{\text{Kondo}} = \sum_{|\epsilon_k|<D} \epsilon_k \hat{c}^\dagger_{k\sigma} \hat{c}_{k\sigma} + J(D) \sum_{|\epsilon_k|,|\epsilon_{k'}|<D} \hat{c}^\dagger_{k\sigma} \boldsymbol{\sigma}_{\sigma\sigma'} \hat{c}_{k'\sigma'} \cdot \mathbf{S} \tag{2.4.10}$$

where we introduced the finite bandwidth D of the conduction electrons and keep their density of states constant. The poor man's renormalization procedure follows the evolution of $J(D)$ that results from reducing D by $|\delta D|$ by progressively integrating out the electron states at the edge of the conduction band. In particular, poor man's scaling does not rescale the bandwidth to its original size after each renormalization. Using the renormalization procedure introduced in the previous section produces the scaling equation

$$J(D - |\delta D|) = J(D) + 2J^2\rho \frac{|\delta D|}{D} \tag{2.4.11}$$

which can be rewritten to

$$\frac{\partial g(D)}{\partial \ln(D)} = -2g(D)^2 \tag{2.4.12}$$

with the coupling constant $g = J\rho$. Separation of variables and integration from D_0 to D' produces for $g > 0$

$$g(D') = \frac{g_0}{1 - 2g_0 \ln(\frac{D_0}{D'})} = \left[2\ln\left(\frac{D'}{D_0 \exp\left(-\frac{1}{2g_0}\right)}\right)\right]^{-1}\,. \tag{2.4.13}$$

Most importantly, we can identify a relevant energy scale in the denominator of the argument of the logarithm: the Kondo temperature. g becomes an universal function of the ratio

between the finite band width D' and the new characteristic low energy scale T_K. In using Eq. 2.4.9 and $\Gamma/2 = \pi|V|^2\rho$, we get

$$T_\mathrm{K} = D_0 \exp\left(\frac{\pi\epsilon(\epsilon+U)}{\Gamma U}\right). \tag{2.4.14}$$

Refs. [35, 133] obtained the prefactor D_0 leading to

Kondo temperature:

$$k_\mathrm{B}T_\mathrm{K} = \frac{\sqrt{\Gamma U}}{2} \exp\left(\frac{\pi\epsilon(\epsilon+U)}{\Gamma U}\right). \tag{2.4.15}$$

2.4.5 SU(4) Kondo effect

In the previous sections, we discussed the Kondo effect occurring in the two spin degrees of freedom, the so-called SU(2) Kondo effect. More generally, the Kondo effect may occur in any degrees of freedom, e.g. purely in orbital degrees of freedom as shown in Ref. [134] for carbon nanotubes. An SU(4) Kondo effect occurs if the ground state of the system has a fourfold degeneracy, e.g. if there are two spin and two orbital degrees of freedom as in the double quantum dots studied in Refs. [135–138]. Filippone *et al.* [139] derived the SU(4) Kondo temperature via a path integral approach to be:

SU(4) Kondo temperature:

$$k_\mathrm{B}T_{\mathrm{K,SU(4)}} = U f\left(\frac{\epsilon}{U}\right)\left(\frac{-2\Gamma U}{\pi\epsilon(\epsilon+U)}\right)^{\frac{1}{4}} \exp\left(\frac{\pi\epsilon(\epsilon+U)}{2\Gamma U}\right) \tag{2.4.16}$$

with

$$f(x) = \left(-x(x+1)^3\right)^{\frac{1}{4}} \exp\left(g(x)\right)$$

and

$$g(x) = \frac{1}{4}\frac{3x-2}{x+2} - \frac{x^2}{2}\frac{(x^2+3x+3)}{(x+2)^2} \ln\left(\frac{2x+3}{x+1}\right).$$

Chapter 3

Benzenedithiolate with monoatomic Au and Pt electrodes

3.1 Introduction

The mechanically controllable break-junction (MCBJ) experiment on the benzenedithiolate (BDT) molecule carried out by Reed *et al.* [15] in 1997 is often considered as the first transport experiment in single-molecule junctions. Although the BDT molecule became a workhorse in the field of molecular electronics, there are severe discrepancies between experimental [15–21] and theoretical results [22–24]. To put it in a nutshell, the calculated conductances tend to be higher than the measured ones. Proposed reasons are the sensitivity of the conductance to the detailed geometry of the junction [25], hydration [26], passivation [27], and correlation effects [28–30].

In the present chapter, we study BDT contacted with monoatomic Au and Pt electrodes employing the DFT+NEGF method using maximally localized Wannier functions (MLWF) as presented in Chpt. 2. We refer to these transport systems as Au-BDT-Au and Pt-BDT-Pt, respectively. Although in MCBJ and scanning tunneling microscope (STM) experiments the formation of monoatomic Au chains has been demonstrated by several authors [140–144], we see the transport systems studied in the present chapter as toy models which we chose for the following reasons. From a practical point of view, using monoatomic chains as electrodes enables performing the Wannier transformation in a very controlled way. From a physical viewpoint, we chose these transport systems for four further reasons: (i) analyzing how transport is affected by low-dimensional electrodes, (ii) investigating the impact of the junction geometry on the conductance, which is more straightforward in these simplified systems, (iii) studying the influence of many-body effects, and (iv) validating the applicability of a single-level model as suggested by Refs. [21–23, 145].

Disregarding small changes which we made to preserve the structure of the thesis, this chapter is adopted from the article *First-principles molecular transport calculation for the benzenedithiolate molecule* published in New J. Phys. **19** 103007, October 2017 [146]. This work

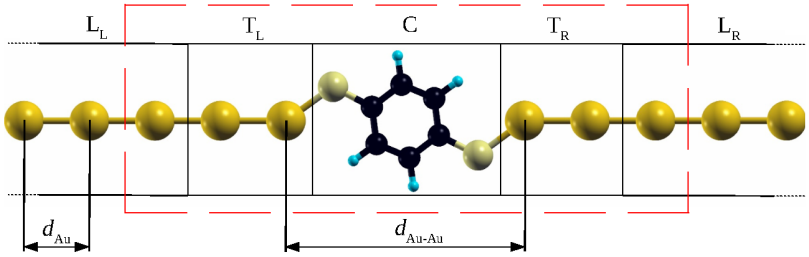

Figure 3.1: Molecular system consisting of a left and a right lead (L_L and L_R), transition layers (T_L and T_R), and the central region (C). The picture is drawn with XCrySDen [148]. Color code: C atoms, black; H atoms, blue; S atoms, light yellow; Au atoms, gold.

was carried out by Michael Rumetshofer and supervised by Lilia Boeri, Enrico Arrigoni, and Wolfgang von der Linden. Gerhard Dorn contributed to the discussion about the many-body effects. Starting point was the master thesis [79] written by Michael Rumetshofer where BDT between monoatomic Au chains was studied. The present article extends the investigations done in the master thesis to the case of monoatomic Pt chains as electrodes which is essentially the main part of the present article.

This chapter is organized as follows. In Sec. 3.2, we give the details of the calculation method. In Secs. 3.3 and 3.4, we study the Au-BDT-Au and Pt-BDT-Pt system, respectively. We give the conclusions in Sec. 3.5.

3.2 Methods

The systems we are considering consist of a central region (C), the BDT molecule, attached to left and right electrodes, also called leads, see Fig. 3.1. The two electrodes are further decomposed into L_L plus T_L on the left side and L_R plus T_R on the right. To determine the Kohn-Sham (KS) Hamiltonian of the system we employ density functional theory (DFT) using the pseudopotential plane-wave code Quantum Espresso [147]. The unit cell, red dashed line in Fig. 3.1, consists of the central region, left and right transition layers (T_L, T_R), also called buffer regions, and the surface part of the remaining electrodes (L_L, L_R). The size of the transition layers is chosen such that the electronic properties of the outermost atoms in the unit cell do not change anymore when the unit cell is increased. This ensures that the central region has negligible impact on the periodicity of the remaining electrodes. For all DFT calculations in this chapter we have used the Perdew-Zunger (PZ) [149] exchange correlation functional within the local density approximation (LDA) and non-relativistic ultrasoft pseudopotentials from the Standard Solid-State Pseudopotentials (SSSP) library (PSlibrary 0.3.1) [150]. According to Refs. [151, 152], we have used MLWF to get localized wave functions $\Psi_i(\mathbf{r})$ and the corresponding Hamiltonian. All Wannier transformations are done with wannier90 [83] which produces orthogonal MLWF.

For including electron interactions, we used a multi-orbital Anderson impurity model (AIM)

according to Sec. 2.3.3 with the impurity being the Wannier orbitals in the central region. In the present chapter, we refer to this approach as DFT+AIM to underline the AIM set ontop of the DFT calculation. The interaction parameters U_{ij} and $V_{ij} = (1 - \delta_{ij})\, U_{ij}$ are calculated numerically via the integral

$$U_{ij} = \int d^3r \int d^3r' \, |\Psi_i(\mathbf{r})|^2 \left|\Psi_j(\mathbf{r}')\right|^2 U(\mathbf{r}, \mathbf{r}') \tag{3.2.1}$$

with the screened Coulomb potential

$$U(\mathbf{r}, \mathbf{r}') = \frac{e^2}{4\pi\epsilon_0 \eta} \frac{1}{|\mathbf{r} - \mathbf{r}'|} \tag{3.2.2}$$

where η is a constant screening factor according to Ref. [153]. We use the AMF double counting presented in Eq. 2.3.19 and set the parameters $x_i = 1, \forall i$.

We calculate the current over the central region by using the Landauer-Büttiker formula which is an integral over the transmission consisting of a matrix product involving the full Green's function of the central region $G_{\mathrm{C}}(\omega)$ and the antihermitian parts of the hybridizations of the transition layers $\Gamma_{\mathrm{T_L}}(\omega)$ and $\Gamma_{\mathrm{T_R}}(\omega)$. We calculate $G_{\mathrm{C}}(\omega)$ within the cluster perturbation theory (CPT) approximation defined in Secs. 2.1.5 and 2.3.4, respectively. Remember that the Landauer-Büttiker formula is exact in the CPT approximation. The hybridizations of the transition layers $\Delta_{\mathrm{T_L}}(\omega)$ and $\Delta_{\mathrm{T_R}}(\omega)$ are obtained by, first, calculating the surface Green's functions of $\mathrm{L_L}$ and $\mathrm{L_R}$ using the method of Sancho *et al.* [87] and, subsequently, applying the coupling equation to calculate the Green's function of the transition layers $\mathrm{T_L}$ and $\mathrm{T_R}$.

Finally, we drive the system out of equilibrium by a bias voltage V_{b} that enters the calculation as a shift of the on-site energies and the chemical potential by $-V_{\mathrm{b}}/2$ for the left electrode and by $+V_{\mathrm{b}}/2$ for the right electrode. In the Landauer-Büttiker formula, V_{b} enters also in the Fermi functions. A gate voltage V_{g} is applied by shifting all on-site energies of the central region by V_{g}. We want to mention that applying bias and gate voltages in that way has the character of investigating a model system and is not a first-principle approach such as DFT+NEGF anymore. Most importantly, DFT+NEGF at finite gate and bias voltages would demand a nonequilibrium charge density self-consistency procedure as discussed in Sec. 2.2.3 which we neglect in this chapter for simplicity. Nevertheless, the finite bias and gate voltage calculations presented in this chapter reveal effects that may develop in a physical system.

3.3 The Au-BDT-Au system

In this section, we apply the DFT+NEGF method to the Au-BDT-Au system schematically drawn in Fig. 3.1. In a first step, we have performed DFT calculations[1] for a periodic chain

[1] We used a cut-off energy for the wave function of $E_{\mathrm{cowf}} = 64$ Ry and the charge density of $E_{\mathrm{con}} = 512$ Ry, the Methfessel-Paxton smearing technique with the smearing parameter $E_{\mathrm{sm}} = 0.01$ Ry, the vacuum distance $d_{\mathrm{vac}} = 12$ Å, and 32 k points.

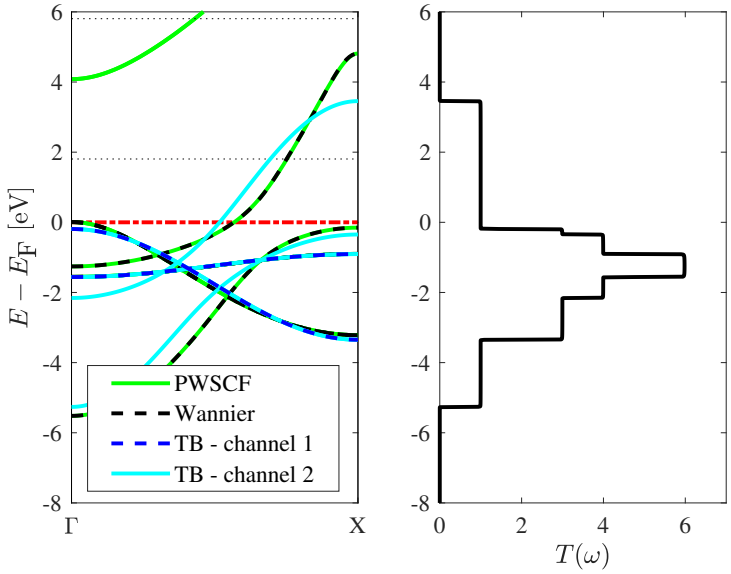

Figure 3.2: Construction of the one-particle Hamiltonian for the monoatomic Au chains. Left panel: plane-wave band structure (PWSCF), Wannier bands (Wannier), and nearest-neighbor tight-binding bands (TB). Right panel: transmission function calculated from TB.

of monoatomic Au. All the parameters are converged with respect to the total energy within 5 meV. In order to find the equilibrium geometry, we have calculated the total energy of the chain for different distances d_{Au} between the Au atoms. We find an optimal distance of $d_{\mathrm{Au}} = 2.515$ Å which is close to the DFT result 2.51 Å in Ref. [154].

The band structure of the Au chain in an interval around E_{F} is shown in the left panel of Fig. 3.2. The Γ-X axis is along the Au chain in reciprocal space. The $6p$ bands are at higher energies. The $6s$ and $5d$ bands coincide exactly with the Wannier bands which demonstrates the properness of the Wannier transformation. The dotted lines represent the inner and the outer energy window as described in Sec. 2.2.2 and are needed to disentangle the $6s$ and $5d$ bands from the $6p$ bands in the Wannier transformation. In Fig. 3.2 tight binding (TB) means that only hopping processes to nearest-neighbor Au atoms are taken into account. The $6s$ band and the $5d$ bands separate into the two bands corresponding to the d_{xz} and the d_{yz} orbital (channel 1) and four bands corresponding to orbitals with inversion symmetry with respect to the xy plane (channel 2). The definition of the coordinate system is according to Fig. 3.4(b). Each symmetry channel couples only to orbitals of the same symmetry and therefore transport takes place in two separated channels. The TB approximation turns out to be a good approximation for the channel 1 bands which are mainly interesting for transport. The right panel of Fig. 3.2 is the calculated equilibrium ($V_{\mathrm{b}} = 0$) transmission function for TB and is similar to the results obtained in Ref. [154]. In the coherent regime the transmission function is proportional to the number of bands at a certain energy.

After calculation of the Hamiltonian of the monoatomic Au chain, we considered the full

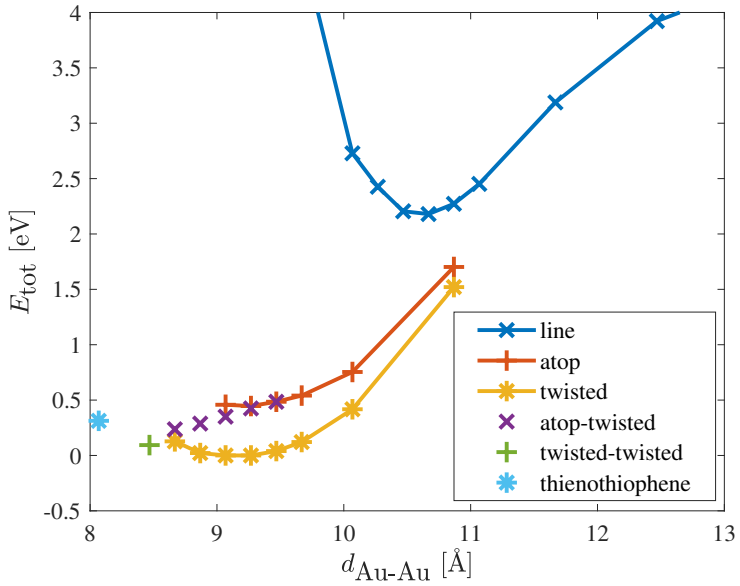

Figure 3.3: Total energy of the Au-BDT-Au system as a function of the distance between neighboring Au atoms and for different geometries. The total energy minimum is set to be at 0 eV.

system including BDT.[2] The BDT molecule can assume different geometry configurations between the two semi-infinite Au chains. In the *line* configuration the BDT molecule is forced to be on the Au-chain axis. In the *atop* configuration the BDT molecule slightly hops out of the Au-chain axis, while it twists out of the axis in the *twisted* configuration as shown in Fig. 3.1. There are also mixed configurations between atop and twisted, called *atop-twisted* and *twisted-twisted*. In order to determine the energetically favorable configuration, we compute the total energy as function of the distance between the Au atoms near to the BDT molecule $d_{\mathrm{Au\text{-}Au}}$, namely the gap between the two (left and right) semi-infinite Au chains, for different configurations, see Figs. 3.1 and 3.3. The distance between the Au atoms d_{Au} was fixed during the geometry optimizations. At $d_{\mathrm{Au\text{-}Au}} \approx 8.1$ Å, the BDT molecule rearranges into thienothiophene. It occurs that the twisted configuration of the BDT atom is energetically most favored and, consequently, we have chosen this configuration for the ensuing transport calculations. The optimized distance is $d_{\mathrm{Au\text{-}Au}} = 9.16$ Å. We have chosen 6 Au atoms per unit cell which ensures that the eigenvalues of the atoms at the outer edges of the unit cell (see Fig. 3.1) are converged within 0.05 eV.

The left panel in Fig. 3.4(a) depicts a comparison of the band structure obtained with the full plane-wave basis and with the Wannier basis. The Wannier transformation is performed only at the Γ point and picks out 47 bands: 35 corresponding to the 6 Au atoms and there are 12 BDT bands within this energy range. At the Γ point the PWSCF bands coincide

[2] We used a cut-off energy for the wave function of $E_{\mathrm{cowf}} = 100$ Ry and the charge density of $E_{\mathrm{con}} = 400$ Ry, the Methfessel-Paxton smearing technique with the smearing parameter $E_{\mathrm{sm}} = 0.001$ Ry, the vacuum distance $d_{\mathrm{vac}} = 18$ Å, and 1 k point.

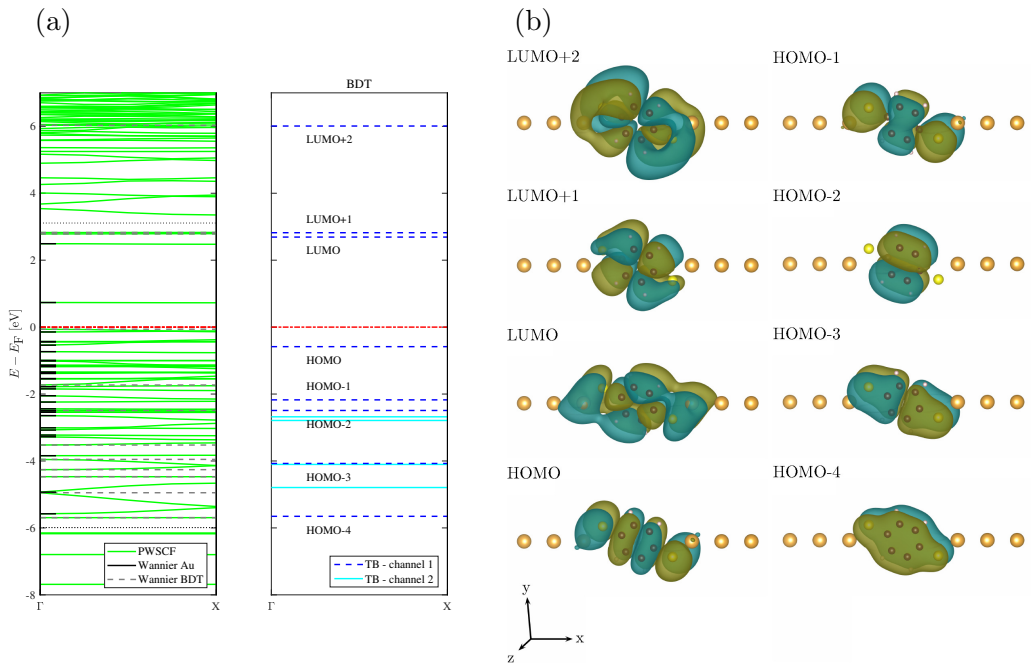

Figure 3.4: The plane-wave band structure (PWSCF) and the corresponding Wannier transformation (Wannier) ((a) left panel), and the eigenorbitals of BDT in channel 1 (b). The Wannier bands are projected onto atomic wave functions to show whether they correspond to the Au atoms (Au) or the BDT molecule (BDT). The levels of the decoupled BDT molecule split into channel 1 and channel 2 ((a) right panel). The eigenorbitals are drawn with VESTA [155].

exactly with the Wannier levels which demonstrates again the properness of the Wannier transformation. Additionally, the obtained Wannier basis functions of the Au atoms coincide with the Wannier basis functions of the pure Au chain which shows that the disentanglement procedure of the $6s$ and $5d$ bands from the $6p$ bands is done correctly. Projections of the wave functions onto atomic wave functions show whether the Wannier levels belong to the Au electrodes and the transition layers or to the BDT molecule. The right panel in Fig. 3.4(a) presents the eigenlevels of the decoupled BDT molecule. As mentioned above and outlined in Refs. [24, 25] transport takes place in separated channels. Channel 1 (blue dashed) consists of p_z-like BDT orbitals and channel 2 (cyan) of p_{xy}-like BDT orbitals. Each channel couples only to the corresponding channel in the Au electrodes.

The eigenorbitals of channel 1 are shown in Fig. 3.4(b). The shape of the orbitals can be explained by the symmetry of the benzene molecule which has the point group D_{6h}. LUMO+2 is the B_{2g} orbital, LUMO+1 and LUMO are the E_{2u} orbitals, HOMO-4 is the A_{2u} orbital and the others are a mixture of the benzene E_{1g} and the sulfur p_z orbitals. Due to the fact that only the HOMO level is close to the Fermi energy, the HOMO level should mainly contribute to transport, which is in general the case in systems with thiol anchoring groups, see Ref. [156]. The HOMO orbital we obtained is an unsaturated sulfur p orbital and can be compared to the HOMO orbitals obtained in Refs. [26, 157]. Passivation would shift the HOMO level away from the Fermi energy and produce lower conductances as demonstrated in Ref. [27]. But, in the Au-BDT-Au system we considered, charge transport through channel 1 is blocked due to the fact that there are no empty states with p_z-like symmetry in the monoatomic Au chain (only a *sd*-hybridized orbital belonging to channel 2 is above the Fermi level in Fig. 3.2). The levels corresponding to channel 2 are more than 2 eV below the Fermi energy, and therefore, transport in this channel is due to the broadening of the electrodes and the current-voltage characteristic is nearly linear. The conductivity for the BDT molecule contacted with monoatomic Au chains is almost constant and in the order of 0.01 G_0 for bias voltages below 4 V which is in the order of the experimental values presented in Refs. [17–20]. In contrast, according to Refs. [24, 25], using Au tips or bulk-like Au as electrodes produces empty states with p_z-like symmetry, and therefore, activates channel 1 which raises the conductance. Hence, the theoretical DFT result for the Au-BDT-Au system with bulk-like electrodes is 0.28 G_0 according to Ref. [27].

Since channel 1 contains the HOMO orbital, it would be the most important channel if supported by the electrodes. The coupling between electrodes and the channels depends on the geometry of the junction, and therefore, as mentioned above, Au tips or bulk-like Au as electrodes activate channel 1. Also the use of Pt instead of Au opens channel 1 because Pt has one electron less than Au, and therefore, also orbitals with p_z-like symmetry contribute to transport.

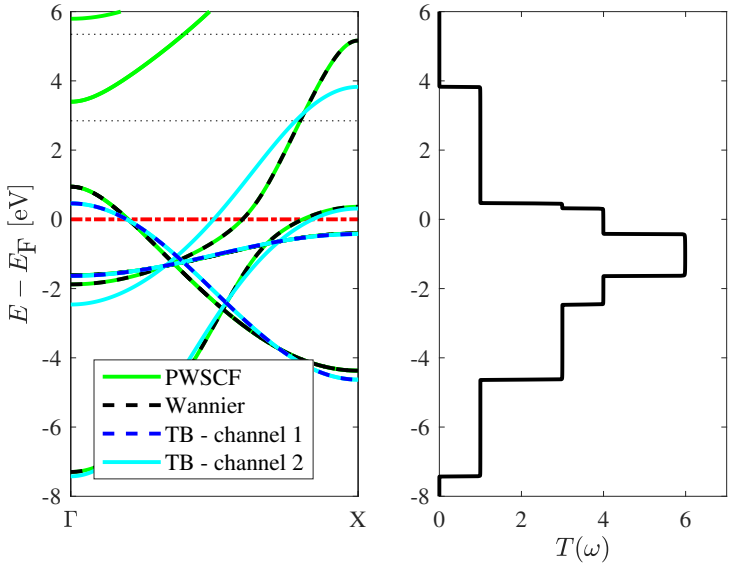

Figure 3.5: Construction of the one-particle Hamiltonian for the monoatomic Pt chains. Left panel: plane-wave band structure (PWSCF), Wannier bands (Wannier), and nearest-neighbor tight-binding bands (TB). Right panel: transmission function calculated from TB.

3.4 The Pt-BDT-Pt system

In order to activate channel 1, we have replaced the Au atoms by Pt ones in our calculations.[3] The optimized distance between the Pt atoms $d_{\mathrm{Pt}} = 2.328$ Å is comparable to the value of 2.34 Å in Ref. [158]. The plane-wave band structure, Wannier bands, and TB bands along with the transmission function are shown in Fig. 3.5. In the Pt chain, not just channel 2 but also channel 1 bands contribute to the equilibrium transmission at the Fermi energy.

We now consider the Pt-BDT-Pt system.[4] The optimized distance between the Pt atoms near to the BDT molecule is $d_{\mathrm{Pt\text{-}Pt}} = 8.58$ Å. It is necessary to take at least 8 Pt atoms per unit cell to ensure that the influence of the BDT molecule on the electrode Pt atoms is negligible. The comparison of the plane-wave band structure with the Wannier bands is given in the left panel of Fig. 3.6(a). In the Wannier transformation we retained 62 bands: 47 corresponding to the 8 Pt atoms and there are 15 BDT bands within this energy range. The right panel in Fig. 3.6(a) presents the decoupled levels of the BDT molecule and is comparable to Fig. 3.4(a) disregarding 3 more levels in channel 2 needed to get all the Pt levels in the calculation. In the following, we will only discuss channel 1 because due to the level alignment the current in channel 2 is an order of magnitude smaller. The eigenorbitals of channel 1 look similar

[3] We used a cut-off energy for the wave function of $E_{\mathrm{cowf}} = 60$ Ry and the charge density of $E_{\mathrm{con}} = 200$ Ry, the Methfessel-Paxton smearing technique with the smearing parameter $E_{\mathrm{sm}} = 0.005$ Ry, the vacuum distance $d_{\mathrm{vac}} = 12$ Å, and 60 k points.

[4] We used a cut-off energy for the wave function of $E_{\mathrm{cowf}} = 80$ Ry and the charge density of $E_{\mathrm{con}} = 320$ Ry, the Methfessel-Paxton smearing technique with the smearing parameter $E_{\mathrm{sm}} = 0.005$ Ry, the vacuum distance $d_{\mathrm{vac}} = 15$ Å, and 1 k point.

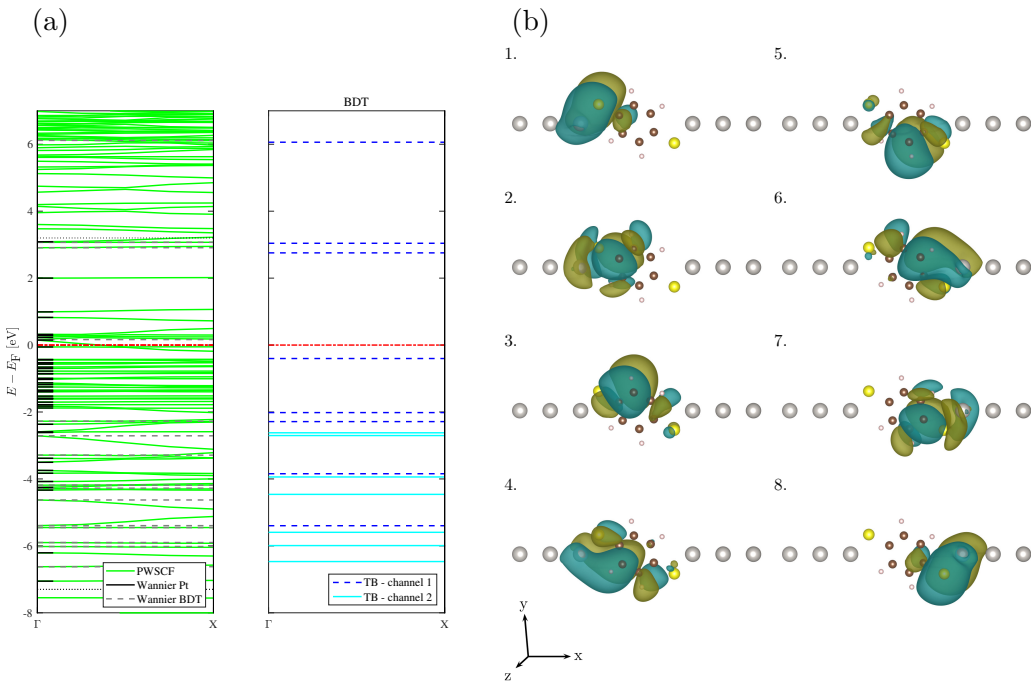

Figure 3.6: The plane-wave band structure (PWSCF) and the corresponding Wannier transformation (Wannier) ((a) left panel), and the localized Wannier orbitals of BDT in channel 1 (b). The Wannier bands are projected onto atomic wave functions to show whether they correspond to the Pt atoms (Pt) or the BDT molecule (BDT). The levels of the decoupled BDT molecule split into channel 1 and channel 2 ((a) right panel). The localized molecular orbitals are drawn with VESTA [155].

to the ones in the Au-BDT-Au calculation in Fig. 3.4(b). The orbitals in Fig. 3.6(b) are the localized Wannier orbitals of the BDT molecule in the Pt-BDT-Pt calculation. These are the 8 orbitals spanning the basis for the Hamiltonian of the central region. The matrix form of the Hamiltonian of the central region and the coupling matrices to the electrodes are given in Appendix A.1. The Fermi energy in the transport Hamiltonian is adjusted such that the local DOS of channel 1 of the atom further away from the BDT molecule has the same filling as in the pure atom chain.

The plot in the middle of Fig. 3.7 shows the spectral density $A_{\mathrm{C}}(\omega)$ of the isolated (continuous lines) and coupled (dash-dotted lines) BDT molecule. The curves labeled by DFT+AIM represent the result for the correlated system which will be explained in Sec. 3.4.2. The peaks in the DFT result (black continuous line) are at -0.4 eV, -2.0 eV, and -2.3 eV. As discussed above, the HOMO level closer to the Fermi level (-0.4 eV) is mainly responsible for transport. Coupling the BDT molecule to the electrodes (black dash-dotted line) strongly influences the levels at -0.4 eV and -2.0 eV which demonstrates that the system is in the strong-coupling regime. The spectral density at the surface atom of the left and the right electrode is shown in the left and the right panel of Fig. 3.7. The spectral density of a homogeneous multi-orbital chain is a superposition of semicircles, see $A_{\mathrm{LL}}(\omega)$ and $A_{\mathrm{LR}}(\omega)$. Coupling the homogeneous chains to the transition layers changes the semicircular structure of the spectral density. The spectral densities $A_{\mathrm{TL}i}(\omega)$ and $A_{\mathrm{TR}i}(\omega)$ are located i atoms away from the last point of the transition region, i.e. points with larger i are closer to the central region. We nicely see how the spectral function gradually changes from the multi-circular structure of the homogeneous chain to the structure of the spectral densities $A_{\mathrm{TL3}}(\omega)$ and $A_{\mathrm{TR3}}(\omega)$ which consists of peaks at -1.6 and -0.5 and a spike at about -1.3. The gray-shaded area indicates the filling. The remarkable point is that the spectral function of the transition region, that enters the transmission function and therefore the current, has a complex structure that will even change when a voltage is applied. As demonstrated by Cuniberti *et al.* [159, 160], low-dimensional electrodes can affect the conductance due to the finite band width and the structure in the DOS. If the DOS is nearly constant one can use the wide-band limit (WBL) approximation which works well for systems with bulk metal electrodes [161]. However the DOS of a one-dimensional chain has Van Hove singularities [162] near the band edge and the WBL approximation does not work. The key message therefore is that the details of the electrodes in such a molecular device are of crucial importance for the transport properties. This adds to the observation that the symmetry of the molecular orbitals and the electrodes can lead to selection rules as far as transport channels are concerned.

3.4.1 Stability diagrams

Next, we present various aspects of the charge stability of the Pt-BDT-Pt system. The stability diagram computed with DFT is presented in Fig. 3.8(a). We have restricted the bias voltage to -3 V$< V_{\mathrm{b}} < 3$ V because otherwise we would have to include Pt p orbitals, and likewise, we have restricted the gate voltage to the interval -2 V$< V_{\mathrm{g}} < 2$ V, otherwise channel 2 becomes important. Remember that applying bias and gate voltages in the way

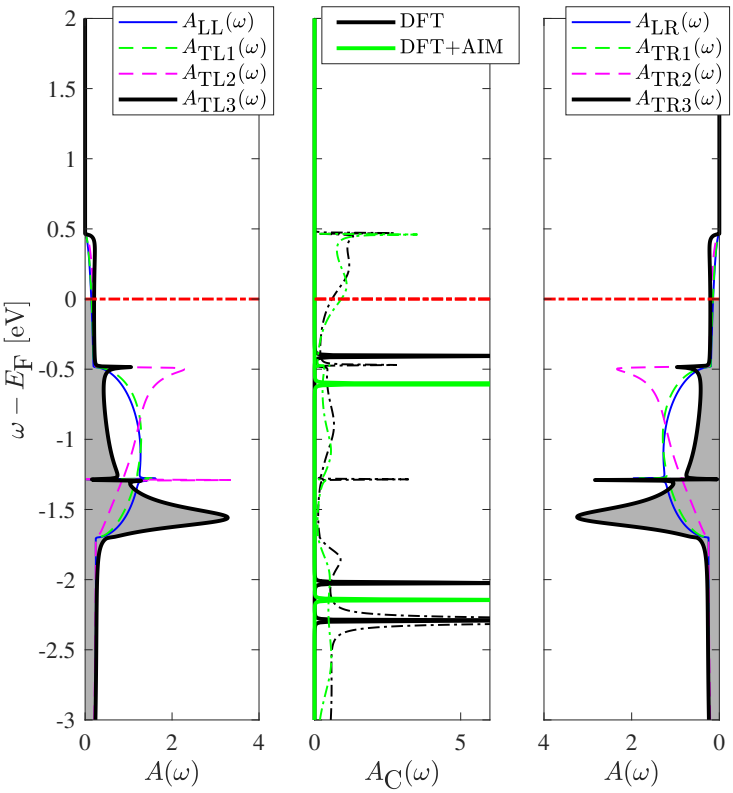

Figure 3.7: The colored lines represent the spectral function at different points in the transition region (first and third panel). The numbers in the indices stand for the distance of these points from the outermost edges of the transition region. The gray-shaded area indicates the filling. The spectral function of the central region (BDT molecule) is drawn in the middle panel for the isolated BDT (continuous lines) and the BDT coupled to the electrodes (dash-dotted lines).

presented in Sec. 3.2 has the character of investigating a model system since we neglect nonequilibrium charge density self-consistency; consequently, the finite bias and gate voltage calculations are no longer DFT+NEGF calculations anymore. Moreover, the application of voltages of that magnitude would cause additional effects, e.g., conformational changes due to charge redistribution, which we do not take into account in our calculations. All diagrams are calculated at an inverse electrode temperature of $\beta = 300$ 1/eV which enters in the Fermi functions of the electrodes.

The conductance at $V_\mathrm{b} = V_\mathrm{g} = 0$ is 0.52 G_0 and is considerable higher than the experimental (0.01 G_0 [17–20]) and theoretical DFT (0.28 G_0 [27]) values of various Au-BDT-Au systems. Beside the influence of the different contact material, the formation of monoatomic chains results in an increase of the conductance as suggested by Refs. [26, 140, 163]. The distance $d_{\mathrm{Pt\text{-}Pt}}$ is also small compared to experimental values where monoatomic chains arise under applying stress to the electrodes. This results in a higher coupling strength between the electrodes and the central region, and therefore, in a higher conductance.

Most strikingly, the stability diagram in Fig. 3.8(a) does not show the usual structure of crossing straight lines resulting in rhombic patterns. The only such structure is the pair of straight lines starting at the left edge of the diagram with $V_\mathrm{g} = 0.8$ and $V_\mathrm{g} = 1.3$, respectively. They correspond to the level at -2.3 eV. At $V_\mathrm{b} = 3$ the Fermi energy of the right electrode is shifted to $\mu = -1.5$. Above the Fermi level, the remaining DOS of unoccupied states has a width of $\Delta E_\mathrm{empty} = 0.5$ eV, see Fig. 3.7. Hence, the transport window of the right electrode is $(-1.5, -1.0)$ eV. With $V_\mathrm{g} = 0.8$, the level which was originally at -2.3 eV is shifted to the lower edge of the transport window and with $V_\mathrm{g} = 1.3$, it is shifted to the upper edge. This constant distance between the lines is an effect of the band edge according to which a positive conductance is always followed by a negative one: the *band-edge effect*. In our case, the distance between the lines along the V_b axis is $\Delta V_\mathrm{b} = 2\Delta E_\mathrm{empty} = 1$ eV. The factor two results from the fact that half of the bias voltage is applied to each electrode. The slope of the lines is constant and equal to $\pm 1/2$. If the electrodes are shifted with $\pm V_\mathrm{b}/2$, one needs $2V_\mathrm{b}$ to compensate a shift in V_g. The effects can be seen so clearly as a consequence of weak coupling of this level to the electrodes.

The levels at -2.0 eV and -0.4 eV produce a similar structure that can be explained by the band-edge effect and the *supporting effect*. To explain the supporting effect, we have projected out the level at -0.4 eV. The resulting charge stability diagram is depicted in Fig. 3.8(c). Comparison to the DFT calculation in Fig. 3.8(a) illustrates that in a broad range of V_g it is enough to use a single-level model for describing the transport through the BDT molecule; this is recommended by Refs. [21–23, 145]. The structure in the stability diagram is a consequence of the strong coupling to the electrodes. In the present case, the electrodes within channel 1 consist again of two nearly decoupled channels, the *supporting channel* and the *conducting channel*. The real (imaginary) parts R^L (Γ^L) of the retarded left electrode hybridization function $\Delta^{\mathrm{L,r}}$ for these two channels are shown in Fig. 3.9. Only the conducting channel has states above the Fermi level. The real part R^L shifts the levels in the central region. R^L of the supporting channel has anti-resonances at $\omega_1 = -0.5$ eV and $\omega_2 = -1.6$ eV. The spike at -1.3 eV is due to the small coupling between the channels in

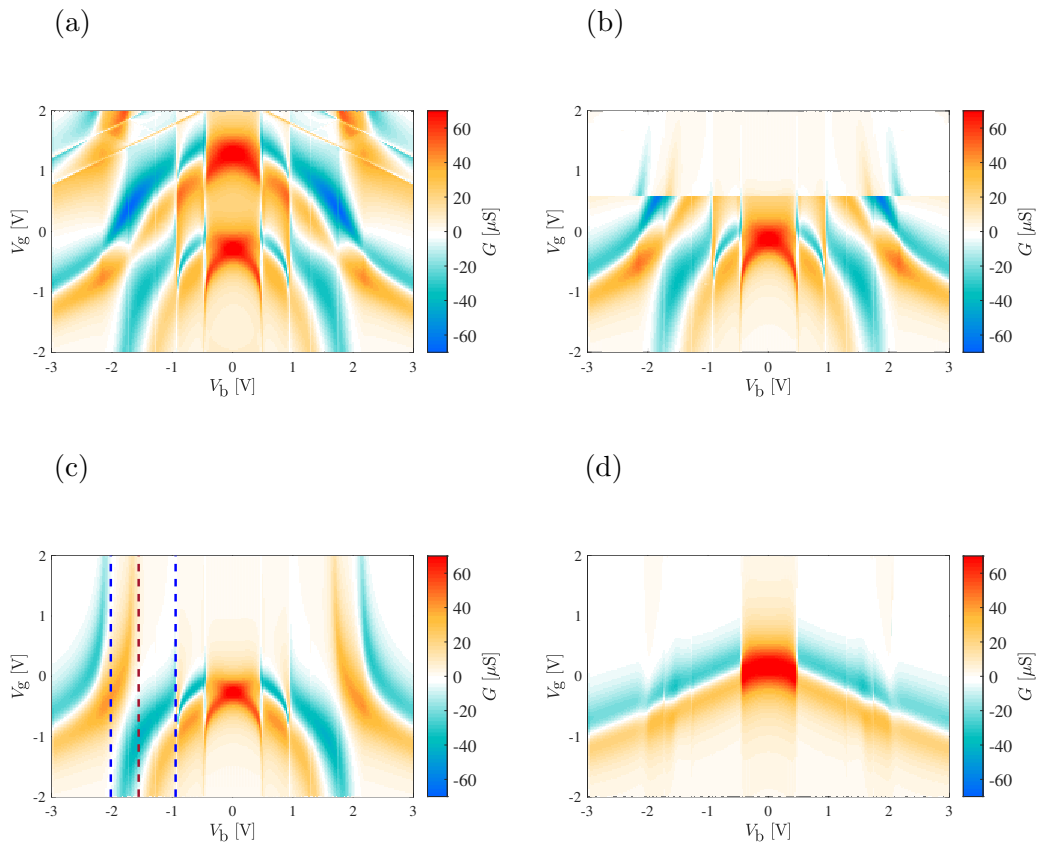

Figure 3.8: Charge stability diagram obtained with DFT (a) and DFT+AIM (b). Charge stability diagram obtained with the DFT result but projected onto the level at -0.4 eV (c), and additionally, with the supporting channel being manually blocked (d). We refer to the main text for a detailed interpretation of the stability diagrams.

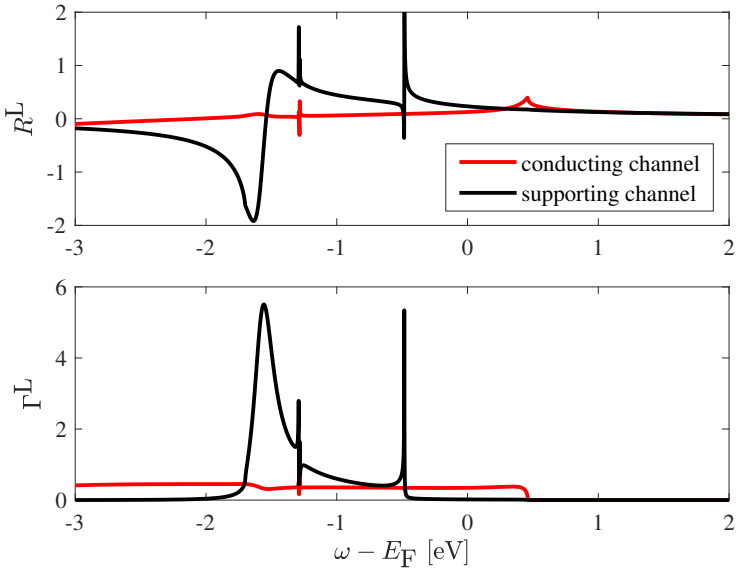

Figure 3.9: Real R^L and imaginary part Γ^L of the retarded left electrode hybridization $\Delta^{L,r}$.

the electrodes and its influence is negligible. The imaginary part Γ^L broadens the levels in the central region and has maxima at the anti-resonances in R^L. By the supporting effect we mean that at every V_b where the positive branch of an antiresonance of R^L hits the transport window of the opposite electrode, the energy level in the central region will be shifted up to higher energies, and therefore, one needs smaller V_g to compensate this and the conductivity structure in the stability diagram bends down, see Fig. 3.8(c). The blue dashed lines show the case where the positive branches of the anti-resonances of R_L hit the upper edge of the opposite electrode,

$$\begin{aligned} \omega_1 - \frac{V_b}{2} &= \Delta E_{\text{empty}} + \frac{V_b}{2} \\ \omega_2 - \frac{V_b}{2} &= \Delta E_{\text{empty}} + \frac{V_b}{2} \,, \end{aligned} \tag{3.4.1}$$

and act as limit where the effect is maximal. The same effect but with opposite sign happens if a negative branch of an antiresonance of R^L hits the transport window of the opposite electrode; there the conductivity structure in the stability diagram bends up. The red dashed line in Fig. 3.8(c) shows the case where the negative branch of the anti-resonances of R^L hits the lower edge of the transport window, the Fermi energy, of the opposite electrode,

$$\omega_2 - \frac{V_b}{2} = +\frac{V_b}{2} \,. \tag{3.4.2}$$

There the structure in the stability diagram is maximally bent up. The supporting effect explains the appearance of more than one maximum in the current voltage characteristic even if there is only a single level in the central region.

The interval $-\Delta E_{\text{empty}} < V_b < \Delta E_{\text{empty}}$ shows the usual structure of a stability diagram but smeared out due to the coupling of the electrodes. Disabling the supporting channel

Level	Energy [eV]	Spin [$\hbar$]	Level	Energy [eV]	Spin [$\hbar$]
10_g	-203.08	0			
$10'$	-200.81	1	9_g	-202.48	1/2
$10''$	-200.24	1	$9'$	-200.95	1/2
$10'''$	-200.11	0	$9''$	-199.46	1/2

Table 3.1: Many-body eigenenergies of the central region in case of Pt-BDT-Pt.

produces the stability diagram in Fig. 3.8(d) where the structure can be explained just by the band-edge effect.

3.4.2 Many-body effects

After having discussed the properties of the one-particle part of the Hamiltonian, we now include many-body effects using DFT+AIM explained in Sec. 3.2. The interaction parameters U_{ij} are determined by numerical integration of Eq. 3.2.1 and are listed in Appendix A.1. We take a constant screening parameter $\eta = 1.5$ as proposed by Ref. [153]. The values obtained in our calculation for the nearest-neighbor hopping between the carbon atoms within benzene in Eq. A.1.2 and the on-site Hubbard interaction in Eq. A.1.4 are comparable to those reported in Ref. [164].

In Tab. 3.1, the lowest many-body eigenenergies of the isolated central region are listed. The ground state (10_g) is in the 10-particle sector and is a singlet state. The other low-lying states in the 10-particle sector have singlet or triplet symmetry. The lowest eigenenergies in the 9-particle sector are doublet states. In principle, including interaction shifts levels and spectral weight away from the Fermi energy and produces additional peaks, and therefore, signatures in the current-voltage characteristic at higher voltages. Therefore, the benzene band gap increases compared to the DFT calculation presented in Ref. [165] and can cause a reduction of the current. In the Pt-BDT-Pt transport system, adding the full interaction shifts the HOMO level down to -0.6 eV, see DFT+AIM result in Fig. 3.7. The peaks obtained by this calculation can be identified with the excitations obtained by diagonalizing the many-body Hamiltonian of the central region. There is a peak at -0.6 eV corresponding to the excitation from the 10_g to the 9_g state. The next peak is at -2.1 eV and corresponds to the excitation from the 10_g to the $9'$ state.

The stability diagram obtained by including electron-electron correlations within DFT+AIM does not change qualitatively for $|V_g| < 0.6$ eV compared to the DFT result, see Figs. 3.8(a) and (b). The drastic change at $V_g = 0.6$ eV is an artifact of CPT which happens due to using the ground state of the isolated central region for each V_g to build up the local interacting Green's function independent of the applied V_b. At $V_g = 0.6$ eV, the HOMO level gets depleted, and therefore, the particle sector changes. We expect that when using more sophisticated nonequilibrium approaches, such as the ME+CPT calculation demonstrated in Ref. [166], the drastic change at $V_g = 0.6$ eV disappears. The conductance at $V_b = V_g = 0$ of $0.86\ G_0$ is higher than the result obtained with DFT even though the HOMO is shifted down

in energy and has less spectral weight. In the DFT+AIM calculation the spectral weight on the HOMO level is lower but distributed in a way that there is more weight in the orbitals near to the electrodes which causes the higher conductance. Strange *et al.* [27] have obtained the same trend at the BDT molecule connected with Au tips and studied with DFT and GW. In contrast to Ryndyk *et al.* [153], the electrode coupling effects overcome the influence of strong electron correlations in our transport system because of stronger coupling between electrodes and BDT due to the geometry of the transport system.

3.5 Conclusions

We have performed first-principle calculations based on DFT, MLWF, NEGF and CPT to study the molecular system consisting of BDT connected to semi-infinite monoatomic Au and Pt electrodes. DFT within the plane-wave pseudopotential method is used to calculate the electronic band structure of the transport system. Transforming the Kohn-Sham eigenvalues and eigenfunctions to a real-space basis of MLWF allows to extract a Hamiltonian to model the transport system. The NEGF method is used in turn to calculate the charge transport through the BDT molecule. In the case of Au electrodes, the HOMO level, which usually provides the dominant contribution to transport properties, does not contribute to transport due to symmetry reasons, and therefore, the conductance is small. Pt electrodes, on the other hand, enable transport via the HOMO level. Strong electron correlations are included on the BDT molecule using a multi-orbital AIM. Since the coupling between electrodes and molecule is large in the Pt-BDT-Pt system, the spectral properties of the electrodes are of importance and their influence on transport overcomes the influence of many-body effects to a large extend. We find that the *band-edge effect* and the *supporting effect* are more relevant than strong electron correlations for the structure of the stability diagram at small gate and bias voltages.

Chapter 4

Copperphthalocyanine on Au(111) and Ag(111)

4.1 Introduction

Copper phthalocyanines (CuPc) are magnetic organic semiconducting molecules with a brilliant blue color [167, 168]. The molecular structure of an isolated CuPc molecule is shown in Fig. 4.1(a). The electronic properties of transition metal phthalocyanines (TMPc) in general have been studied extensively in several environments using different methods, in both, experiment and theory, e.g., pristine CuPc [169, 170], TMPc between monoatomic chains [171–173], and TMPc on metal surfaces [42, 44, 174–185]. In the case of TMPc on metal surfaces, the arising physics depends strongly on the type of the transition metal; early and intermediate TM(II) ions (Mn, Fe, Co) have vacant d orbitals projecting out of the molecular plane and hybridizing with the substrate states, while later TM(II) ions (Ni, Cu) have unoccupied or semi-occupied $d_{x^2-y^2}$ orbitals confined in the molecular plane and therefore less hybridizing with the substrate orbitals [186, 187]. In several of these systems one of the cooperative many-body phenomena in solid state physics, the Kondo effect [34–37], has been observed, especially also for CuPc on Ag(100) [41] and Ag(111) [43].

To keep this chapter self-contained, we mainly adopted the same texts and figures as used for the article *First-principles quantum transport simulation of CuPc on Au(111) and Ag(111)* published in Phys. Rev. B **99** 045148, January 2019 [108]. This work is carried out by Michael Rumetshofer and Daniel Bauernfeind and is supervised by Wolfgang von der Linden. Michael Rumetshofer carried out the entire simulation, with the exception of solving the Anderson impurity model (AIM), which was carried out by Daniel Bauernfeind. All authors contributed to the discussions and conclusions.

This chapter is structured as follows. In Sec. 4.2, we give an overview about the current knowledge on CuPc on Au(111) and Ag(111) and discuss novel contributions made within this thesis. While Sec. 4.3 presents the methods and calculation details, the obtained results for CuPc on Au(111) and Ag(111) are given in Sec. 4.4. Finally, in Sec. 4.5, we give the

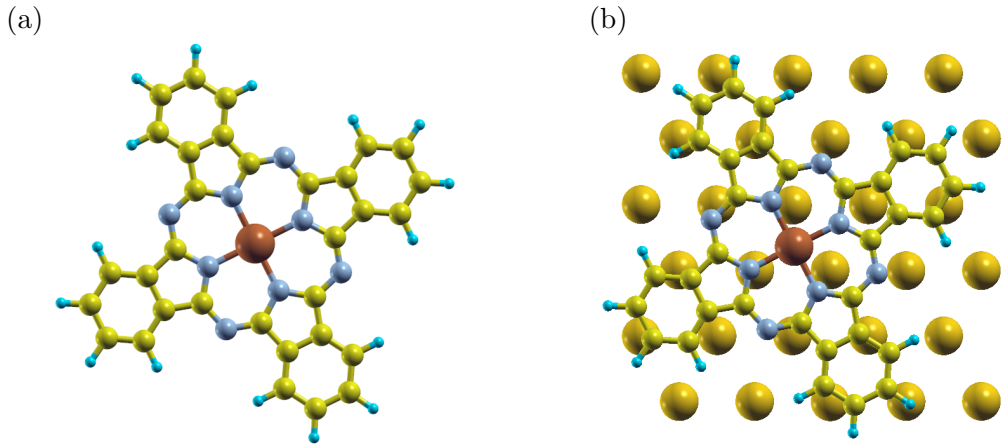

Figure 4.1: An isolated CuPc molecule (a) and the position of the CuPc molecule on the Au(111) surface (b). The pictures are drawn with XCrySDen [148]. Color code: C atoms, yellow; H atoms, cyan; N atoms, gray; Cu atom, red; Au atoms, gold.

conclusions.

4.2 Current knowledge and novel contributions

In the gas phase, the TM in TMPc binds to four isoindole ligands leaving the ion in a $[TM]^{2+}$ state. The molecule itself has a square planar D_{4h} symmetry, and hence, the TM d states transform as b_{2g} (d_{xy}), b_{1g} ($d_{x^2-y^2}$), a_{1g} (d_{z^2}), and e_g (d_{xz}, d_{yz}). Depending on their symmetry and energetic position, these orbitals hybridize to a different degree with p orbitals of the C and N atoms. In the gas phase, CuPc has a total spin $S = 1/2$ due to one unpaired electron in the b_{1g} state. The highest occupied and lowest unoccupied molecular orbital (HOMO and LUMO) are delocalized a_{1u} and $2e_g$ π orbitals with marginal contributions from the TM d states and therefore mainly located at the Pc. If the molecule is adsorbed on Ag(100), see e.g. Ref. [41], surface charge transfer from the metal surface to the $2e_g$ states generates another unpaired spin $S = 1/2$ located at the Pc. Therefore, in the adsorbed molecule one finds two weakly interacting spins, one localized on the Cu orbitals (b_{1g} state) and the other induced in the Pc ($2e_g$ states), leading to singlet ($S = 0$) and triplet ($S = 1$) states of the molecule. Such a charge transfer between the surface and the $2e_g$ states does not occur in CuPc on Au(111) [44], where the molecule remains in the doublet ($S = 1/2$) state.

Photoelectron spectroscopy (PES) measurements for CuPc on Au(111) and Ag(111) show a sharp structure at the Fermi energy for CuPc on Ag(111) but not for CuPc on Au(111), see Refs. [43, 44]. A Kondo scenario in the $2e_g$ states is suggested to be the possible origin. Mugarza *et al.* [41, 42] measured the differential conductance of CuPc on Ag(100) at different tip positions of the scanning tunneling microscope (STM) and found a Kondo resonance in the $2e_g$ orbitals and estimated the Kondo temperature to $T_K = 27 \pm 2$ K. Korytár *et al.* [188] performed density functional theory (DFT) calculations for CuPc on Ag(100) using

localized Wannier functions and employing the non-crossing approximation (NCA) to solve the impurity problem describing the $2e_g$ states plus exchange interaction with the single occupied b_{1g} state. Korytár *et al.* [188] were not able to estimate the Kondo temperature from their *ab initio* calculations and state that the underlying reason for this is the DFT level misalignment due to the lack of Coulomb repulsion. Here, we will present evidence that the hybridization strength is an important reason for the discrepancy of the Kondo temperature found in experiment and theory. It is well known that the Kondo temperature depends sensitively (exponentially) on the hybridization strength with the environment. Since the latter depends on the adsorption geometry of the molecule on the respective metal surface, reliable estimates for the Kondo temperature can only be found if the correct geometry for the underlying DFT calculation is used.

In this thesis, we calculate the transport properties of CuPc on Au(111) and Ag(111) from first principles to determine a simplified model sufficient for the description of the system. This is important in order to predict situations where the Kondo effect can be observed as well as its properties: Kondo temperature, symmetry, involved orbitals. Especially possibilities for the experimental observation of the Kondo cloud are a longstanding question [127, 128, 189, 190] where *ab initio* calculations can help to gain deeper understanding. Contrary to Korytár *et al.* [188], for our calculations we use the optimized adsorption geometry obtained by Huang *et al.* [44] and we check that our (many-body) spectral function is consistent with the density of states (DOS) obtained by Heyd-Scuseria-Ernzerhof (HSE) [191] DFT calculations and by ultraviolet photoemission spectroscopy (UPS) experiments performed in Ref. [44]. Taking additionally into account the error propagation of the incoming parameters, this allows us to estimate the order of the Kondo temperature from first principles. To include many-body effects, we apply the method presented in Sec. 2.3.2 to construct an effective AIM. For CuPc on Au(111), this yields a single-orbital AIM for the copper b_{1g} orbital. In the case of CuPc on Ag(111), we obtain a three-orbital AIM for the copper b_{1g} and the two nearly degenerate $2e_g$ orbitals mainly located at the Pc. Due to the negligible hybridization of the b_{1g} orbital with the remaining orbitals, it can be treated in the atomic limit. The resulting exchange coupling to the $2e_g$ orbitals can then be accounted for in mean-field approximation. Eventually, this leads to an effective spin-dependent energy shift for the electrons in the $2e_g$ states. For the many-body treatment of the physics in the nearly degenerate $2e_g$ orbitals, we use the the fork tensor product state (FTPS) solver described in Sec. 2.3.4. Our calculations yield a reliable *ab initio* estimate of the Kondo temperature and reproduce the qualitative behavior of the differential conductance found in the STM measurements in Refs. [41, 42].

4.3 Method and computational details

While we give the density functional calculation details in Sec. 4.3.1, Sec. 4.3.2 gives the details for the many-body treatment of the correlated subspace.

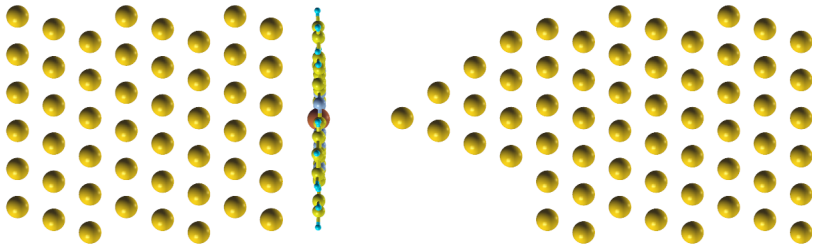

Figure 4.2: Two-dimensional cut through the central region for the simulation of the CuPc molecule sandwiched between an Au(111) substrate and the STM tip. The picture is drawn with XCrySDen [148].

4.3.1 Density functional calculations

To determine the one-particle part of the Hamiltonian, we perform DFT calculations for CuPc on Au(111) and Ag(111), respectively, in STM configuration. In such an STM configuration the CuPc molecule is sandwiched between the (111) surface of the Au/Ag substrate and an STM tip, see Fig. 4.2. The molecule lies in the xy plane which is defined by the surface of the substrate. The z axis, perpendicular to the surface, defines the transport direction. To model the tip, we use a tetrahedron attached to a three-dimensional semi-infinite system, both of the same material.

For the transport calculations, the system is split into a central region and two leads. The central region, displayed in Fig. 4.2, consists of the CuPc molecule, the actual tip, and eight layers of the substrate material on each side. On both sides, this central region is attached to the residual parts of the semi-infinite systems, which we will denote as leads (not shown in Fig. 4.2).

For the DFT calculation, it is necessary to have a periodic system in the xy plane, which is therefore split into appropriate unit cells. According to Ref. [44], we use a lattice constant of 4.18 Å for Au and 4.15 Å for Ag and p(6×5) Au(111) and Ag(111) surfaces. We chose the tip material to be the same as the surface, i.e., an Ag tip for the Ag(111) surface and an Au tip for the Au(111) surface. We want to emphasize though that one could also use any other tip material. To reduce the influence of the tip onto the molecule, we choose the molecule-tip distance to be large (5.57 Å in the Au and 5.89 Å in the Ag setup) compared to the distance between molecule and surface.

The relaxation of molecules on surfaces is generally a highly nontrivial task and, moreover, the molecular position strongly influences electrical, magnetic, and transport properties. Therefore, we use the optimized adsorption geometries from Huang *et al.* [44]. The resulting positions of the CuPc molecule on the Au(111) and Ag(111) surfaces are shown in Figs. 4.1(b) and 4.6, respectively. Importantly, the distance between the molecule and the relaxed surface layer of the Ag(111) surface is 2.84 Å which is larger than the distance obtained for CuPc on Ag(100) in Refs. [188, 192]. In Sec. 4.4.2 we discuss the influence of this discrepancy on the estimation of the Kondo temperature.

The DFT calculations are performed with SIESTA [84] and TranSIESTA [85] using the Perdew-Burke-Ernzerhof (PBE) [193] functional. We exclusively perform spin-unpolarized DFT calculations since we want to describe the magnetic properties using an additional strongly correlated many-body Hamiltonian. Calculation details are given in Appendix A.2.

4.3.2 Embedded many-body system

For the inclusion of many-body effects, we apply the method presented in Sec. 2.3.2 to construct an effective AIM. We obtain the bath parameters ϵ_{ik} and $\tilde{V}_{ik}$ of the AIM as presented in Sec. 2.3.3 and solve the impurity model using the FTPS solver presented in Sec. 2.3.4. As FTPS is a Hamiltonian based method, it can only employ a finite but large number of bath states and hence Eq. 2.3.20 can only be satisfied approximately. We perform the calculation using the following parameters. Our FTPS tensor network consists of 309 bath sites for each orbital. Note that we perform the calculations using the Hamiltonian of the AIM in the form given by Eq. 5.5.2, i.e., we do not transform onto a nearest-neighbor tight-binding Wilson chain [194, 195]. The truncation at each singular value decomposition (SVD) was 10^{-11} during density matrix renormalization group (DMRG) and $5 \cdot 10^{-9}$ during time evolution where we additionally restrict the maximal tensor index dimensions to 1500. We choose a Suzuki-Trotter time step $\Delta t = 0.5\text{eV}$ to be able to resolve the low-energy part of the spectrum better. This might seem very large, but remember that the energy scales of the Hamiltonian in general are very small ($U = 0.5$ eV see below) allowing a larger time step. Additionally, we checked that the result is converged in Δt. We performed the time evolution up to times $t = 800\ \text{eV}^{-1}$ and used a broadening of $\eta = 0.005$ eV during Fourier transform (see Eq. 2.3.29). Furthermore, we made sure that the spectral function of the FTPS solver is consistent with the continuous-time quantum Monte Carlo (CTQMC) result. When using CTQMC as presented in Sec. 2.3.4, it was difficult to reliably discern the splitting of the Kondo resonance from artifacts of the analytic continuation (AC) done using the maximum entropy method [56] with an alternative evidence approximation [196] and the preblur formalism [197]. For this reason, we propose Bayesian parametric analytic continuation (BPAC) as a new method for the AC of noisy imaginary-time Green's function data, as e.g. obtained by CTQMC, in Chpt. 5. Most strikingly, BPAC allows to infer whether the data support specific structures of the spectral function. We show the results for an AIM closely related to the AIM describing CuPc on Ag(111) in Sec. 5.5.

Solving the AIM by the FTPS solver leads to the corresponding Green's function $G_{\text{AI}}^{\text{FTPS}}(\omega)$ of the AIM with approximated bath. Since the number of bath states is large (309 for each orbital, see above), the Green's function with a finite number of bath sites is a very good approximation to the true Green's function of the AIM with the hybridization $\bar{\Delta}_{\text{AI}}(\omega)$. Therefore, we can use the Dyson equation to obtain the self energy of the true AIM:

$$\bar{\Sigma}_{\text{AI}}(\omega) = \left(\bar{G}_{\text{AI}}^{0}\right)^{-1}(\omega) - \left(G_{\text{AI}}^{\text{FTPS}}\right)^{-1}(\omega) \tag{4.3.1}$$

with

$$\bar{G}_{\text{AI}}^{0}(\omega) = \left(\omega + \text{i}0^{+} - \bar{H}_{\text{AI}} - \bar{\Delta}_{\text{AI}}(\omega)\right)^{-1} . \tag{4.3.2}$$

4.4 Results for CuPc on Au(111) and Ag(111)

In this section, we use the scheme described above to perform an *ab initio* calculation for the electronic transport properties of CuPc on Au(111) and Ag(111), respectively. In Sec. 4.4.1, we present the DFT results and combine them with experimental evidence and other theoretical studies to obtain the interaction parameters used for the AIM. After that, in Sec. 4.4.2, we present the solutions of the AIM and estimate the Kondo temperatures of these systems. The different contributions to the transmission are then calculated in Sec. 4.4.3.

4.4.1 Density of states and interaction parameters

In this section, we estimate the interaction parameters using a simplified many-body approach, namely cluster perturbation theory (CPT), see Sec. 2.1.5. CPT becomes exact for vanishing interaction strength. It is reliable enough for a rough estimation but it will not be able to describe the Kondo physics appropriately.

First, we investigate CuPc on Au(111). In Fig. 4.3(a) we depict the atomic-element resolved DOS obtained from the spin-unpolarized DFT-PBE calculation. The orbital directly located at the Fermi energy (partially filled) turns out to have approximately 50 % copper and 50 % nitrogen character. The contributions from the carbons and the metal surface are negligible. Therefore, we identify this orbital as the b_{1g} orbital localized in the Cu ion reported in literature, e.g., Ref. [42]. Localization and partial filling ($S = 1/2$ for pristine CuPc [198]) suggest that correlation effects are important for the b_{1g} orbital. We will model these correlations by adding a Hubbard-type interaction with strength $U_{b_{1g}}$. To determine its magnitude, we use UPS spectra obtained in Ref. [44]. They report the HOMO peak at -0.81 eV also seen in our DFT-PBE calculations but at slightly lower energy. Importantly, the UPS spectra show no additional peak down to -1.6 eV which implies for a Hubbard model at half filling an on-site interaction of $U_{b_{1g}} > 3.2$ eV. Additionally, DFT calculations using the HSE exchange-correlation functional (DFT-HSE) performed in Ref. [44] suggest $U_{b_{1g}} = 4.0$ eV, which we use in the following. We use the AMF double counting according to Eq. 2.3.19. As suggested by DFT-HSE calculations the Hubbard satellites are almost symmetric around the Fermi level, which we can achieve using $x = 0.85$. Note that this choice of x does not affect the filling of $n = 1$ as suggested by $S = 1/2$ of the pristine CuPc. Since $\bar{\Gamma}_{b_{1g}} \ll U_{b_{1g}}$, namely $\bar{\Gamma}_{b_{1g}} = \mathcal{O}(\text{meV})$, using CPT to solve the many-body problem is justified. The atomic-element resolved DOS thus obtained is shown in Fig. 4.3(c). The HOMO peak at around -0.9 eV, the spectral weight below -1.6 eV, and the absence of the b_{1g} peak at the Fermi level are in good agreement to the DFT-HSE calculations and the UPS spectra of Ref. [44].

In contrast, for CuPc on Ag(111) photoemission spectroscopy [43] and for CuPc on Ag(100) scanning tunneling microscopy [41] show a Kondo resonance directly at the Fermi level. Besides the HOMO peak at -1.23 eV, peaks at -1.74 eV and -2.16 eV and spectral weight below -2.6 eV appear in the UPS spectra obtained in Ref. [44]. While our DFT-PBE

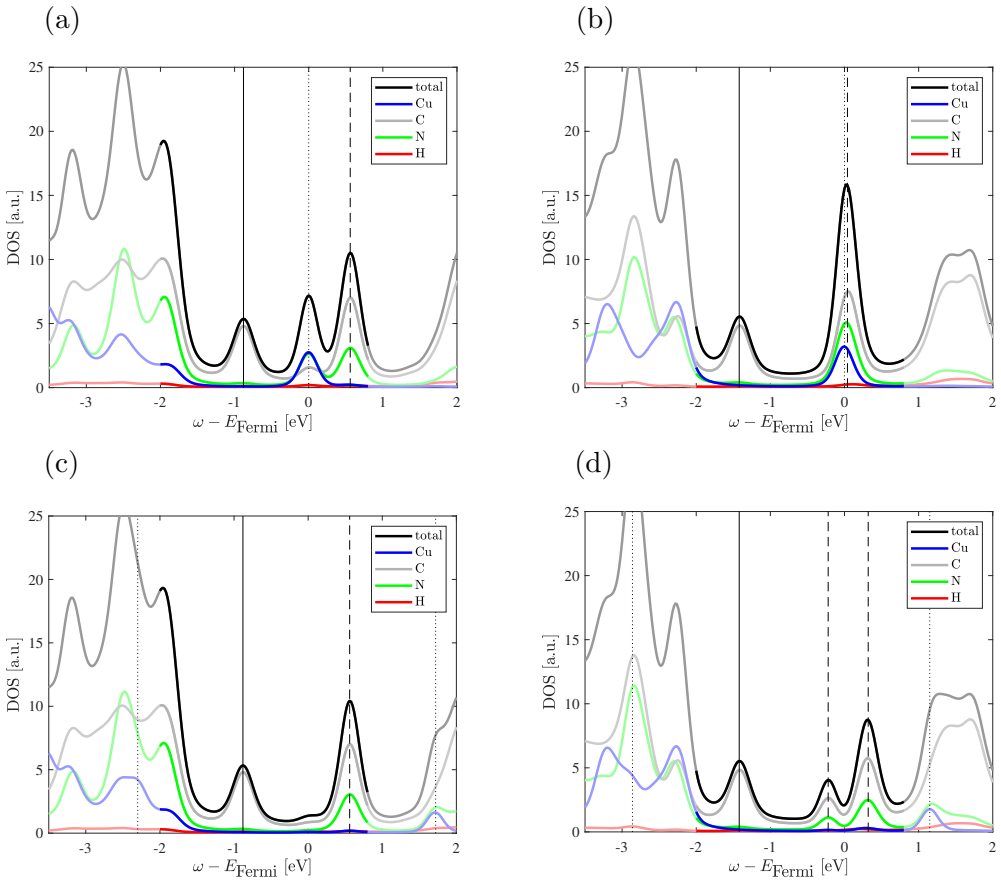

Figure 4.3: Atom-resolved DOS of CuPc on Au(111), (a) and (c), and Ag(111), (b) and (d). (a) and (b) are the ones obtained in DFT-PBE and (c) and (d) include the interaction term in the CPT approximation. We used a 0^+ of 0.04 for calculating the DOS and an additional convolution with a Gaussian to obtain a total broadening σ of $0.2/\sqrt{2}$. The vertical lines indicate the HOMO (solid line) and the positions of the $2e_g$ orbitals (dashed lines) and the b_{1g} orbitals (dotted lines).

calculation (Fig. 4.3(b)) shows the HOMO peak at approximately the correct position, other spectral weight can be found already below −2.0eV. Huang *et al.* [44] demonstrated that this is an artifact of the PBE exchange correlation functional. As can be seen in Fig. 6(b) of Ref. [44], the DFT spectral weight below −2 eV is shifted down to approximately −2.6 eV using HSE instead of PBE. The authors of Ref. [44] suggest that the remaining two peaks at −1.74 eV and −2.16 eV are closely related to the strong interaction between CuPc and Ag(111), especially the feature at −1.74 eV.

In our DFT-PBE calculation for CuPc on Ag(111), three orbitals are located at the Fermi energy and, therefore, partially filled. As in the case of CuPc on Au(111), we can identify one of them with the b_{1g} orbital. The remaining two orbitals are nearly degenerated and turn out to consist approximately of 50 % carbon and 30 % nitrogen character. Remaining contributions are from the copper ion and the metal surface. We identify them with the $2e_g$ levels spatially located mainly at the Pc. To model these three correlated orbitals, we choose the AIM Hamiltonian given by Eq. 2.3.17 with parameters

$$U = \begin{pmatrix} U_{b_{1g}} & U_{\mathrm{x}} & U_{\mathrm{x}} \\ U_{\mathrm{x}} & U_{2e_g} & U_{2e_g} \\ U_{\mathrm{x}} & U_{2e_g} & U_{2e_g} \end{pmatrix} \quad \text{and} \quad V = \begin{pmatrix} 0 & U_{\mathrm{x}} - J & U_{\mathrm{x}} - J \\ U_{\mathrm{x}} - J & 0 & U_{2e_g} \\ U_{\mathrm{x}} - J & U_{2e_g} & 0 \end{pmatrix}. \tag{4.4.1}$$

In analogy to CuPc on Au(111), we take $U_{b_{1g}} = 4.0$ eV as the on-site interaction parameter for the b_{1g} orbital. According to Refs. [188, 199], the screened interaction U for the $2e_g$ orbitals is between 0.5 eV and 1.0 eV on Ag surfaces. We choose $U_{2e_g} = 0.5$ eV, which is also in agreement with the results of DFT-HSE calculations performed in Ref. [44]. In analogy to CuPc on Au(111), we use a factor of $x = 0.85$ for the double counting (Eq. 2.3.19) in the b_{1g} orbital and $x = 1$ for the $2e_g$ system. In a first very crude approximation, we neglect correlations between the b_{1g} and the $2e_g$ orbitals, therefore $U_{\mathrm{x}} = J = 0$, and solve two independent many-body problems, one for the b_{1g} orbital and the other describing the $2e_g$ orbitals. In analogy to CuPc on Au(111), we used CPT for the many-body problem of the b_{1g} orbital. To obtain a first guess for the atomic-element resolved DOS depicted in 4.3(d), we also use the CPT approximation for the many-body problem of the $2e_g$ orbitals. Note that this approximation is not fully justified. Doing so, the DOS including the interaction is qualitatively comparable to the DFT calculations based on the HSE functional obtained in Ref. [44].

4.4.2 Kondo temperature and AIM

Now that all parameters are fixed, we will study the Kondo features and solve the many-body problem accurately by the FTPS solver introduced in Sec. 4.3.2. First, let us consider a possible Kondo effect in the b_{1g} orbitals of CuPc on Au(111) and Ag(111). For the one-band case in the wide-band limit (WBL), the Kondo temperature $T_{\mathrm{K,SU(2)}}$ is given by Eq. 2.4.15. We already determined the parameters $U_{b_{1g}} = 4$ eV and $\epsilon_{b_{1g}} = -2.29$ eV. In analogy to Eq. 2.1.63, the antihermitian part of the hybridization relevant for the Kondo effect is given

by

$$\bar{\Gamma}(\omega) = -2\Im\{\bar{\Delta}_{\mathrm{AI}}(\omega)\} \,. \tag{4.4.2}$$

Since Γ in Eq. 2.4.15 is in the WBL, and therefore independent of ω, we average $\bar{\Gamma}(\omega)$[1] in the interval $\omega \in [-1, 1]$,

$$\Gamma := \frac{1}{2}\int_{-1}^{1} d\omega\, \bar{\Gamma}(\omega) \,. \tag{4.4.3}$$

For CuPc on Au(111) $T_{\mathrm{K,SU(2)}} \lesssim 10^{-100}$ with $\Gamma_{b_{1g}} = 4.7$ meV, and therefore, Kondo features cannot be observed experimentally. The same is true for CuPc on Ag(111) ($\Gamma_{b_{1g}} = 9.4$ meV, $U_{b_{1g}} = 4$ eV, and $\epsilon_{b_{1g}} = -2.85$ eV). Hence, we do not expect to be able to observe Kondo resonances of the b_{1g} orbital in any of the two systems. Nevertheless, we will show below that the Kondo temperature for the $2e_g$ orbitals in CuPc on Ag(111) is high enough to be visible in experiments.

Therefore, let us discuss the many-body problem for CuPc on Ag(111) in more depth. First, we have to determine the missing parameters J and U_{x} introduced in Eq. 4.4.1. These parameters account for the exchange coupling between the b_{1g} and the $2e_g$ electrons and reproduce the Kondo side peaks obtained in Ref. [41]. According to the energy distance between side peaks and Kondo peak of about 21 meV we take $J = 25$ meV and $U_{\mathrm{x}} = J$. The DFT-PBE calculation leads to slightly different on-site energies ($\Delta\epsilon = 41$ meV) and hybridization functions for the $2e_g$ orbitals, see Fig. 4.4. This difference in the on-site energies $\Delta\epsilon$ causes a similar effect as the exchange coupling J, see Eq. 4.4.4 below. Therefore, from our *ab initio* calculations we cannot conclude whether the Kondo side peaks obtained in Ref. [41] stem from $\Delta\epsilon$ or J. Hence, we consider only the exchange coupling J and symmetrize the $2e_g$ orbitals ($\Delta\epsilon = 0$) and use the same hybridization function. We also neglect the off-diagonal contributions in the hybridization function since they are smaller by a factor of 5 (see Fig. 4.4) than the diagonal contributions. Furthermore, because of the strong localization of the b_{1g} orbital, we treat the correlations with the $2e_g$ orbitals in mean field and solve the AIM only in the $2e_g$ subspace using FTPS:

$$\begin{aligned} \hat{H}_{\mathrm{int},b_{1g}\text{-}e_g} &= J\hat{n}_{b_{1g},\uparrow}\hat{n}_{e_g,\downarrow} + J\hat{n}_{b_{1g},\downarrow}\hat{n}_{e_g,\uparrow} \\ &\approx J\underbrace{\langle\hat{n}_{b_{1g},\uparrow}\rangle}_{\approx 0}\hat{n}_{e_g,\downarrow} + J\underbrace{\langle\hat{n}_{b_{1g},\downarrow}\rangle}_{\approx 1}\hat{n}_{e_g,\uparrow} \approx J\hat{n}_{e_g,\uparrow} \end{aligned} \tag{4.4.4}$$

where we set $\langle\hat{n}_{b_{1g},\uparrow}\rangle = 0$ and $\langle\hat{n}_{b_{1g},\downarrow}\rangle = 1$. For the bath hybridization, we choose an energy window $[-1, 1]$, see Fig. 4.4, and represent this energy range using 309 bath sites for each orbital and spin. Such a large bath is necessary to be able to resolve the fine details of the splitting of the Kondo resonance. The spectral function for the AI orbitals obtained by FTPS is shown in Fig. 4.5. The spectral function for $J = 0$ (gray line) shows the familiar scenario consisting of two Hubbard satellites and the Kondo resonance at 0 eV. An exchange

[1] This procedure seems crude, but consider that due to the uncertainty in the DFT part and the interaction parameters, we are providing only a rough estimate of T_{K}.

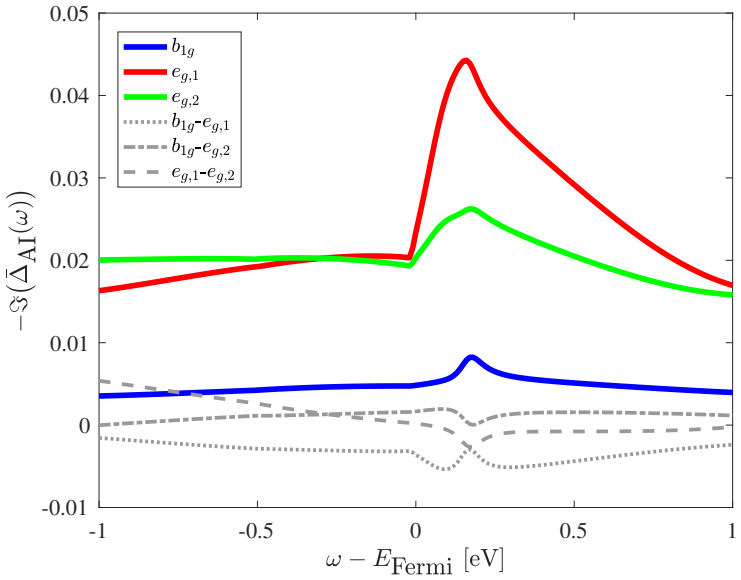

Figure 4.4: Matrix elements of the imaginary part of the hybridization $\bar{\Delta}_{\mathrm{AI}}$ for CuPc on Ag(111).

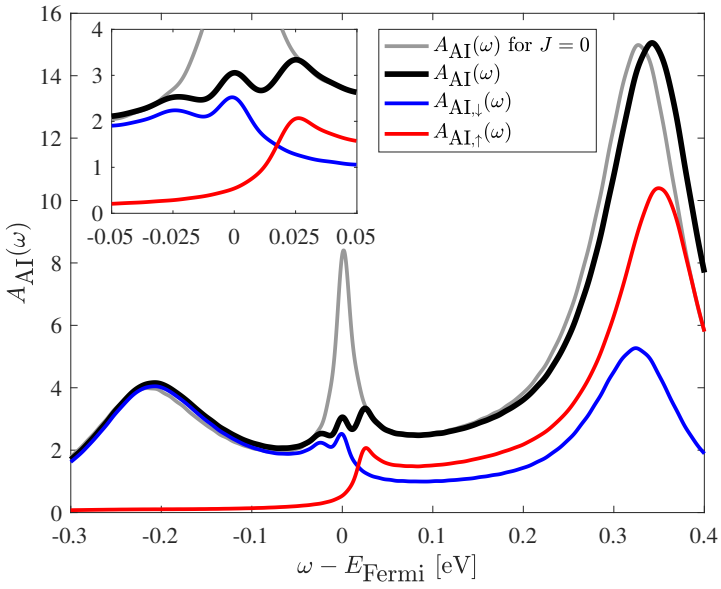

Figure 4.5: Spectral function of the AIM of CuPc on Ag(111) for $J = 0$ (gray line) and $J = 25$ meV (black line) separated in spin down (blue line) and spin up (red line).

coupling of $J = 25$ meV breaks the spin degeneracy by increasing the on-site energy for spin-up electrons according to Eq. 4.4.4 but not the orbital degeneracy. Hence, $A_{\mathrm{AI}\downarrow}(\omega)$ (blue line) differs from $A_{\mathrm{AI}\uparrow}(\omega)$ (red line). Since mainly $A_{\mathrm{AI}\downarrow}(\omega)$ is occupied, the degeneracy of the $2e_g$ orbitals causes an orbital Kondo effect in the spin-down electrons producing the Kondo resonance at 0 eV. The spin Kondo effect leads to the Kondo satellite peaks at $\omega \approx \pm 25$ meV in the total spectral function (black line). Note that $\Delta\epsilon = 25$ meV and $J = 0$ would show the same Kondo scenario but orbital and spin degrees of freedom are interchanged.

Let us discuss the impact of the symmetry reduction on the Kondo temperature. In the limit of $J \to 0$, the spins of the $2e_g$ orbitals are degenerate causing an SU(4) Kondo effect. For $J \to \infty$ on the other hand, the two spin-up orbitals are shifted to $+\infty$ and we expect an SU(2) (orbital) Kondo effect from the remaining spin-down degrees of freedom (see Eq. 4.4.4). For intermediate values of J, we hence expect a situation in between the SU(4) and the SU(2) Kondo regime as discussed in Refs. [136, 137]. The comparison of the relevant energy scales shows that the exchange coupling J is larger than both Kondo temperatures (SU(2) and SU(4)). This indicates that the system is closer to the SU(2) than to the SU(4) regime and, therefore, for the Kondo temperature of CuPc on Ag(111) $T_{\mathrm{K,SU(2)}}$ is the better approximation. The relevant parameters for estimating the Kondo temperature are $U_{2e_g} = 0.5$ eV, $\Gamma_{2e_g} = 44.2$ meV, which is the mean of $\Gamma_{e_g,1}$ and $\Gamma_{e_g,2}$, and $\epsilon_{2e_g} = -0.20$ eV, being the mean of $\epsilon_{e_g,1}$ and $\epsilon_{e_g,2}$. Equation 2.4.15 yields $T_{\mathrm{K,SU(2)}} = \{0.02, 1.5, 39\}$ K where the values are the $\{25, 50, 75\}$ %-quantile. The quantiles are determined by assuming a Gaussian distribution for Γ, U, and ϵ_0 centered at the value obtained in the previous section and with a standard deviation which is 50 % of the modulus of that value.[2] We emphasize that the Kondo temperature depends sensitively (exponentially) on the relevant parameters and therefore getting the correct order of magnitude for T_{K} is already a remarkable result. A closed analytical expression for the Kondo temperature of the SU(4) symmetrical Anderson model is given in Eq. 2.4.16 according to Ref. [139]. Application of this formula yields $T_{\mathrm{K,SU(4)}} = \{3, 25, 84\}$ K. Both temperatures, $T_{\mathrm{K,SU(2)}}$ and $T_{\mathrm{K,SU(4)}}$, are consistent with the experimentally obtained Kondo temperature for CuPc on Ag(100) of $T_{\mathrm{K}} = 27$ K [41].

To be able to obtain values for the Kondo temperature comparable to experiment, Korytár *et al.* [188] rescaled ϵ and Γ. The hybridization Γ_{2e_g} obtained in our calculation is smaller than Γ obtained for CuPc on Ag(100) in Ref. [188] and therefore gives a different estimate of the Kondo temperature. Hence, we suggest an imprecise adsorption geometry as possible origin of the necessity of this rescaling procedure. As shown in our calculation it is possible to get at least the correct order of magnitude for the Kondo temperature from *ab initio* calculations.

4.4.3 Transport properties

As discussed in Sec. 4.4.1, the $2e_g$ orbitals contain 50 % contribution from the carbon atoms and 30 % from the nitrogen atoms while the remaining contributions are from the copper ion

[2] This magnitude of the error accounts for uncertainties due to approximations in DFT and the estimation of the interaction parameters.

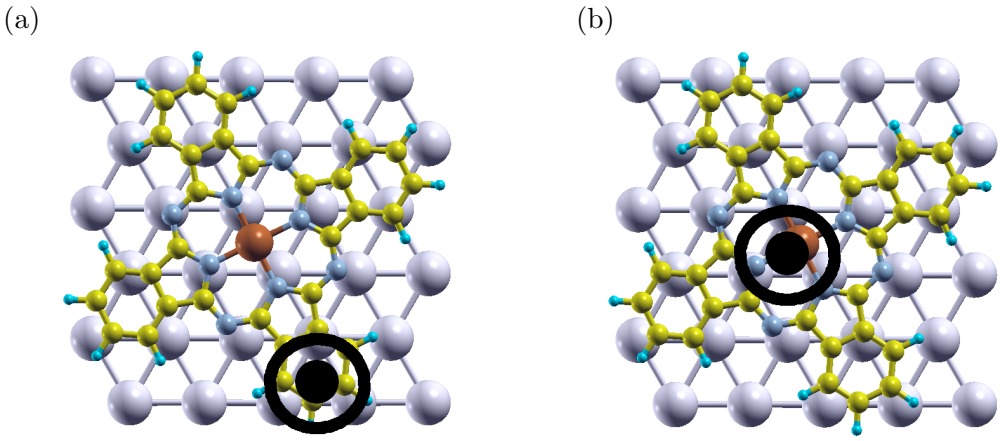

Figure 4.6: The tip positions I (a) and II (b) of the STM tip (black sphere) on the molecule on the Ag(111) surface. The pictures are drawn with XCrySDen [148].

and the metal surface. Whether a Kondo feature can be observed in the differential conductance measurements with an STM therefore depends on the position of the tip. In particular, if the tip is placed above the benzene rings, we expect to observe a Kondo resonance, which should be absent if the tip is above the Cu atom (see Fig. 4.6). Therefore, let us discuss the transport properties for the two tip positions used in the experiment performed in Refs. [41, 42] (also shown in Fig. 4.6).

Figures 4.7 and 4.9 show the calculated transmissions for the two STM tip positions. In addition to the total transmission, we also show its different contributions, as derived in Sec. 2.3.5: The coherent part T_{coh}, consisting of T_{NI}, T_{AI}, and T_{I}, as well as the incoherent part $T_{\mathrm{L,inc}}$. Beside the use of a different surface orientation, another difficulty in the comparison with the published experimental results in Ref. [41] is that the authors performed a background subtraction for the STM differential conductance measurements as proposed in Ref. [200]. The authors introduced the background subtraction to obtain the transmission of the molecule only, without effects stemming from the tip or the surface. To take the background subtraction into account in our calculations, we introduce a WBL approximation. Therefore we define the molecular region (MR $\subseteq$ IR) consisting of all atomic orbitals located at the CuPc molecule. Using a modified hybridization $\Gamma^{\mathrm{x,WBL}}_{\mathrm{MR}}$ for $x \in \{L, R\}$ leads to the following transmission formula:

$$T_{\mathrm{WBL}}(\omega) = \mathrm{Tr}\left[\Gamma^{\mathrm{L,WBL}}_{\mathrm{MR}} G^{\mathrm{WBL}}_{\mathrm{MR}}(\omega) \Gamma^{\mathrm{R,WBL}}_{\mathrm{MR}} G^{\mathrm{WBL}\dagger}_{\mathrm{MR}}(\omega)\right] \tag{4.4.5}$$

where direct tunneling from the surface to the tip is neglected. In the WBL approximation, we replace the imaginary parts of the hybridization functions by the constant

$$\Gamma^{x,\mathrm{WBL}}_{\mathrm{MR}} = \int_{-1/2}^{1/2} d\omega \; \Gamma^{x}_{\mathrm{MR}}(\omega) \; . \tag{4.4.6}$$

To obtain the corresponding real parts, we use the Kramers-Kronig relations. The Green's

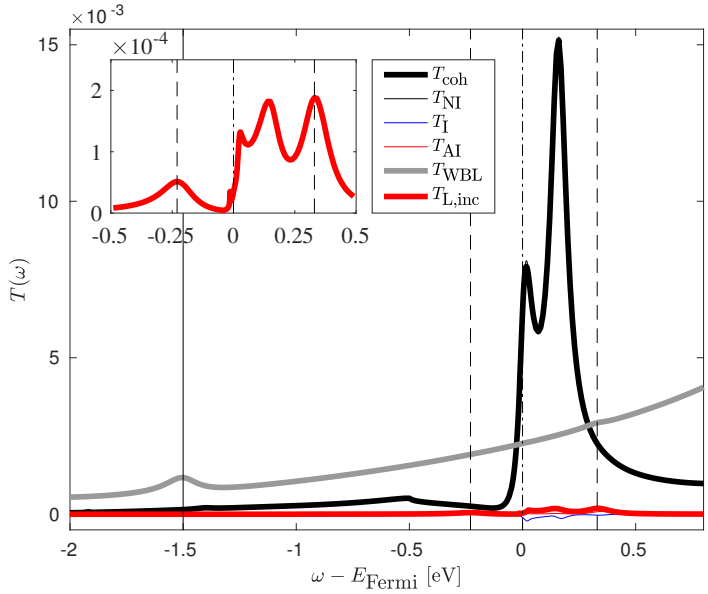

Figure 4.7: Transmission of CuPc on Ag(111) in tip position I. The vertical lines mark the position of the HOMO resonance (solid line), the Kondo resonance at 0 eV (dash-dotted line), and the positions of the Hubbard satellites (dashed lines).

function

$$G_{\mathrm{MR}}^{\mathrm{WBL}}(\omega) = \left(\left(\omega + \mathrm{i}0^{+}\right) S_{\mathrm{MR}} - H_{\mathrm{MR}} - \Delta_{\mathrm{L,MR}}^{\mathrm{WBL}}(\omega) - \Delta_{\mathrm{R,MR}}^{\mathrm{WBL}}(\omega) - \Sigma_{\mathrm{MR}}(\omega) \right)^{-1} \tag{4.4.7}$$

includes only the MR part of the self-energy.

Figure 4.7 shows the resulting transmission calculated for tip position I, obtained from the *ab initio* calculation, as well as in the WBL. First of all, we observe in the *ab initio* case that the largest contribution to the coherent transmission T_{coh} (black line) is from T_{NI} (thin black line, mostly covered by the black line). It has only small contributions from T_{AI} (thin red line, covered by the red line) and T_{I} (thin blue line). Moreover, the coherent transmission T_{coh} is dominated by two peaks at energies 0.02 eV and 0.16 eV, respectively. These peaks are missing in the WBL (gray line) indicating that they cannot be attributed to the pristine molecule. To underpin this interpretation, we present in Fig. 4.8 the projected DOS of the surface (dash-dotted line) and the tip (dashed line). We observe that the projected DOS of the surface layer and tip show peaks at 0.02 eV and 0.16 eV, respectively, coinciding with the peaks in the coherent transmission (black line). Additional six-layer slab calculations (gray line) of the pristine Ag(111) surface with a vacuum gap of 10 Å and an appropriate number of k points show that these peaks in the DOS are an artifact of the finite p(6×5) surface Γ point calculation. To avoid these artifacts, we would have to increase the number of atoms in the super cell which is computationally very demanding and would most likely not provide additional information.

In Fig. 4.7, the transmission in the WBL T_{WBL} is much smoother and clearly shows the

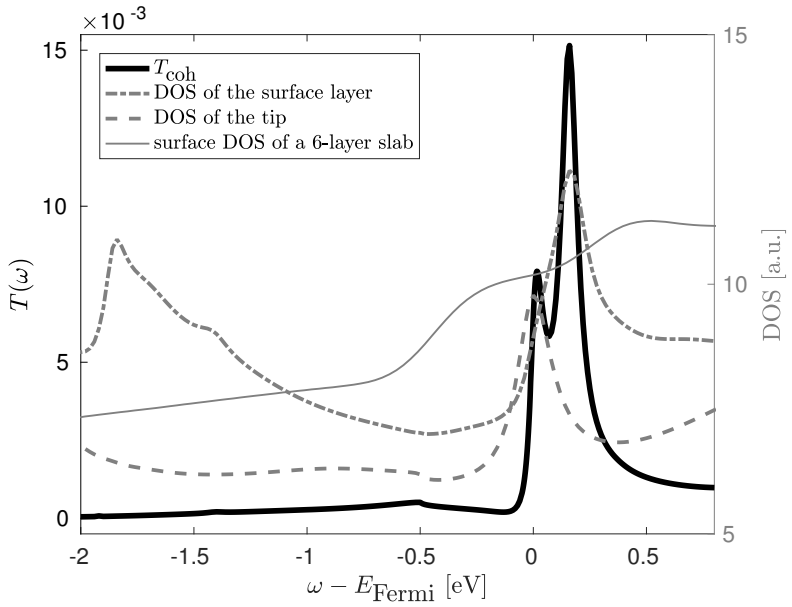

Figure 4.8: Coherent transmission of the STM configuration in tip position I (left axis) and the DOS projected onto the atomic orbitals of the tip and the surface layer and the surface DOS of a 6-layer slab calculation (right axis).

HOMO peak, marked by a vertical line at about $-1.5eV$, which is in agreement with the experiments in Refs. [41, 42]. The incoherent part of the transmission for position I of the tip is shown in Fig. 4.7 as a red line (see also the inset). Apart from the two peaks induced by the surface and the tip, we find Hubbard satellites (dashed vertical lines) and the Kondo feature (dash-dotted vertical line). The positions of these peaks are also in agreement with the experiment.

Finally, in Fig. 4.9, we present the results obtained for tip position II. We find that the overall transmission is larger by one order of magnitude. The coherent transmission T_{coh} (black line) has contributions from T_{NI} (thin black line, mostly covered by the black line), from T_{AI} (thin red line), and from the interference part T_{I} (thin blue line). T_{NI} consists mainly of the surface and the tip features discussed above and T_{AI} consists of the Hubbard satellites, again marked with dashed vertical lines. There is almost no structure in T_{WBL} (gray line). The incoherent transmission (red line) shows Hubbard satellites (dashed vertical lines) and the Kondo feature (dash-dotted vertical line). The Kondo resonance is small compared to the height of the Hubbard bands.

There are two big differences between the results for tip positions I and II. First, the HOMO peak at about $-1.5eV$ appears in tip position I and not in tip position II (compare gray lines in Figs. 4.7 and 4.9). Secondly, the Kondo resonance is very pronounced in tip position I, while at tip position II the height of the Hubbard satellites is much larger than the height of the Kondo resonance (compare red lines in Figs. 4.7 and 4.9). Both findings are in agreement with the experiment for CuPc on Ag(100) in Ref. [41].

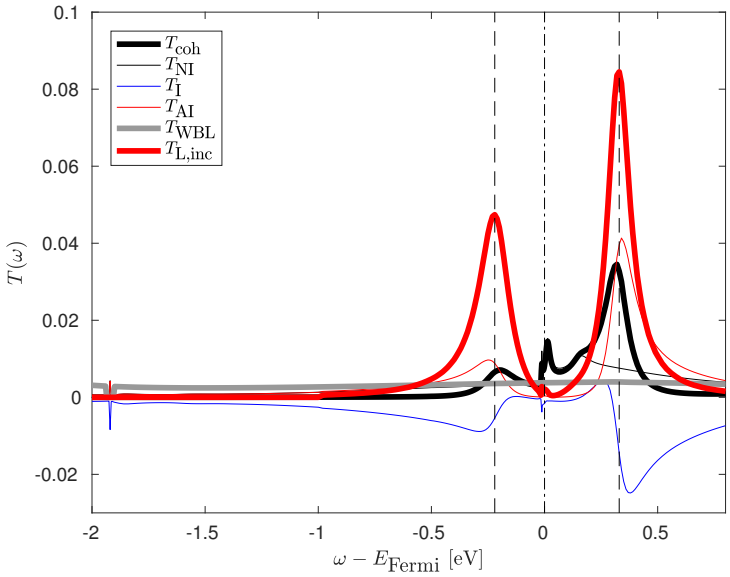

Figure 4.9: Transmission of CuPc on Ag(111) in tip position II. The vertical lines mark the Kondo resonance at 0 eV (dash-dotted line) and the positions of the Hubbard satellites (dashed lines).

4.5 Conclusions

We investigated equilibrium and transport properties of a CuPc molecule adsorbed on Au(111) and Ag(111). Apart from the usual coherent contributions to the transmission, several localized partially filled (strongly correlated) orbitals also lead to an incoherent part. As the starting point for our *ab initio* calculation we used the adsorption geometry obtained by Huang *et al.* [44] and performed DFT calculations that describe the coherent part of the transmission reasonably well. To tackle the strongly correlated part, we first used the transformation scheme described by Droghetti *et al.* [45] to obtain an AIM based on the DFT calculations. We estimate the interaction parameters from theoretical and experimental data published in Refs. [41, 44]. For CuPc on Au(111), there is one unpaired spin in the b_{1g} orbital located at the copper ion. Whereas for CuPc on Ag(111), there is an additional unpaired electron in two almost degenerated $2e_g$ orbitals. In both systems, the coupling between the b_{1g} orbital and the remaining system is weak, and therefore, the Kondo temperature for the b_{1g} orbital is very small. Hence, no Kondo resonance is found in experiments for CuPc on Au(111).

This is different for CuPc on Ag(111) where the AIM consists of three orbitals filled with two electrons, the b_{1g} orbital and the $2e_g$ orbitals. While the Kondo temperature of the b_{1g} is still very small, the electron in the $2e_g$ orbitals shows a measurable Kondo resonance. We solve the corresponding AIM obtained by the transformation scheme using CPT for the b_{1g} subspace and the FTPS solver for the $2e_g$ subspace. To combine the two subspaces, we treat the correlations between the subspaces on a mean-field level. The mean-field coupling reduces

the SU(4) symmetry of the $2e_g$ subspace into a SU(2) symmetry of the orbital degrees of freedom. This in turn leads to a Kondo effect with a symmetry somewhere between SU(2) and SU(4) for CuPc on Ag(111).

Since the Kondo temperature depends sensitively on the hybridization of the molecule with the surface, the adsorption geometry is very important in the DFT calculation. Indeed, using the relaxed geometries and taking additionally into account the error propagation of the incoming parameters yields reliable *ab initio* estimates of the Kondo temperature. In addition, we find that the transport properties depend on the detailed position of the STM tip above the CuPc molecule in qualitative agreement with the differential conductance measurements of Refs. [41, 42].

Chapter 5

Bayesian parametric analytic continuation

5.1 Introduction

In quantum transport simulations of strongly correlated molecules, solving the many-body problem requires special numerical approaches, e.g., exact diagonalization (ED), continuous-time quantum Monte Carlo (CTQMC), and fork tensor product states (FTPS), as discussed in Sec. 2.3.4. Quantum Monte Carlo methods calculate Green's functions in the imaginary-time domain. The imaginary-time Green's function $G(\tau)$ is related to the spectral function $A(\omega)$, and therefore, to the frequency-dependent Green's function $G(\omega)$, by a Laplace transform, the so-called analytic continuation (AC). Obtaining $A(\omega)$ from $G(\tau)$ corresponds to inverting a Fredholm integral of the first kind and small changes in $G(\tau)$ correspond to large differences in $A(\omega)$. The AC problem is *ill-posed* and very unstable against numerical noise; even errors at the level of machine precision can lead to unphysical results in practice.

In Sec. 4.4, we already presented the FTPS results of the Anderson impurity model (AIM) describing the many-body physics of CuPc on Ag(111). To compare, we solved the AIM by employing CTQMC and have thereby reached the limits of the existing methods for performing the AC. That is the reason why we put special emphasis on the AC of noisy imaginary-time CTQMC data in the present chapter. We discuss the FTPS and CTQMC solution for an AIM closely related to the AIM of CuPc on Ag(111) in detail in Sec. 5.5.

Many different methods to perform the AC have been proposed, e.g., series expansions such as the Padé method [201], machine learning [202], stochastic methods [203–209], and the maximum entropy method (MEM) [210–214]. The latter is a consistent approach as it is based on Bayesian probability theory; however, a highly ignorant entropic prior is used, which merely accounts for positivity and additivity of the reconstructed signal.

Here, we propose a physically motivated prior that takes into account the knowledge of typical structures of a spectral density, which results in a parametric instead of a form-free

reconstruction. The Bayesian parametric analytic continuation (BPAC) is based on Bayesian parameter estimation [49–52] to obtain a parametrized spectral function. To be precise, we use asymmetric Lorentzians as well as suitable tails to build up the spectral function. To validate parametrizations, we use Bayesian model comparison. The required evidence integrals can be computed by employing methods such as thermodynamic integration (TI) [53, 54] or nested sampling (NESA) [55]. With this approach, we can compare parametrizations, e.g., with a different number of asymmetric Lorentzians. Compared to the other methods, this allows to ask specific questions about the spectral function, e.g., about the reliability of peaks in the spectral function.

We demonstrate the capability of BPAC in terms of an AIM closely related to the AIM of CuPc on Ag(111). We calculate the imaginary-time Green's function of the AIM with CTQMC and compare the spectral functions obtained from BPAC with that of a MEM reconstruction. The MEM spectrum shows a peak close to the Abrikosov-Suhl resonance, but it is unclear whether this feature is physical or an artifact of the AC. BPAC can answer this question showing that it is, in fact, an artifact. Additionally, we successfully compare the BPAC result to the solution obtained with the recently developed real-time FTPS impurity solver which directly computes the spectral density without any AC.

In addition, we present a combination of MEM and BPAC and its application to an AIM arising from the dynamical mean-field theory (DMFT) [215, 216] treatment of $SrVO_3$. The spectral function obtained with the real-time FTPS solver shows a three-peak structure in the upper Hubbard band which is absent in the CTQMC+MEM spectral function. We investigate the question whether the absence of this structure is due to a failure of the MEM or due to the ill-posed nature of the AC.

The applications of BPAC presented in the present chapter demonstrate that BPAC is a valuable addition to nonparametric reconstruction methods such as MEM, e.g., to assess whether the data support specific features found in the MEM reconstruction.

Disregarding small changes which we made to preserve the structure of the thesis, this chapter is adopted from the article *Bayesian parametric analytic continuation of Green's functions* published in Phys. Rev. B **100** 075137, August 2019 [217]. This work is carried out by Michael Rumetshofer and Daniel Bauernfeind and is supervised by Wolfgang von der Linden. The basic principle for BPAC was developed by Michael Rumetshofer and Wolfgang von der Linden. Michael Rumetshofer carried out the entire simulations except for the FTPS calculations which have been done by Daniel Bauernfeind. All authors contributed to the discussions and conclusions.

The present chapter is organized as follows: We first introduce the AC problem in Sec. 5.2. In Sec. 5.3, we define and evaluate our parametrizations of the spectral function. Bayesian parameter estimation and model comparison are discussed in Sec. 5.4. Finally, in Secs. 5.5 and 5.6, we demonstrate the capability of BPAC, first, on an AIM closely related to the AIM of CuPc on Ag(111), and second, on an AIM stemming from the *ab initio* treatment of $SrVO_3$.

5.2 Analytic continuation and maximum entropy methods

Dynamical correlation functions in imaginary time as obtained from CTQMC obey the (anti-) periodicity relation $G(\tau+\beta) = \mp G(\tau)$. The upper sign (-) holds for fermions and the lower sign (+) holds for bosons. Due to (anti-) periodicity, $G(\tau)$ is uniquely determined by its values in the interval $\tau \in [0,\beta)$ and its discrete Fourier representation is

$$G(\tau) = \frac{1}{\beta}\sum_{\omega_n} e^{-\mathrm{i}\omega_n\tau}\mathcal{G}(\mathrm{i}\omega_n)\ . \tag{5.2.1}$$

The sum is over the Matsubara frequencies $\omega_n = (2n+1)\pi/\beta$ for fermions and $\omega_n = 2n\pi/\beta$ for bosons, where $n \in \mathbb{Z}$. The retarded Green's function $\mathcal{G}(\omega + \mathrm{i}0^+)$ and Matsubara Green's function $\mathcal{G}(\mathrm{i}\omega_n)$ are related through the analyticity of $\mathcal{G}(z)$. The spectral function $A(\omega) = -\frac{1}{\pi}\Im\mathcal{G}(\omega + i0^+)$ determines

$$\mathcal{G}(z) = \mp\int_{-\infty}^{\infty} d\omega\ \frac{A(\omega)}{z-\omega}\ . \tag{5.2.2}$$

Merging Eqs. 5.2.1 and 5.2.2 produces the relation between the imaginary-time Green's function $G(\tau)$ and the spectral function $A(\omega)$, e.g., for fermions,

$$G(\tau) = \int_{-\infty}^{\infty} d\omega\ \frac{e^{-\omega\tau}}{e^{-\beta\omega}+1}A(\omega) = \int_{-\infty}^{\infty} d\omega\ K(\tau,\omega)A(\omega)\ . \tag{5.2.3}$$

To handle the problem numerically, we discretize the functions $G(\tau)$ and $A(\omega)$, i.e., $(\mathbf{G})_n = G_n = G(\tau_n)$ and $(\mathbf{A})_m = A_m = A(\omega_m)$. Consequently, discretizing the kernel $K_{nm} = K(\tau_n,\omega_m)$ produces the matrix equation $\mathbf{G} = K\mathbf{A}$. Note that, as shown by Ref. [209], choosing the discretization grid already includes prior information and is equivalent to imposing a default model. Here, we restrict ourselves to linear discretization grids.

The determination of $\mathbf{G}$ from $\mathbf{A}$ is straight forward, but the inversion $\mathbf{A} = K^{-1}\mathbf{G}$ is an ill-posed problem which is impossible to tackle without taking the noise statistics and reliable prior knowledge consistently into account. In assuming a multivariate normal distribution with the covariance matrix Σ of the QMC data vector $\mathbf{G}_\mathrm{d}$, the maximum likelihood (ML) estimator $\mathbf{A}_\mathrm{ML}$ is obtained by minimization of $\chi^2(\mathbf{A}) = (K\mathbf{A}-\mathbf{G}_\mathrm{d})^T\Sigma^{-1}(K\mathbf{A}-\mathbf{G}_\mathrm{d})$. Due to the ill posedness of the problem, $\mathbf{A}_\mathrm{ML}$ is in general not a satisfying solution, e.g., negative, spiky, and unnormalized. Additional information, e.g., positivity, smoothness, etc., can be incorporated to regularize the problem. As shown by Skilling [218] on a rigorous probabilistic footing, introducing an entropy term

$$S(A) = \int_{-\infty}^{\infty} d\omega\ \left(A(\omega) - D(\omega) - A(\omega)\ln\frac{A(\omega)}{D(\omega)}\right) \tag{5.2.4}$$

and maximizing $-\frac{1}{2}\chi^2(\mathbf{A}) + \alpha S(\mathbf{A})$, where $S(\mathbf{A})$ is the discretized version of the entropy $S(A)$, regularizes the problem. In this so-called MEM, the standard model $D(\omega)$ determines the prior information about the spectral function, and the hyperparameter α, roughly speaking, determines the mixing ratio between the ML solution and the standard model $D(\omega)$. A small α produces the ML solution, whereas for large α, the spectral function approaches the standard model $D(\omega)$. The hyperparameter α can be adjusted in various ways, e.g., historic MEM [212, 219], classical MEM [220, 221], and Bryan MEM [222].

5.3 Parametrization of spectral functions

In the present chapter, we propose BPAC. This approach circumvents the ill-posed problem to a large extend by representing the spectrum using only a few parameters.

We want to build up the spectral function as a sum of peaks where each peak is supposed to correspond to a real peak in the spectrum, e.g., the Abrikosov-Suhl resonance, the left and right Hubbard band, etc. Due to the natural line width of spectral lines, the obvious choice is to use Lorentzian functions. General peaks in spectral functions are not single Lorentzians and can show shoulders or plateaus, e.g., between a Hubbard band and the Abrikosov-Suhl resonance. Therefore, we introduce a sum of asymmetric Lorentzian functions for each peak and add additional tails to describe the decay of the spectrum at higher energies. It depends on the desired accuracy $|A(\omega)-A_0(\omega)|$ of the reconstructed spectrum $A(\omega)$ to the true spectral function $A_0(\omega)$ whether using one or more Lorentzians per peak is more appropriate. In our parametrization, the nth peak is located at position μ_n and is built up by C_n asymmetric Lorentzians, each $i \in \{1, 2, ..., C_n\}$ having its own individual amplitude a_n^i, left width $\gamma_n^{i,\mathrm{l}}$, and right width $\gamma_n^{i,\mathrm{r}}$, resulting in $(3C_n + 1)$ parameters $\tilde{\alpha}_n = \{\mu_n, \{a_n^i, \gamma_n^{i,\mathrm{l}}, \gamma_n^{i,\mathrm{r}}\}\}$,

$$f_n(\omega|\tilde{\alpha}_n) = \begin{cases} \sum_{i=1}^{C_n} a_n^i \frac{2\gamma_n^{i,\mathrm{l}}}{\gamma_n^{i,\mathrm{l}}+\gamma_n^{i,\mathrm{r}}} L(\omega|\mu_n, \gamma_n^{i,\mathrm{l}}) & \text{for } \omega < \mu_n \\ \sum_{i=1}^{C_n} a_n^i \frac{2\gamma_n^{i,\mathrm{r}}}{\gamma_n^{i,\mathrm{l}}+\gamma_n^{i,\mathrm{r}}} L(\omega|\mu_n, \gamma_n^{i,\mathrm{r}}) & \text{for } \mu_n \leqslant \omega \end{cases} . \tag{5.3.1}$$

$L(\omega|\mu, \gamma)$ denotes the normalized Lorentzian with center μ and width γ,

$$L(\omega|\mu, \gamma) := \frac{1}{\pi} \frac{\gamma}{(\omega - \mu)^2 + \gamma^2} . \tag{5.3.2}$$

We refer to the case of $C_n > 1$ as *split* Lorentzian. The prefactors $2\gamma_n^{i,\mathrm{l}}(\gamma_n^{i,\mathrm{l}} + \gamma_n^{i,\mathrm{r}})^{-1}$ and $2\gamma_n^{i,\mathrm{r}}(\gamma_n^{i,\mathrm{l}} + \gamma_n^{i,\mathrm{r}})^{-1}$ in Eq. 5.3.1 ensure continuity and normalization of the asymmetric Lorentzians. The spectrum in the frequency interval $I_\Omega = [\Omega^{\mathrm{l}}, \Omega^{\mathrm{r}}]$ is described by a superposition of the Lorentzians $f_n(\omega|\tilde{\alpha}_n)$. For the tails of the spectrum outside the interval I_Ω, a power-law decay is more appropriate. Then, the total spectral function becomes

$$A(\omega|\boldsymbol{\alpha}) = \begin{cases} a^{\mathrm{l}} \, |\omega - \mu^{\mathrm{l}}|^{-\nu^{\mathrm{l}}} & \text{for } \omega < \Omega^{\mathrm{l}} \\ \sum_{n=1}^{N_{\mathrm{p}}} \, f_n(\omega|\tilde{\alpha}_n) & \text{for } \Omega^{\mathrm{l}} \leqslant \omega \leqslant \Omega^{\mathrm{r}} \\ a^{\mathrm{r}} \, |\omega - \mu^{\mathrm{r}}|^{-\nu^{\mathrm{r}}} & \text{for } \Omega^{\mathrm{r}} < \omega \end{cases} . \tag{5.3.3}$$

N_{p} is the total number of peaks and $\boldsymbol{\alpha}$ includes the parameters of the Lorentzians $\tilde{\boldsymbol{\alpha}}$ and the six parameters of the tails, namely, $\{\mu^{\mathrm{l}}, \nu^{\mathrm{l}}, \Omega^{\mathrm{l}}, \mu^{\mathrm{r}}, \nu^{\mathrm{r}}, \Omega^{\mathrm{r}}\}$. The parameters a^{l} and a^{r} are determined by forcing the spectral function to be continuous. Hence, we end up with a spectral function described by $N_\alpha = \left(\sum_n^{N_{\mathrm{p}}}(3C_n + 1)\right) + 6$ parameters.

In a first test, we analyze how well parametrized spectral functions using Lorentzians of increasing complexity as defined in Eq. 5.3.3 can represent typical physical spectra. As a test case, we use the spin-down and spin-up spectra $A(\omega)$ of the AIM discussed in Sec. 5.5.

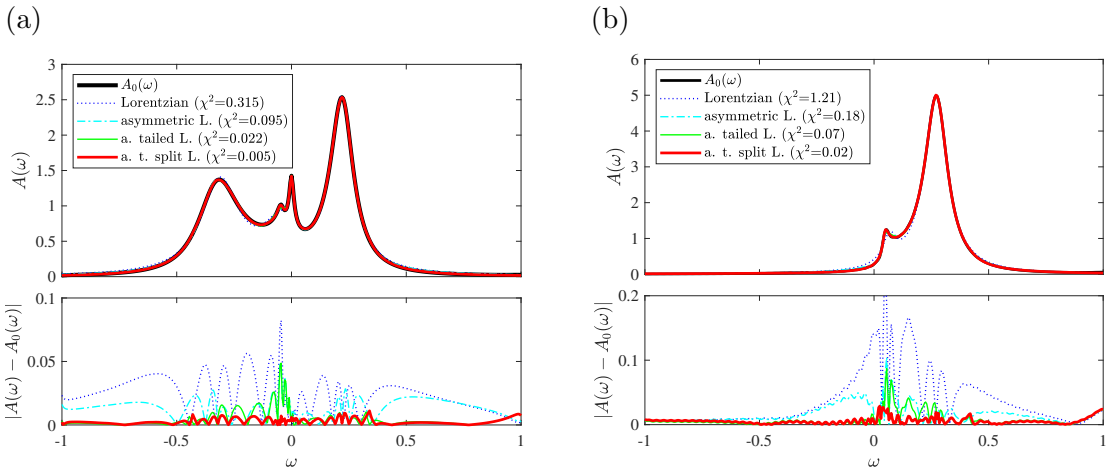

Figure 5.1: (a) Spin-down and (b) spin-up spectral function $A_0(\omega)$ of the AIM presented in Sec. 5.5 and obtained with the FTPS impurity solver. The upper plots show fits using Lorentzians (labeled: Lorentzian), asymmetric Lorentzians (labeled: asymmetric L.), asymmetric Lorentzians including tails (labeled: a. tailed L.), and asymmetric and split Lorentzians ($C_n = 2$, $\forall n$) including tails (labeled: a. t. split L.). We refer to the main text for the detailed definition of the parametrized spectral functions. The quadratic errors χ^2 and the deviation $|A(\omega) - A_0(\omega)|$ (lower plots) indicate the increasing quality of the fit.

Fig. 5.1 shows the (reference) spectra obtained by the FTPS impurity solver ($A_0(\omega)$, solid black lines) for the (a) spin-down and the (b) spin-up electrons and compares $A_0(\omega)$ to approximations of increasing complexity with the generalized Lorentzian ansatz (colored lines). For the (a) spin-down spectrum, we used a four-peak ($N_\mathrm{p} = 4$) spectral function whereas the (b) spin-up spectrum is approximated by a two-peak ($N_\mathrm{p} = 2$) spectral function. We determine the parameters in Eq. 5.3.3 by the least-squares approach. We find that using asymmetric Lorentzians instead of symmetric ones allows to describe the peaks much better, whereas including tails leads to visible improvements in the high-energy regions, see the lower plots in Figs. 5.1(a) and (b). Using split Lorentzians further decreases the deviation to the reference spectrum. Note that the small oscillations in the lower plots of Figs. 5.1(a) and (b) are artifacts caused by the Fourier transformation of the finite-time solution of the FTPS impurity solver.

To summarize, we find that the parametrization of Eq. 5.3.3 is highly flexible and allows to represent reliably the entire structure of the spectrum.

5.4 Parameter estimation and model comparison

5.4.1 Bayesian data analysis

In this section, we discuss how to determine the parameters $\boldsymbol{\alpha}$ of the spectral function $\mathbf{A}(\boldsymbol{\alpha})$ and how to judge which parametrization is supported best by the data. From now on, we

call a parametrization of the spectral function the model $M = M(\mathbf{C})$, depending implicitly on the peak complexity $\mathbf{C}$ which also includes the number of peaks $N_\mathrm{p} = \dim(\mathbf{C})$. Note that M does not define the values of the model parameters. Bayes' theorem gives

$$\underbrace{p(\boldsymbol{\alpha}|\mathbf{G}_\mathrm{d}, \boldsymbol{\sigma}, M, \mathcal{I})}_{\text{posterior}} \underbrace{p(\mathbf{G}_\mathrm{d}|M, \boldsymbol{\sigma}, \mathcal{I})}_{\text{data evidence}} = \underbrace{p(\mathbf{G}_\mathrm{d}|\boldsymbol{\alpha}, \boldsymbol{\sigma}, M, \mathcal{I})}_{\text{likelihood}} \underbrace{p(\boldsymbol{\alpha}|M, \mathcal{I})}_{\text{prior}} \tag{5.4.1}$$

where $\mathbf{G}_\mathrm{d}$ stands for the N_d imaginary-time data points from CTQMC. We assume that they have a multivariate Gaussian stochastic error. The corresponding covariance matrix is denoted by Σ. The kernel K is included in the conditional complex $\mathcal{I}$. The likelihood is therefore

$$\begin{aligned} L(\boldsymbol{\alpha}) :&= p(\mathbf{G}_\mathrm{d}|\boldsymbol{\alpha}, \boldsymbol{\sigma}, M, \mathcal{I}) = \frac{1}{\sqrt{(2\pi)^{N_\mathrm{d}} \det(\Sigma)}} e^{-\frac{1}{2}\chi^2(\boldsymbol{\alpha})} \\ \chi^2(\boldsymbol{\alpha}) &= (K\mathbf{A}(\boldsymbol{\alpha}) - \mathbf{G}_\mathrm{d})^T \Sigma^{-1} (K\mathbf{A}(\boldsymbol{\alpha}) - \mathbf{G}_\mathrm{d}) \ . \end{aligned} \tag{5.4.2}$$

Since correlations are negligible in the data sets used in the present chapter, we take $\Sigma_{ij} = \sigma_i^2 \delta_{ij}$ in the following.

We use the prior probability to restrict the parameter space for two reasons: First, to only obtain physical results, e.g., by forcing the spectral function to be positive ($a_n^i > 0$, $\forall n, i$); second, to build in and test additional knowledge about the spectral function, e.g., by forcing a peak to appear in a chosen energy interval to analyze whether the data support this peak. For example, a question that can be answered by BPAC could be: *Is there a side peak left to the Abrikosov-Suhl resonance?* Bayesian model comparison allows to judge whether the model including the additional peak is more probable than the model without this peak. Apart from the above restrictions, we used a flat prior,

$$\pi(\boldsymbol{\alpha}) := p(\boldsymbol{\alpha}|M, \mathcal{I}) = \prod_{i=1}^{N_\alpha} \frac{1}{\alpha_i^\mathrm{max} - \alpha_i^\mathrm{min}} \Theta(\alpha_i^\mathrm{min} < \alpha_i < \alpha_i^\mathrm{max}) \ . \tag{5.4.3}$$

In the present chapter, we restrict ourselves to this prior, which is simple to implement and computationally inexpensive since sampling from uniform distributions is cheap. More advanced priors are possible although, e.g., including transformation invariance, smoothness, using testable information, such as the normalization of the spectral function, or even using the entropic prior, may help to improve the results.

Primarily, we are interested in the probability density for the spectral function $p(\mathbf{A}|\mathbf{G}_\mathrm{d}, \boldsymbol{\sigma}, M, \mathcal{I})$ which we easily obtain from the posterior distribution $p(\boldsymbol{\alpha}|\mathbf{G}_\mathrm{d}, \boldsymbol{\sigma}, M, \mathcal{I})$ by using the marginalization rule,

$$p(\mathbf{A}|\mathbf{G}_\mathrm{d}, \boldsymbol{\sigma}, M, \mathcal{I}) = \int d\boldsymbol{\alpha} \ \underbrace{p(\mathbf{A}|\boldsymbol{\alpha}, M, \mathcal{I})}_{\delta(\mathbf{A}-\mathbf{A}(\boldsymbol{\alpha}))} p(\boldsymbol{\alpha}|\mathbf{G}_\mathrm{d}, \boldsymbol{\sigma}, M, \mathcal{I}) \ . \tag{5.4.4}$$

The integration over $\boldsymbol{\alpha}$ means integrating out each parameter included in $\boldsymbol{\alpha}$. The domain of each integration parameter, and therefore, the integration region, should be clear from the context. We keep this abbreviated notation during the whole chapter.

Additionally, we want to calculate the data evidence $p(\mathbf{G}_\mathrm{d}|M,\boldsymbol{\sigma},\mathcal{I})$ which allows to assess the probability of different models relative to each other since the probability for model M is proportional to the data evidence,

$$P(M|\mathbf{G}_\mathrm{d},\boldsymbol{\sigma},\mathcal{I}) = \frac{1}{p(\mathbf{G}_\mathrm{d}|\mathcal{I})}\, p(\mathbf{G}_\mathrm{d}|M,\boldsymbol{\sigma},\mathcal{I})\, P(M|\mathcal{I})\,. \tag{5.4.5}$$

In the so-called odds ratio, the ratio between the probabilities for models M_1 and M_2, the unknown probability $p(\mathbf{G}_\mathrm{d}|\mathcal{I})$ cancels out and we get

$$\mathcal{O} = \frac{P(M_1|\mathbf{G}_\mathrm{d},\boldsymbol{\sigma},\mathcal{I})}{P(M_2|\mathbf{G}_\mathrm{d},\boldsymbol{\sigma},\mathcal{I})} = \underbrace{\frac{p(\mathbf{G}_\mathrm{d}|M_1,\boldsymbol{\sigma},\mathcal{I})}{p(\mathbf{G}_\mathrm{d}|M_2,\boldsymbol{\sigma},\mathcal{I})}}_{\text{Bayes factor}} \underbrace{\frac{P(M_1|\mathcal{I})}{P(M_2|\mathcal{I})}}_{\text{prior odds}}\,. \tag{5.4.6}$$

In the applications presented in this chapter, we always set the prior odds to one since we do not want to favor any model.

5.4.2 Evaluating posterior and data evidence

In this section, we want to give a very brief introduction to NESA, which is a method providing both the data evidence and samples from the posterior. We provide the basic equations in this section but refer to Refs. [49, 52, 223] for the detailed derivation of NESA.

Skilling [55] proposed to write the data evidence integral as the Lebesgue integral

$$p(\mathbf{G}_\mathrm{d}|M,\boldsymbol{\sigma},\mathcal{I}) = \int d\boldsymbol{\alpha}\; \underbrace{p(\mathbf{G}_\mathrm{d}|\boldsymbol{\alpha},\boldsymbol{\sigma},M,\mathcal{I})}_{L(\boldsymbol{\alpha})}\underbrace{p(\boldsymbol{\alpha}|M,\mathcal{I})}_{\pi(\boldsymbol{\alpha})} = \int d\lambda\; X(\lambda) \tag{5.4.7}$$

where the integral over the prior mass

$$X(\lambda) = \int d\boldsymbol{\alpha}\; \pi(\boldsymbol{\alpha})\; \Theta\left(L(\boldsymbol{\alpha}) > \lambda\right) \tag{5.4.8}$$

runs over the likelihood values λ. Equivalently, the data evidence can be written as

$$p(\mathbf{G}_\mathrm{d}|M,\boldsymbol{\sigma},\mathcal{I}) = \int_0^1 dX\; \mathcal{L}(X) \approx \sum_{n=0}^{\infty} \Delta X_n\; \mathcal{L}(X_n) \approx \sum_{n=0}^{n_\mathrm{max}} \Delta X_n\; \lambda_n^* \tag{5.4.9}$$

where the integral is approximated by the Riemann sum and $\Delta X_n = X_n - X_{n+1}$. The likelihood $\mathcal{L}(X)$ is a monotonically decreasing function of the prior mass and the computation is as complicated as the original evaluation of the data evidence. Skilling proposed a stochastic approach to sample $\mathcal{L}(X)$ based on order statistics providing the likelihood minima $\{\lambda_n^*\}$. The pseudo code is given in Algorithm 5.4.1.

Algorithm 5.4.1: NESA ALGORITHM$(\{\lambda_n^*\}, \{\boldsymbol{\alpha}_n^*\}, n_{\max})$

input parameters: $N_{\mathrm{w}}, \epsilon_\lambda$
initialize $\lambda_0^* = 0$, $n = 0$,
draw N_{w} configurations $\{\boldsymbol{\alpha}_i\}$ at random from $\pi(\boldsymbol{\alpha}|\lambda_0^*)$ (Eq. 5.4.10)
take the smallest likelihood value $\lambda^* = \min\{\lambda_i = L(\boldsymbol{\alpha}_i)\}$ and its configuration $\boldsymbol{\alpha}^*$
set $\lambda_{n=1}^* := \lambda^*$ and $\boldsymbol{\alpha}_{n=1}^* := \boldsymbol{\alpha}^*$
while $\left|\left(\lambda_{n+1}^* - \lambda_n^*\right)/\lambda_{n+1}^*\right| > \epsilon_\lambda$
do
- $n \leftarrow n + 1$
- replace configuration $\boldsymbol{\alpha}^*$ with a new configuration drawn from $\pi(\boldsymbol{\alpha}|\lambda_n^*)$
- determine the smallest likelihood $\lambda^* = \min\{\lambda_i = L(\boldsymbol{\alpha}_i)\}$ and its configuration $\boldsymbol{\alpha}^*$
- **set** $\lambda_{n+1}^* = \lambda^*$ and $\boldsymbol{\alpha}_{n+1}^* = \boldsymbol{\alpha}^*$

set $n = n_{\max}$
return $(\{\lambda_n^*\}, \{\boldsymbol{\alpha}_n^*\}, n_{\max})$

The nested sampling moves in configuration space ensure that even well-separated peaks of the likelihood function are sampled correctly. The crucial step for the NESA algorithm is to draw from the constrained prior probability

$$\pi(\boldsymbol{\alpha}|\lambda_n^*) = \frac{\pi(\boldsymbol{\alpha})}{X(\lambda_n^*)}\,\Theta(L(\boldsymbol{\alpha}) > \lambda_n^*)\,. \tag{5.4.10}$$

This probability density represents the normalized prior restricted to areas where $L(\boldsymbol{\alpha})$ exceeds the λ_n^* threshold. In the applications presented in this chapter, $\pi(\boldsymbol{\alpha})$ is constant within the prior constraints according to Eq. 5.4.3. Therefore, we need to draw samples from the uniform distribution constrained by both the likelihood and the prior. A simple way to draw a sample from Eq. 5.4.10 is to clone an existing configuration, which obviously fulfills all constraints, and perform an ordinary Markov chain Monte Carlo update obeying $\pi(\boldsymbol{\alpha}|\lambda_n^*)$. We implemented local updates in the parameters and monitored autocorrelations, which can become considerable depending on the problem.

The prior masses can be derived using order statistics as shown in detail in Ref. [49]. We can write the nth prior mass as $X_n = \prod_{\nu=1}^{n} \theta_\nu$, where the shrinking factors θ_ν are independent and identically distributed random variables and obey the first-order statistic of the uniform probability density function (PDF), the β distribution $p(\theta) = \theta^{N_{\mathrm{w}}-1}/N_{\mathrm{w}}$. Knowing the distribution of X_n and, therefore, of ΔX_n, allows to calculate the expectation value and variance of the Riemann sum in Eq. 5.4.9 given the set of likelihood minima $\{\lambda_n^*\}$ obtained from Algorithm 5.4.1.

Also posterior samples can be generated from a single NESA run by reusing the samples $\{\boldsymbol{\alpha}_n^*\}$ obtained from Algorithm 5.4.1. Eq. 5.4.9 shows that the nth NESA step contributes with weight $\Delta X_n \lambda_n^*$ to the Riemann sum for calculating the data evidence. Therefore, samples from the posterior PDF can be provided by choosing n with the corresponding $\boldsymbol{\alpha}_n^*$ according to its weight $p(n) \propto \Delta X_n \lambda_n^*$, e.g., by inversion sampling. With such posterior samples $\{\boldsymbol{\alpha}_\nu\}$, the expectation value of the spectral function can be obtained as $\langle \mathbf{A} \rangle = \frac{1}{N_\nu} \sum_{\nu=1}^{N_\nu} \mathbf{A}(\boldsymbol{\alpha}_\nu)$.

There are different improvements of NESA going beyond the algorithm we presented within this section which may increase the performance, e.g., updating more configurations at once [49, 52], using a parallel version of NESA [224], extending the update method in the prior sampling [225], or using the knowledge of the position of the minima obtained by optimization algorithms [226]. We successfully checked all our NESA results by employing TI which we briefly discuss in Appendix A.3.

5.5 Application I: BPAC

In this section, we apply BPAC to an impurity problem closely related the AIM describing the many-body physics of CuPc on Ag(111) studied in Sec. 4.4.2. In Sec. 5.5.1, we define the AIM which we solve subsequently using three different methods: FTPS, CTQMC+MEM, and CTQMC+BPAC. Technical details of these methods are given in Sec. 5.5.2, whereas the comparison of the results is given in Sec. 5.5.3.

5.5.1 The impurity problem

Although we have already introduced the Hamiltonian of the AIM in Sec. 2.3.3, we like to do this again in a slightly modified form to keep this chapter self-contained. The Hamiltonian of the isolated multi-orbital Anderson impurity with on-site energies $\epsilon_{i\sigma}$ and interaction parameters U_{ij} for electrons of different spin and V_{ij} for electrons of the same spin is

$$\hat{H}_{\mathrm{AI}} = \sum_{i\sigma} \epsilon_{i\sigma} \hat{n}_{i\sigma} + \frac{1}{2} \sum_{ij\sigma} U_{ij} \hat{n}_{i\sigma} \hat{n}_{j\bar{\sigma}} + \frac{1}{2} \sum_{i \neq j, \sigma} V_{ij} \hat{n}_{i\sigma} \hat{n}_{j\sigma} \, . \tag{5.5.1}$$

Here, $\hat{n}_{i\sigma} = \hat{a}^{\dagger}_{i\sigma} \hat{a}_{i\sigma}$ is the particle number operator for orbital $i \in \{1, 2\}$ and spin $\sigma \in \{\downarrow, \uparrow\}$ in the second quantization with creation (annihilation) operators $\hat{a}^{\dagger}_{i\sigma}$ ($\hat{a}_{i\sigma}$). In the AIM, the impurity is coupled to a bath of non-interacting fermions,

$$\hat{H}_{\mathrm{AIM}} = \hat{H}_{\mathrm{AI}} + \sum_{ik\sigma} \tilde{V}_{ik} \left(\hat{a}^{\dagger}_{i\sigma} \hat{c}_{ik\sigma} + h.c. \right) + \sum_{ik\sigma} \epsilon_{ik} \hat{n}_{ik\sigma} \, . \tag{5.5.2}$$

$\hat{c}^{\dagger}_{ik\sigma}$ ($\hat{c}_{ik\sigma}$) are the creation (annihilation) operators of the kth bath state of orbital i with spin σ. For the on-site energy of the impurity, we use $\epsilon_{i\downarrow} = \epsilon - J$ and $\epsilon_{i\uparrow} = \epsilon$ with $\epsilon = -0.25$ eV and $J = 50$ meV, and

$$U = \begin{pmatrix} \tilde{U} & \tilde{U} \\ \tilde{U} & \tilde{U} \end{pmatrix} \quad \text{and} \quad V = \begin{pmatrix} 0 & \tilde{U} \\ \tilde{U} & 0 \end{pmatrix} \tag{5.5.3}$$

with $\tilde{U} = 0.5$ eV. The bath parameters $\tilde{V}_{ik}$ and ϵ_{ik} are obtained from a flat bath hybridization function

$$\Delta_i(\omega) \stackrel{!}{=} \sum_k \frac{\tilde{V}^2_{ik}}{\omega + \mathrm{i}0^+ - \epsilon_{ik}} \tag{5.5.4}$$

defined by $-2\Im\left(\Delta_i(\omega)\right) = \Gamma\ \Theta(-1 < \omega < 1)$ with $\Gamma = 50$ meV. This set of parameters exhibits a generalized Kondo scenario with symmetry between SU(2) [133] and SU(4) [139] with the corresponding Kondo temperatures of $T_{\mathrm{SU(2)}} = 0.36$ K and $T_{\mathrm{SU(4)}} = 20$ K. Due to the difference in the on-site energies of the impurity orbitals, this AIM exhibits side peaks close to the Abrikosov-Suhl resonance. We present the spin-down and spin-up spectral functions of this AIM in Figs. 5.2 and 5.4.

5.5.2 Technical details of the methods

We solve the AIM in the imaginary-time domain using the CTQMC solver in hybridization expansion as implemented in the TRIQS library [117, 120, 227]. We performed 15 CTQMC runs at $\beta = 400\ (\mathrm{eV})^{-1}$ ($T = 29$ K), each on 20 node points and with 10^6 measurements. The difference in the impurity on-site energies J lifts the spin degeneracy but keeps the orbital degeneracy intact and, therefore, the 15 CTQMC runs give 30 independent samples. Based on these samples, we estimate reliable variances for the QMC data without having to bother about possible autocorrelations.

In the following, we do not distinguish orbitals anymore and just discuss the spectral functions depending on the spin. The AC in the present chapter is performed with MEM and BPAC. In both cases, we use $N_{\mathrm{d}} = 401$ data points on an equally spaced τ grid for $\tau \in [0, \beta]$ and the same amount of ω points equally spaced on the interval $\omega \in [-1, 1]$. We applied the MEM of Ref. [56] with an alternative evidence approximation [196] and the preblur formalism [197]. BPAC is applied as explained in Sec. 5.4 using a $N_{\mathrm{w}} = 1000$ walker and $\epsilon_\lambda = 10^{-5}$.

Additionally, we compare the results with those obtained by the real-time FTPS impurity solver, which does not need any AC, since it calculates the Green's function already on the real axis. In contrast to the CTQMC solver, the FTPS solver is a zero-temperature method, which has to be considered when comparing the results.

5.5.3 Comparison of the results

First, we employ the FTPS solver for the spin-down part of the AIM and show the corresponding spectrum in Fig. 5.2 (black line). As expected from the definition of the impurity model in Sec. 5.5.1, the spectral function shows Hubbard satellites at approximately -0.3 eV and 0.2 eV and the Abrikosov-Suhl resonance at the chemical potential (0 eV). Additionally, there is a peak at approximately -50 meV contributed by the exchange coupling parameter J. The CTQMC+MEM result (red dash-dotted line) shows a spurious peak at approximately 0.04 eV which does not appear in the FTPS solution. To find out whether this peak is supported by the CTQMC data or whether it is an artifact of the AC by MEM, we employ BPAC (blue line). First, we use a four-peak model $M_4 = M(\mathbf{C} = (1, 1, 1, 1))$ where each peak consists of a single asymmetric Lorentzian, i.e., with peak complexity $C_n = 1$. The NESA logarithmic data evidence yields $\ln(p(\mathbf{G}_{\mathrm{d}}|M_4, \boldsymbol{\sigma}, \mathcal{I})) = 2828.2 \pm 0.3$. Table A.1 in Appendix A.4 shows the prior ranges used and the parameters estimated. The four-peak

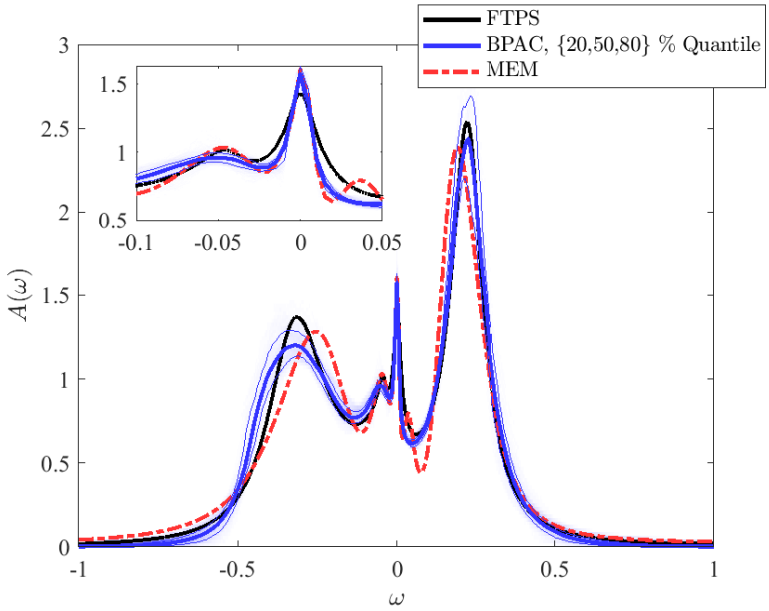

Figure 5.2: Spectral function for the down electrons obtained by the FTPS solver (black line), CTQMC+BPAC (blue line including confidence intervals), and CTQMC+MEM (red dash-dotted line). The BPAC solution does not show the peak slightly above $\omega = 0$ of the MEM solution, which is in agreement with the FTPS solution (the inset).

BPAC solution (Fig. 5.2, blue line) does not show the additional peak slightly above $\omega = 0$ by construction. The evaluation of the five-peak model $M_5 = M(\mathbf{C} = (1,1,1,1,1))$ where we introduce an additional peak at $\mu \in (0.03, 0.07)$ produces the logarithmic data evidence $\ln(p(\mathbf{G}_\mathrm{d}|M_5, \boldsymbol{\sigma}, \mathcal{I})) = 2825.0 \pm 0.3$. This yields a logarithmic Bayes factor of 3.2 ± 0.6 which corresponds to a probability of $(93\% - 98\%)$ that the four-peak model is preferred over the five-peak model. This is in agreement with the FTPS solution and demonstrates that the fifth peak at approximately 0.04 eV is not supported by the CTQMC data and, therefore, an artifact of the MEM solution. In general, the spectral function obtained by BPAC depends on the choice of the model M. In the spirit of Bayesian probability theory, we can average over different models weighted by their corresponding model probability. Therefore, we actually should compute

$$p(\mathbf{A}|\mathbf{G}_\mathrm{d}, \boldsymbol{\sigma}, \mathcal{I}) = \sum_i p(\mathbf{A}|\mathbf{G}_\mathrm{d}, \boldsymbol{\sigma}, M_i, \mathcal{I}) P(M_i|\mathbf{G}_\mathrm{d}, \boldsymbol{\sigma}, \mathcal{I}) \; . \tag{5.5.5}$$

If one model is highly preferable, as M_4 in the present case, then

$$p(\mathbf{A}|\mathbf{G}_\mathrm{d}, \boldsymbol{\sigma}, \mathcal{I}) \approx p(\mathbf{A}|\mathbf{G}_\mathrm{d}, \boldsymbol{\sigma}, M_4, \mathcal{I}) \; . \tag{5.5.6}$$

Hence, we plotted $p(\mathbf{A}|\mathbf{G}_\mathrm{d}, \boldsymbol{\sigma}, M_4, \mathcal{I})$ in Fig. 5.2 (blue line).

Starting point for the determination of the spectral function $A(\omega)$ are CTQMC data on the imaginary-time Green's function $G(\tau)$, which we denote by $G_\mathrm{d}(\tau)$. Inserting the reconstructed spectral function $A(\omega)$ into Eq. 5.2.3 yields the reconstructed $G(\tau)$, which allows to

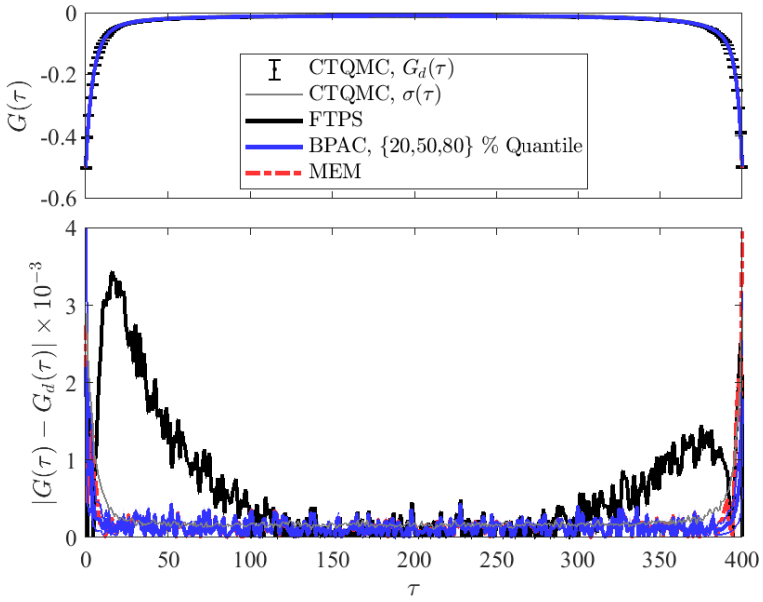

Figure 5.3: Imaginary-time Green's function (upper panel) and its deviation from the CTQMC data (lower panel) for the spin-down electrons. FTPS spectral function ($T = 0$ K) (black line) shows systematic deviations from the CTQMC data ($T = 29$ K) due to the difference in temperature.

asses the misfit in data space. Likewise, we can apply Eq. 5.2.3 to the FTPS spectral function to obtain the corresponding $G(\tau)$. The reconstructed Green's function for imaginary times $G(\tau)$ is compared with the CTQMC data $G_{\mathrm{d}}(\tau)$ in Fig. 5.3 for the MEM, BPAC, and FTPS. Even though the spectral functions of MEM and BPAC differ slightly, $G(\tau)$ of both solutions lies within the error of the CTQMC data. In the lower panel, the difference between $G(\tau)$ and $G_{\mathrm{d}}(\tau)$ is shown on an enlarged scale, which reveals a systematic deviation between FTPS and CTQMC data. The reason is that the FTPS solver calculates the spectral function at $T = 0$ K, whereas $\beta = 400$ $(\mathrm{eV})^{-1}$ ($T = 29$ K) is used in the CTQMC simulation.

The spectrum of the spin-up part of the AIM obtained with the FTPS solver is presented in Fig. 5.4 (black line) and shows a two-peak structure as does the MEM (red dash-dotted line). Hence, for parametrizing the spin-up spectral function in BPAC (blue line), we use a two-peak model $M_2 = M(\mathbf{C} = (1, 1))$ with the prior ranges given in Tab. A.2 in Appendix A.4. Since we are not interested in specific questions about spurious peaks, we are satisfied with model M_2.

5.6 Application II: MEM+BPAC

In this section, we propose a combination of MEM and BPAC (MEM+BPAC) and apply the method to the impurity problem studied in Ref. [46] for $SrVO_3$. We present the details of the AIM in Sec. 5.6.1, give the technical details of MEM+BPAC in Sec. 5.6.2, and discuss

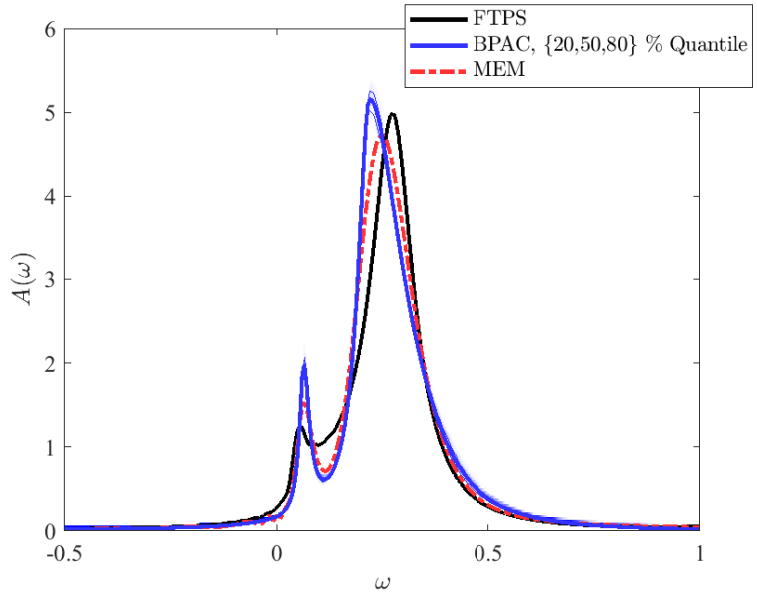

Figure 5.4: Spectral function for the up electrons obtained by the FTPS solver (black line), CTQMC+BPAC (blue line including confidence intervals), and CTQMC+MEM (red dash-dotted line). FTPS calculates the spectral function at $T = 0$ K, therefore, there are systematic deviations to the CTQMC+MEM and CTQMC+BPAC solutions obtained at $T = 29$ K.

the results in Sec. 5.6.3.

5.6.1 The impurity problem

The multi-orbital AIM discussed in Ref. [46] arises from the *ab initio* treatment of $SrVO_3$ which has become a test-bed material in DMFT. The solution of the AIM obtained with the FTPS solver shows a three-peak structure in the upper Hubbard band between 1.75 eV and 4.25 eV, see Fig. 5.5 (black line). Ref. [46] showed that CTQMC+MEM is not able to resolve these high-energy excitations. The question we want to address in this section is as follows: *Is the absence of the three-peak structure a failure of MEM, or is it - due to the ill-posed inversion problem - generally impossible to recover certain high-energy details of the spectrum?* To answer this question, we applied MEM+BPAC as explained in the following section.

5.6.2 Technical details and MEM+BPAC

In order to obtain an answer to this question, we start from the FTPS real-frequency data, transform them to the imaginary-time axis, and add noise on the order of the CTQMC error ($\sigma = 10^{-5}$). By this procedure, we ensure that we know precisely the error statistics of the data and we know that the correct result has to have the three-peak structure.

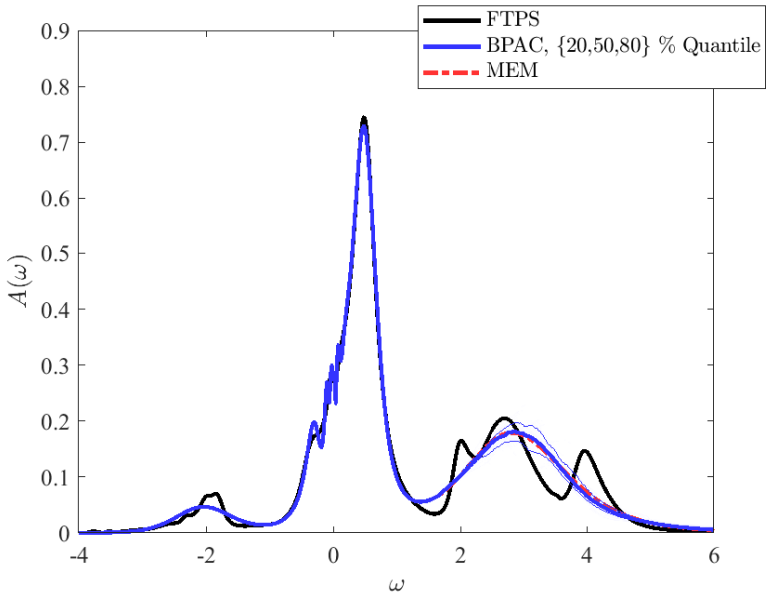

Figure 5.5: Spectral function of the AIM for $SrVO_3$ studied in Ref. [46]. The FTPS solution (black) shows a three-peak structure in the upper Hubbard band, whereas MEM (red dash-dotted) and MEM+BPAC using the three-peak model M_3 (blue) do not resolve these peaks.

We use an inverse temperature $\beta = 200\ (\mathrm{eV})^{-1}$ ($T = 58$ K), $N_\mathrm{d} = 501$ data points on an equally spaced τ grid in the interval $\tau \in [0, \beta]$ and the same amount of ω points equally spaced for $\omega \in [-4, 6]$.

Instead of using BPAC as explained in the previous sections, here, we apply a combination of MEM and BPAC. MEM+BPAC takes the MEM solution for a given subinterval of the energy axis and applies BPAC only for the remaining interval. In that way, the number of parameters is small, which enables faster sampling in the calculation of the evidence integral with NESA. We take $\Omega \in (1, 1.75)$ as an additional parameter and use the MEM solution for $\omega < \Omega$ and BPAC for $\omega \geqslant \Omega$. We use the prior ranges $1.75 < \mu_n < 4.25$ and $0 < a_n, \gamma_n^\mathrm{l}, \gamma_n^\mathrm{r} < 1$, and $C_n = 1$ for each peak n. Furthermore, the remaining parameters describing the right tail are constrained by $4.25 < \Omega^r < 6$, $-2 < \mu^r < 4.25$, and $1 < \nu^r < 10$. In NESA, we use $N_\mathrm{w} = 2000$ walkers and $\epsilon_\lambda = 10^{-5}$.

5.6.3 Comparison of the results

We applied the MEM of Ref. [56] with an alternative evidence approximation [196] and the preblur formalism [197] and were able to qualitatively reproduce the CTQMC+MEM solution in Fig. 5 of Ref. [46], see Fig. 5.5 (red dash-dotted line, mostly covered by the blue line). The MEM spectral function does not show the three-peak structure in the upper Hubbard band.

We applied MEM+BPAC using one-, two-, and three-peak models M_1, M_2, and M_3. The obtained logarithmic data evidences $\ln(p(\mathbf{G}_\mathrm{d}|M_i, \boldsymbol{\sigma}, \mathcal{I}))$ for $i \in \{1, 2, 3\}$ are $\{5036.7 \pm 0.2, 5036.0 \pm$

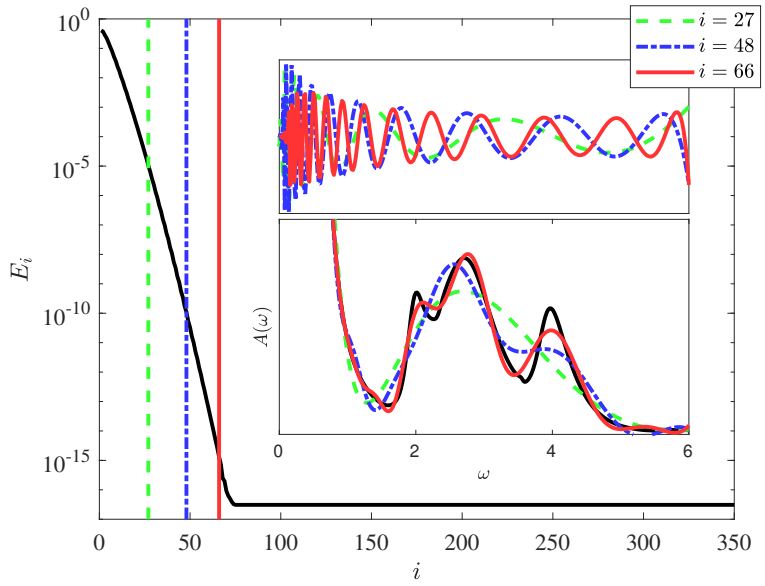

Figure 5.6: Singular values E_i versus index i for the kernel of the AIM for $SrVO_3$. For the selected singular mode indices 27 (green dashed, $E_{27} \approx 10^{-5}$), 48 (blue dash-dotted, $E_{48} \approx 10^{-10}$), and 66 (red, $E_{66} \approx 10^{-15}$), we show the singular modes $\mathbf{v}_i$ (upper inset) and the projected spectral functions $A(\omega)$ (see Eq. 5.6.5) for $N = 27, 48, 66$ (green dashed, blue dash-dotted, and red) (the lower inset). Although 66 singular modes resolve the three-peak structure, 27 and 48 do not.

$0.2, 5035.3 \pm 0.2\}$ and correspond to probabilities of 57 % for M_1, 29 % for M_2, and 14 % for M_3. It is interesting to note that the correct three-peak model actually has the lowest probability. Still, let us take a look at the result of M_3 shown in Fig. 5.5. Surprisingly, the three-peak model looks very similar to the MEM result, i.e., it is not even able to resolve the three-peak structure. Instead, it just shows one large peak in the energy region of the upper Hubbard band.

To elucidate this behavior, we consider the singular value representation of the kernel as suggested in Ref. [228],

$$K = \sum_i E_i \, \mathbf{u}_i \big(\mathbf{v}_i\big)^T \, . \tag{5.6.1}$$

Given the vector $\mathbf{A}$ of the discretized spectral function and the corresponding vector $\mathbf{G}$ of the Green's function for discrete imaginary times as defined in Sec. 5.2, we get

$$\mathbf{G} = K\mathbf{A} = \sum_i E_i \, \mathbf{u}_i \big(\mathbf{v}_i \cdot \mathbf{A}\big) \, . \tag{5.6.2}$$

The misfit defined in Eq. 5.4.2 can then be expressed in a very suggestive way. For simplicity, we assume constant noise $\sigma_l = \sigma$, $\forall l$. Then, the misfit to the data vector $\mathbf{G}_\mathrm{d}$ is

$$\chi^2 = \frac{1}{\sigma^2} \sum_i \Big(\big(\mathbf{G}_\mathrm{d} \cdot \mathbf{u}_i\big) - E_i \big(\mathbf{v}_i \cdot \mathbf{A}\big) \Big)^2 \, . \tag{5.6.3}$$

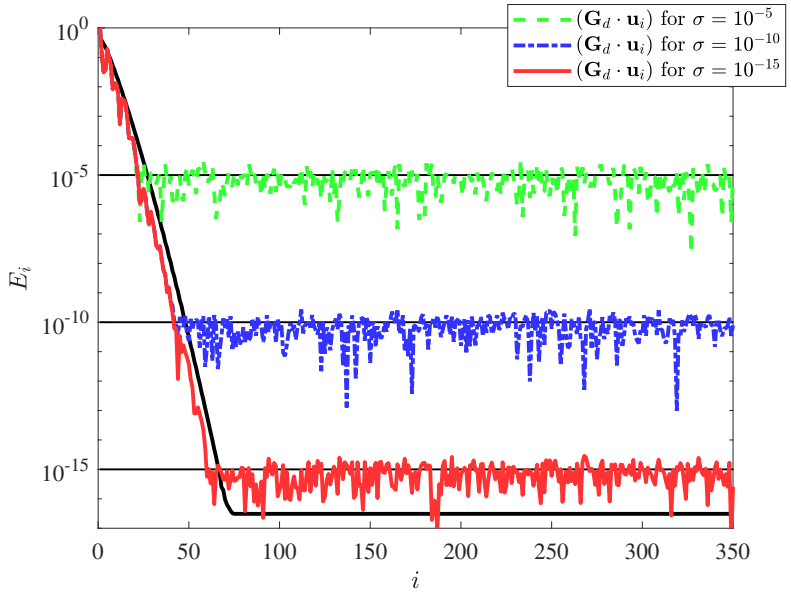

Figure 5.7: Singular values E_i versus index i for the kernel of the AIM for $SrVO_3$. $\left(\mathbf{G}_\mathrm{d} \cdot \mathbf{u}_i\right)$ is shown for selected noise levels.

In Fig. 5.6, the singular values E_i of the kernel matrix are plotted with decreasing magnitude on a logarithmic scale. We find that the singular values decrease exponentially and that, above $i = 70$, the singular values are smaller than machine precision. We select the three singular modes $i = \{27, 48, 66\}$ corresponding to singular values of approximately $\{10^{-5}, 10^{-10}, 10^{-15}\}$, respectively. The corresponding modes $\mathbf{v}_i$, which are depicted in the upper inset, show an increasing number of nodes with increasing index i. Minimization of Eq. 5.6.3 with respect to the spectral function $\mathbf{A}$ yields the maximum likelihood solution,

$$\mathbf{A}_\mathrm{ML} = \sum_i \frac{\left(\mathbf{G}_\mathrm{d} \cdot \mathbf{u}_i\right)}{E_i} \mathbf{v}_i \ . \tag{5.6.4}$$

Since the singular values decay exponentially, their inverse increases exponentially and small noise in the coefficients $\left(\mathbf{G}_\mathrm{d} \cdot \mathbf{u}_i\right)$ becomes amplified. Fig. 5.7 demonstrates nicely that $\left(\mathbf{G}_\mathrm{d} \cdot \mathbf{u}_i\right)$ becomes dominated by noise above the mode index i where the singular value E_i reaches the order of the noise σ. In order to see which part of the spectrum can, therefore, be reconstructed, we expand $\mathbf{A}$ into the mode vectors $\mathbf{v}_i$,

$$\mathbf{A} = \sum_{i=1}^{N} \left(\mathbf{A} \cdot \mathbf{v}_i\right) \mathbf{v}_i \ . \tag{5.6.5}$$

In the lower inset of Fig. 5.6, we present the projected FTPS spectrum for $N = 27, 48$, and 66. We observe that the three-peak structure is not resolvable at all with $N = 27$ and the resulting spectrum (green dashed line in the lower inset) looks similar to the MEM and MEM+BPAC solutions in Fig. 5.5. $N = 48$ allows to resolve two of the three peaks (blue dash-dotted line in the lower inset), whereas only $N = 66$ resolves the full three-peak structure (red line

in the lower inset). This demonstrates that, for a CTQMC error of $\sigma \geqslant 10^{-10}$, the AC kernel definitely does not allow to resolve the three-peak-structure. CTQMC errors of this magnitude, however, would imply enormous data-acquiring times, and even then only two of the three peaks would be visible.

5.7 Conclusions

We proposed a Bayesian parametric approach for the analytic continuation of noisy imaginary-time Green's function data, as e.g. obtained by CTQMC. The commonly used Bayesian form-free reconstruction of QMC data is the MEM which is based on the entropic prior that uses a minimum amount of prior information, merely positivity and additivity. Due to the nature of the form-free reconstruction, there are typically as many unknown parameters as noisy data points. This, in combination with the ill-conditioned kernel, can lead to spurious features in the reconstructed spectrum. In many applications, however, we have additional prior knowledge, e.g., we know that there will be a small number of peaklike structures of a specific shape. This prior knowledge can be encoded by representing the spectrum in terms of suitably parametrized basis functions, encoding the spectrum with only a few parameters, much less than the number of data points. Our approach, which we denote BPAC, employs Bayesian parameter estimation to obtain the parametrized spectral function. In the present chapter, we used asymmetric Lorentzians and additional tails. Of course, in other applications a different basis might be favorable.

Moreover, we employed Bayesian model comparison to validate different numbers of Lorentzian peaks. For Bayesian model comparison, the evaluation of high-dimensional evidence integrals is necessary. To this end, we employ NESA which is particularly efficient for such integration problems.

We demonstrated the capability of BPAC in terms of the CTQMC data for an AIM closely related to the AIM describing CuPc on Ag(111) discussed in Sec. 4.4.2. We compared the BPAC spectra to the MEM result as well as the spectral function obtained with the real-time FTPS impurity solver. It was shown that BPAC is able to tell true peaks from artifacts which are present in the MEM's solution close to Abrikosov-Suhl resonance.

In a second application, we studied the AIM arising from the *ab initio* treatment of $SrVO_3$. The spectral function obtained with the real-time FTPS solver shows a three-peak structure in the upper Hubbard band which is not present in the MEM reconstruction of the CTQMC data. Although the MEM cannot resolve the three-peak structure, the rest of the spectrum is captured well. To start with a data set that definitely contains the three-peak structure, we generated imaginary-time data from the real-frequency FTPS spectrum. Adding noise to simulate the CTQMC error, we studied the MEM and BPAC reconstructions of this data set. To keep the number of parameters and, therefore, the numerical effort small, we employed BPAC focused on the structure in the upper Hubbard band. Therefore, we only described the upper part of the spectrum by Lorentzians whereas keeping the MEM reconstruction for the rest of the spectrum. Bayesian model comparison then allows to infer which details of

the upper Hubbard band can reliably be inferred from the data. Considering the singular value decomposition of the kernel allows us to find rigorous arguments how numerical noise is propagated by the kernel. Remarkably, we found that the information of the three-peak structure present in the real-frequency spectrum is attenuated by ten orders of magnitude during the transformation to imaginary-time space. It is, therefore, buried in the noise and impossible to be retrieved from the QMC data. This means that independent of the model chosen, we obtained a single large peak resembling the MEM solution. Although BPAC was not able to reconstruct the true shape of the upper Hubbard band, its advantage is that it reliably detects how many details of the spectrum are actually above the noise threshold in the data.

Therefore, we conclude that BPAC is a valuable addition to nonparametric reconstruction methods such as MEM. The reconstruction can be performed either only with BPAC or with a MEM reconstruction that can be used first, and BPAC is employed to assess whether the data support specific features found in the MEM spectral function.

Appendix A

Appendix

A.1 Pt-BDT-Pt: Parameters of the Hamiltonian

The matrices in A.1.1, A.1.2 and A.1.3 are the one-particle parameters of the Hamiltonian for the Pt-BDT-Pt system discussed in detail in Sec 3.4. $\tilde{t}$ are the hopping parameters of the central region, where the double counting is not yet subtracted, and $V_{\mathrm{T_L C}}$ and $V_{\mathrm{CT_R}}$ are the coupling matrices between the central region and the transition layers. The row and column indices of $\tilde{t}$ correspond to the basis functions presented in Fig. 3.6(b).

$$V_{\mathrm{T_L C}} = \begin{pmatrix} -1.11 & 0.08 & 0.01 & -0.34 & 0.14 & -0.02 & -0.02 & 0.00 \\ -0.85 & 0.11 & 0.00 & 0.08 & -0.05 & -0.02 & 0.01 & 0.00 \end{pmatrix} \tag{A.1.1}$$

$$\tilde{t} = \begin{pmatrix} -1.46 & -2.12 & 0.21 & 0.17 & 0.07 & 0 & 0.05 & -0.03 \\ -2.12 & -0.29 & -2.58 & -2.54 & 0.01 & 0.27 & -0.23 & 0.05 \\ 0.21 & -2.58 & 0.16 & 0.01 & -0.08 & -2.77 & 0.02 & 0.07 \\ 0.17 & -2.54 & 0.01 & 0.53 & -2.77 & -0.24 & 0.27 & 0 \\ 0.07 & 0.01 & -0.08 & -2.77 & 0.16 & 0.01 & -2.58 & 0.21 \\ 0 & 0.27 & -2.77 & -0.24 & 0.01 & 0.52 & -2.54 & 0.18 \\ 0.05 & -0.23 & 0.02 & 0.27 & -2.58 & -2.54 & -0.29 & -2.12 \\ -0.03 & 0.05 & 0.07 & 0 & 0.21 & 0.18 & -2.12 & -1.46 \end{pmatrix} \tag{A.1.2}$$

$$V^{\dagger}_{\mathrm{CT_R}} = \begin{pmatrix} 0.00 & 0.02 & -0.14 & 0.03 & -0.01 & 0.34 & -0.08 & 1.11 \\ 0.00 & -0.01 & 0.05 & 0.02 & 0.00 & -0.08 & -0.11 & 0.85 \end{pmatrix} \tag{A.1.3}$$

The interaction parameters U_{ij} determined by numerical integration of Eq. 3.2.1 are

$$U = \begin{pmatrix} 7.72 & 4.86 & 3.24 & 3.25 & 2.27 & 2.21 & 1.96 & 1.49 \\ 4.86 & 8.52 & 5.06 & 4.97 & 3.34 & 3.23 & 2.85 & 1.96 \\ 3.24 & 5.06 & 8.67 & 3.32 & 3.00 & 5.04 & 3.34 & 2.27 \\ 3.25 & 4.97 & 3.32 & 7.93 & 5.03 & 2.86 & 3.23 & 2.22 \\ 2.27 & 3.34 & 3.00 & 5.03 & 8.67 & 3.32 & 5.06 & 3.24 \\ 2.21 & 3.23 & 5.04 & 2.86 & 3.32 & 7.94 & 4.97 & 3.26 \\ 1.96 & 2.85 & 3.34 & 3.23 & 5.06 & 4.97 & 8.52 & 4.86 \\ 1.49 & 1.96 & 2.27 & 2.22 & 3.24 & 3.26 & 4.86 & 7.72 \end{pmatrix}. \quad \text{(A.1.4)}$$

The relative integration error is within 5 %.

A.2 CuPc on Au(111) and Ag(111): Density functional calculation details

The DFT calculations of CuPc on Au(111) and Ag(111) presented in Chpt. 4 are performed with SIESTA [84] and TranSIESTA [85]. We use the Perdew-Burke-Ernzerhof (PBE) [193] functional which is a generalized gradient approximation (GGA) functional. To suppress periodicity effects, we perform the calculations at the Γ point, except for the electrode calculations where we use 100 k points in the transport direction with one electrode unit cell consisting of six metal layers. For an appropriate description of the surface, we have to ensure that the super cell is large enough parallel to the surface in order to justify a Γ point calculation. For computational reasons, we restrict ourselves to the p(6×5) surface and discuss possible consequences in Sec. 4.4.3. We use 300 Ry mesh-cutoff and an electronic temperature of 5 meV. For the H, C, N, and Cu atoms we use non-relativistic norm-conserving pseudopotentials [229] from the Abinit's pseudo database[1] and for Au and Ag relativistic pseudopotentials as recommended by Rivero *et al.* [230]. For the basis set, we restrict ourselves to the standard single-zeta basis plus polarization (SZP) and double-zeta basis plus polarization (DZP) basis sets with an energy shift of 0.01 Ry. We perform our calculations using an SZP basis set for the bulk atoms and a DZP basis set for the atoms in the molecule, the first 2 layers of the metal surface, as well as the tip. Additionally, we use an extended cutoff radius of 7.5 Å for the first zeta basis functions of the four atoms at the tip for calculating the transmissions. We successfully benchmark the pseudopotentials and basis sets calculating the bulk band structure with SIESTA and Quantum Espresso [147]. We apply TranSIESTA in equilibrium and choose the complex contour consisting of a circular part from -40 eV to $-10\ k_{\mathrm{B}}T$ and a tail to infinity. The imaginary part of the Fermi function tail when crossing the Fermi level is chosen to be 2.5 eV and a Gauss-Legendre quadrature with 96 points is used for the circular part and a Gauss-Fermi quadrature with 16 points is used for the tail of the complex contour.

[1] `https://departments.icmab.es/leem/siesta/Databases/Pseudopotentials/periodictable-gga-abinit.html`

A.3 BPAC: Thermodynamic integration

In Sec. 5.4.2, we introduced NESA as a method for calculating high-dimensional integrals such as the data evidence. To check all the calculated data evidences, we employed thermodynamic integration (TI) [53, 54] in addition to NESA. TI was developed in statistical physics [231] and independently discovered by Ref. [232]. We briefly discuss the basic principles of TI in the present section.

We aim to calculate the data evidence integral

$$Z(\beta) = \int d\boldsymbol{\alpha}\; L(\boldsymbol{\alpha})^{\beta}\pi(\boldsymbol{\alpha}) \tag{A.3.1}$$

where we introduced an auxiliary parameter β. The case $\beta = 0$ produces the prior normalization, $Z(0) = 1$, and $\beta = 1$ the data evidence, $Z = Z(1)$. Derivation of $\ln(Z(\beta))$ with respect to β leads to

$$\frac{\partial}{\partial\beta}\ln(Z(\beta)) = \int d\boldsymbol{\alpha}\, \underbrace{\frac{\pi(\boldsymbol{\alpha})}{Z(\beta)}L(\boldsymbol{\alpha})^{\beta}}_{p_\beta(\boldsymbol{\alpha})}\ln(L(\boldsymbol{\alpha})) = \langle\ln(L(\boldsymbol{\alpha}))\rangle_\beta\ . \tag{A.3.2}$$

The logarithm of the data evidence is therefore an integral over this expectation value,

$$\ln(Z) = \ln(Z(1)) - \ln(Z(0)) = \int_0^1 d\beta\,\langle\ln(L(\boldsymbol{\alpha}))\rangle_\beta\ . \tag{A.3.3}$$

The expectation value $\langle\ln(L(\boldsymbol{\alpha}))\rangle_\beta$ for a certain temperature β can be estimated by a MCMC run obeying $p_\beta(\boldsymbol{\alpha})$. To improve the numerical evaluation of Eq. A.3.3, it is advantageous to apply a nonlinear transformation [49], e.g.,

$$\beta(z) = \frac{2z^n}{1+z^n} \tag{A.3.4}$$

with a fixed n and $z \in [0,1]$ equally spaced, and to solve the integral

$$\ln(Z) = \int_0^1 dz\;\frac{d\beta}{dz}\langle\ln(L(\boldsymbol{\alpha}))\rangle_{\beta(z)} \tag{A.3.5}$$

by using numerical integration techniques, e.g., Romberg integration [233]. The final result suffers from two sources of error: the statistical error of the MCMC runs and the integration error.

A.4 BPAC: Prior ranges and estimated parameters

Tab. A.1 shows the prior ranges and the estimated parameters for the four-peak model M_4 of the spin-down spectral function of the AIM discussed in Sec. 5.5.

	μ_n	a_n	γ_n^{l}	γ_n^{r}
prior range	(-0.4, -0.2)	(0, 1)	(0.001, 0.3)	(0.001, 0.3)
estimator	-0.32 ± 0.04	0.7 ± 0.1	0.20 ± 0.06	0.18 ± 0.06
prior range	(-0.07, -0.03)	(0, 0.5)	(0.001, 0.1)	(0.001, 0.1)
estimator	-0.05 ± 0.01	0.08 ± 0.04	0.06 ± 0.03	0.04 ± 0.02
prior range	(-0.02, 0.02)	(0, 0.5)	(0.001, 0.1)	(0.001, 0.1)
estimator	0.001 ± 0.003	0.022 ± 0.005	0.008 ± 0.004	0.006 ± 0.003
prior range	(0.1, 0.25)	(0, 1)	(0.001, 0.3)	(0.001, 0.3)
estimator	0.22 ± 0.02	0.6 ± 0.1	0.06 ± 0.01	0.09 ± 0.05

		Ω	μ	ν
left tail	prior range	(-0.5, -0.4)	(-0.4, 0.5)	(1, 10)
	estimator	-0.45 ± 0.03	0.0 ± 0.2	7 ± 2
right tail	prior range	(0.25, 0.5)	(-0.5, 0.25)	(1, 10)
	estimator	0.36 ± 0.07	-0.1 ± 0.2	7 ± 2

Table A.1: Prior ranges and estimated parameters for model M_4 of the spin-down spectral function.

Tab. A.2 shows the prior ranges and the estimated parameters for the two-peak model M_2 of the spin-up spectral function of the AIM discussed in Sec. 5.5.

	μ_n	a_n	γ_n^{l}	γ_n^{r}
prior range	(0.03, 0.07)	(0, 0.1)	(0.001, 0.1)	(0.001, 0.1)
estimator	0.063 ± 0.001	0.078 ± 0.002	0.0116 ± 0.0004	0.016 ± 0.002
prior range	(0.2, 0.3)	(0, 1.5)	(0.001, 0.5)	(0.001, 0.5)
estimator	0.218 ± 0.002	1.06±0.03	0.0320 ± 0.0007	0.100 ± 0.007

		Ω	μ	ν
left tail	prior range	(0, 0.03)	(0.03, 0.5)	(1, 10)
	estimator	0.003 ± 0.001	0.1076 ± 0.0007	1.281 ± 0.005
right tail	prior range	(0.3, 0.5)	(-0.5, 0.3)	(1, 10)
	estimator	0.37 ± 0.04	0.0 ± 0.2	4 ± 2

Table A.2: Prior ranges and estimated parameters for model M_2 of the spin-up spectral function.

List of Figures

List of Publications and Presentations

This section lists peer-reviewed articles published during the time of working on this thesis, oral presentations, and some selected poster presentations given at conferences, workshops, and schools.

Peer-reviewed articles

- **M. Rumetshofer**, G. Dorn, L. Boeri, E. Arrigoni, W. von der Linden
  First-principles molecular transport calculation for the benzenedithiolate molecule
  New J. Phys. **19** 103007, October 2017.
- **M. Rumetshofer**, P. Heim, B. Thaler, W. E. Ernst, M. Koch, W. von der Linden
  Analysis of femtosecond pump-probe photoelectron-photoion coincidence measurements applying Bayesian probability theory
  Phys. Rev. A **97** 062503, June 2018.
- M. J. Pfeifenberger, **M. Rumetshofer**, W. von der Linden
  Nested sampling, statistical physics and the Potts model
  J. Comput. Phys. **375** 368, December 2018.
- P. Heim, **M. Rumetshofer**, S. Ranftl, B. Thaler, W. E. Ernst, M. Koch, W. von der Linden
  Bayesian Analysis of Femtosecond Pump-Probe Photoelectron-Photoion Coincidence Spectra with Fluctuating Laser Intesities
  Entropy **21** 93, January 2019.
- **M. Rumetshofer**, D. Bauernfeind, E. Arrigoni and W. von der Linden
  First-principles quantum transport simulation of CuPc on Au(111) and Ag(111)
  Phys. Rev. B **99** 045148, January 2019.
- M. P. K. Frewein, **M. Rumetshofer**, G. Pabst
  Global small-angle scattering data analysis of inverted hexagonal phases
  J. Appl. Crystallogr. **52** 403, April 2019.

- **M. Rumetshofer**, D. Bauernfeind, W. von der Linden
  Bayesian parametric analytic continuation of Green's functions
  Phys. Rev. B **100** 075137, August 2019.

Oral presentations

- **M. Rumetshofer**
  Quantum transport simulations of BDT and CuPc and Bayesian parametric analytic continuation
  Physikalisches Oberseminar, Graz, Austria, 10.05.2019.

Poster presentations

- **M. Rumetshofer**, L. Boeri, W. von der Linden
  First-principle molecular transport calculation
  PISACMS: Paris International School on Advanced Computational Materials Science, Paris, France, 31.08.2016.
- **M. Rumetshofer**, L. Boeri, W. von der Linden
  First-principle molecular transport calculation
  Winter school: Magnetism, Vienna, Austria, 20.01.2017.
  DPG-Frühjahrstagung, Dresden, Germany, 20.03.2017.
  Ab-initio Electronic Structure for Solids in the 21st Century, Bad Honnef, Germany, 31.10.2017.
- **M. Rumetshofer**, D. Bauernfeind, W. von der Linden
  CuPc on Au(111) and Ag(111), Bayesian Analytic Continuation
  Autumn school on Correlated Electrons: DMFT - From Infinite Dimensions to Real Materials, Jülich, Germany, 19.09.2018.
  TranSIESTA and TBtrans workshop: Multi-electrode nanoscale transport with nonequilibrium Greens Functions - From tight-binding to DFT, Copenhagen, Denmark, 21.11.2018.

Bibliography

[1] D. A. Ryndyk. *Theory of Quantum Transport at Nanoscale. An Introduction* (Springer International Publishing, Switzerland, 2016) (see pp. 1, 5).

[2] A. Ghosh. *Nanoelectronics. A Molecular View* (World Scientific Publishing, Singapure, 2016) (see pp. 1, 5).

[3] S. Datta. *Lessons from Nanoelectronics. A New Perspective on Transport* (World Scientific Publishing, Singapure, 2012) (see pp. 1, 5).

[4] J. C. Cuevas and E. Scheer. *Molecular Electronics. An Introduction to Theory and Experiment* (World Scientific Publishing, Singapure, 2010) (see pp. 1, 5, 25).

[5] *Introducing Molecular Electronics. Lecture Notes in Physics* (eds G. Cuniberti, G. Fagas, and K. Richter) (Springer, Berlin, Heidelberg, 2005) (see pp. 1, 25, 27).

[6] C. Joachim and M. A. Ratner. Molecular electronics: Some views on transport junctions and beyond. *Proc. Natl. Acad. Sci. USA* 102, 8801 (2005) (see p. 1).

[7] W. Kohn. Nobel Lecture: Electronic structure of matter—wave functions and density functionals. *Rev. Mod. Phys.* 71, 1253 (1999) (see p. 1).

[8] L. P. Kadanoff and G. Baym. *Quantum Statistical Mechanics* (W. A. Benjamin, New York, 1962) (see pp. 1, 8).

[9] L. V. Keldysh. Diagram technique for nonequilibrium processes. *J. Exptl. Theoret. Phys.* 47, 1515 (1964) (see pp. 1, 8).

[10] K. S. Thygesen and A. Rubio. Conserving *GW* scheme for nonequilibrium quantum transport in molecular contacts. *Phys. Rev. B* 77, 115333 (2008) (see p. 1).

[11] D. Jacob. Towards a full ab initio theory of strong electronic correlations in nanoscale devices. *J. Phys. Condens. Matter* 27, 245606 (2015) (see pp. 1, 27).

[12] H. Breuer and F. Petruccione. *The Theory of Open Quantum Systems* (Oxford University Press, New York, 2007) (see p. 1).

[13] P. W. Anderson. Localized Magnetic States in Metals. *Phys. Rev.* 124, 41 (1961) (see pp. 1, 38).

[14] E. Gull, A. J. Millis, A. I. Lichtenstein, A. N. Rubtsov, M. Troyer, and P. Werner. Continuous-time Monte Carlo methods for quantum impurity models. *Rev. Mod. Phys.* 83, 349 (2011) (see pp. 2, 33, 34).

[15] M. A. Reed, C. Zhou, C. J. Muller, T. P. Burgin, and J. M. Tour. Conductance of a Molecular Junction. *Science* 278, 252 (1997) (see pp. 2, 43).

[16] E. Lörtscher, H. B. Weber, and H. Riel. Statistical Approach to Investigating Transport through Single Molecules. *Phys. Rev. Lett.* 98, 176807 (2007) (see pp. 2, 43).

[17] H. Song, Y. Kim, Y. H. Jang, H. Jeong, M. A. Reed, and T. Lee. Observation of molecular orbital gating. *Nature* 462, 1039 (2009) (see pp. 2, 43, 49, 54).

[18] X. Xiao, B. Xu, and N. J. Tao. Measurement of Single Molecule Conductance: Benzenedithiol and Benzenedimethanethiol. *Nano Lett.* 4, 267 (2004) (see pp. 2, 43, 49, 54).

[19] M. Tsutsui, M. Taniguchi, and T. Kawai. Atomistic Mechanics and Formation Mechanism of Metal-Molecule-Metal Junctions. *Nano Lett.* 9, 2433 (2009) (see pp. 2, 43, 49, 54).

[20] M. Kiguchi, H. Nakamura, Y. Takahashi, T. Takahashi, and T. Ohto. Effect of Anchoring Group Position on Formation and Conductance of a Single Disubstituted Benzene Molecule Bridging Au Electrodes: Change of Conductive Molecular Orbital and Electron Pathway. *J. Phys. Chem. C* 114, 22254 (2010) (see pp. 2, 43, 49, 54).

[21] Y. Kim, T. Pietsch, A. Erbe, W. Belzig, and E. Scheer. Benzenedithiol: A Broad-Range Single-Channel Molecular Conductor. *Nano Lett.* 11, 3734 (2011) (see pp. 2, 43, 54).

[22] Z. Xie, I. Baldea, C. E. Smith, Y. Wu, and C. D. Frisbie. Experimental and Theoretical Analysis of Nanotransport in Oligophenylene Dithiol Junctions as a Function of Molecular Length and Contact Work Function. *ACS Nano* 9, 8022 (2015) (see pp. 2, 43, 54).

[23] Y. Xue, S. Datta, and M. A. Ratner. Charge transfer and "band lineup" in molecular electronic devices: A chemical and numerical interpretation. *J. Chem. Phys.* 115, 4292 (2001) (see pp. 2, 43, 54).

[24] M. di Ventra, S. T. Pantelides, and N. D. Lang. First-Principles Calculation of Transport Properties of a Molecular Device. *Phys. Rev. Lett.* 84, 979 (2000) (see pp. 2, 43, 49).

[25] H. Kondo, H. Kino, J. Nara, T. Ozaki, and T. Ohno. Contact-structure dependence of transport properties of a single organic molecule between Au electrodes. *Phys. Rev. B* 73, 235323 (2006) (see pp. 2, 43, 49).

[26] A. d. M. Souza, I. Rungger, R. B. Pontes, A. R. Rocha, A. J. R. da Silva, U. Schwingenschloegl, and S. Sanvito. Stretching of BDT-gold molecular junctions: thiol or thiolate termination? *Nanoscale* 6, 14495 (2014) (see pp. 2, 43, 49, 54).

[27] M. Strange, C. Rostgaard, H. Häkkinen, and K. S. Thygesen. Self-consistent GW calculations of electronic transport in thiol- and amine-linked molecular junctions. *Phys. Rev. B* 83, 115108 (2011) (see pp. 2, 43, 49, 54, 58).

[28] R. B. Pontes, A. R. Rocha, S. Sanvito, A. Fazzio, and A. J. R. da Silva. Ab Initio Calculations of Structural Evolution and Conductance of Benzene-1,4-dithiol on Gold Leads. *ACS Nano* 5, 795 (2011) (see pp. 2, 43).

[29] C. Toher and S. Sanvito. Efficient Atomic Self-Interaction Correction Scheme for Nonequilibrium Quantum Transport. *Phys. Rev. Lett.* 99, 056801 (2007) (see pp. 2, 27, 43).

[30] T. Rangel, A. Ferretti, V. Olevano, and G.-M. Rignanese. Many-body correlations and coupling in benzene-dithiol junctions. *Phys. Rev. B* 95, 115137 (2017) (see pp. 2, 43).

[31] N. Marzari and D. Vanderbilt. Maximally localized generalized Wannier functions for composite energy bands. *Phys. Rev. B* 56, 12847 (1997) (see pp. 2, 23).

[32] I. Souza, N. Marzari, and D. Vanderbilt. Maximally localized Wannier functions for entangled energy bands. *Phys. Rev. B* 65, 035109 (2001) (see pp. 2, 23).

[33] D. Sénéchal. An introduction to quantum cluster methods. *ArXiv e-prints.* arXiv:0806.2690 (2008) (see pp. 2, 15).

[34] J. Kondo. Resistance Minimum in Dilute Magnetic Alloys. *Prog. Theor. Phys.* 32, 37 (1964) (see pp. 2, 37, 59).

[35] A. C. Hewson. *The Kondo Problem to Heavy Fermions* (Cambridge University Press, Cambridge, 1993) (see pp. 2, 37, 40, 42, 59).

[36] D. Goldhaber-Gordon, H. Shtrikman, D. Mahalu, D. Abusch-Magder, U. Meirav, and M. A. Kastner. Kondo effect in a single-electron transistor. *Nature* 391, 156 (1998) (see pp. 2, 59).

[37] J. Park, A. N. Pasupathy, J. I. Goldsmith, C. Chang, Y. Yaish, J. R. Petta, M. Rinkoski, J. P. Sethna, H. D. Abruna, P. L. McEuen, and D. C. Ralph. Coulomb blockade and the Kondo effect in single-atom transistors. *Nature* 417, 722 (2002) (see pp. 2, 59).

[38] V. Madhavan, W. Chen, T. Jamneala, M. F. Crommie, and N. S. Wingreen. Tunneling into a Single Magnetic Atom: Spectroscopic Evidence of the Kondo Resonance. *Science* 280, 567 (1998) (see pp. 2, 37).

[39] J. Li, W.-D. Schneider, R. Berndt, and B. Delley. Kondo Scattering Observed at a Single Magnetic Impurity. *Phys. Rev. Lett.* 80, 2893 (1998) (see pp. 2, 37).

[40] H. C. Manoharan, C. P. Lutz, and D. M. Eigler. Quantum mirages formed by coherent projection of electronic structure. *Nature* 403, 512 (2000) (see pp. 2, 37).

[41] A. Mugarza, C. Krull, R. Robles, S. Stepanow, G. Ceballos, and P. Gambardella. Spin coupling and relaxation inside molecule–metal contacts. *Nat. Commun.* 2, 490 (2011) (see pp. 2, 59–61, 64, 67, 69, 70, 72–74).

[42] A. Mugarza, R. Robles, C. Krull, R. Korytár, N. Lorente, and P. Gambardella. Electronic and magnetic properties of molecule-metal interfaces: Transition-metal phthalocyanines adsorbed on Ag(100). *Phys. Rev. B* 85, 155437 (2012) (see pp. 2, 59–61, 64, 70, 72, 74).

[43] J. Ziroff, S. Hame, M. Kochler, A. Bendounan, A. Schöll, and F. Reinert. Low-energy scale excitations in the spectral function of organic monolayer systems. *Phys. Rev. B* 85, 161404 (2012) (see pp. 2, 59, 60, 64).

[44] Y. L. Huang, E. Wruss, D. A. Egger, S. Kera, N. Ueno, W. A. Saidi, T. Bucko, A. T. Wee, and E. Zojer. Understanding the Adsorption of CuPc and ZnPc on Noble Metal Surfaces by Combining Quantum-Mechanical Modelling and Photoelectron Spectroscopy. *Molecules* 19, 2969 (2014) (see pp. 2, 59–62, 64, 66, 73).

[45] A. Droghetti and I. Rungger. Quantum transport simulation scheme including strong correlations and its application to organic radicals adsorbed on gold. *Phys. Rev. B* 95, 085131 (2017) (see pp. 2, 29, 73).

[46] D. Bauernfeind, M. Zingl, R. Triebl, M. Aichhorn, and H. G. Evertz. Fork Tensor-Product States: Efficient Multiorbital Real-Time DMFT Solver. *Phys. Rev. X* 7, 031013 (2017) (see pp. 2, 33, 35, 86–88).

[47] D. Bauernfeind, R. Triebl, M. Zingl, M. Aichhorn, and H. G. Evertz. Dynamical mean-field theory on the real-frequency axis: $p-d$ hybridization and atomic physics in $SrMnO_3$. *Phys. Rev. B* 97, 115156 (2018) (see pp. 2, 35).

[48] D. Bauernfeind. Fork Tensor Product States. Efficient Multi-Orbital Impurity Solver for Dynamical Mean Field Theory. PhD thesis (Graz University of Technology, Austria, 2018) (see pp. 2, 35).

[49] W. von der Linden, V. Dose, and U. von Toussaint. *Bayesian Probability Theory. Applications in the Physical Sciences* (Cambridge University Press, Cambridge, 2014) (see pp. 2, 76, 81–83, 95).

[50] P. Gregory. *Bayesian Logical Data Analysis for the Physical Sciences. A Comparative Approach with Mathematica® Support* (Cambridge University Press, New York, 2005) (see pp. 2, 76).

[51] E. T. Jaynes. *Probability Theory. The Logic of Science* (ed G. L. Bretthorst) (Cambridge University Press, New York, 2003) (see pp. 2, 76).

[52] D. S. Sivia and J. Skilling. *Data Analysis. A Bayesian Tutorial* (Oxford University Press, Oxford, 2006) (see pp. 2, 76, 81, 83).

[53] A. Gelman and X.-L. Meng. Simulating normalizing constants: from importance sampling to bridge sampling to path sampling. *Statist. Sci.* 13, 163 (1998) (see pp. 2, 76, 95).

[54] R. M. Neal. Markov Chain Sampling Methods for Dirichlet Process Mixture Models. *J. Comput. Graph. Stat.* 9, 249 (2000) (see pp. 2, 76, 95).

[55] J. Skilling. Nested Sampling. *AIP Conf. Proc.* 735, 395 (2004) (see pp. 2, 76, 81).

[56] M. Jarrell and J. Gubernatis. Bayesian inference and the analytic continuation of imaginary-time quantum Monte Carlo data. *Phys. Rep.* 269, 133 (1996) (see pp. 2, 63, 84, 88).

[57] P. Coleman. *Introduction to Many-Body Physics* (Cambridge University Press, Cambridge, 2015) (see pp. 5, 8, 37, 40, 41).

[58] W. Nolting. *Grundkurs Theoretische Physik 7. Viel-Teilchen-Theorie* (Springer, Berlin, Heidelberg, 2009) (see p. 5).

[59] H. Haug and A. P. Jauho. *Quantum Kinetics in Transport and Optics of Semiconductors* (Springer, Berlin, Heidelberg, 2008) (see pp. 5, 8, 16).

[60] A. Fetter and J. Walecka. *Quantum Theory of Many-particle Systems* (Dover Publications, New York, 2003) (see pp. 5, 9).

[61] P. Fulde. *Electron Correlations in Molecules and Solids* (Springer, Berlin, Heidelberg, 1995) (see pp. 5, 37).

[62] K. S. Thygesen. Electron transport through an interacting region: The case of a nonorthogonal basis set. *Phys. Rev. B* 73, 035309 (2006) (see p. 7).

[63] J. Fransson, O. Eriksson, and I. Sandalov. Effects of nonorthogonality in the time-dependent current through tunnel junctions. *Phys. Rev. B* 64, 153403 (2001) (see p. 7).

[64] J. Fransson, O. Eriksson, and I. Sandalov. Effects of non-orthogonality and electron correlations on the time-dependent current through quantum dots. *Phys. Rev. B* 66, 195319 (2002) (see p. 7).

[65] M. Soriano and J. J. Palacios. Theory of projections with nonorthogonal basis sets: Partitioning techniques and effective Hamiltonians. *Phys. Rev. B* 90, 075128 (2014) (see p. 7).

[66] J. Rammer and H. Smith. Quantum field-theoretical methods in transport theory of metals. *Rev. Mod. Phys.* 58, 323 (1986) (see p. 8).

[67] F. J. Dyson. The S Matrix in Quantum Electrodynamics. *Phys. Rev.* 75, 1736 (1949) (see p. 14).

[68] C. Gros and R. Valenti. Cluster expansion for the self-energy: A simple many-body method for interpreting the photoemission spectra of correlated Fermi systems. *Phys. Rev. B* 48, 418 (1993) (see p. 15).

[69] Y. Meir and N. S. Wingreen. Landauer formula for the current through an interacting electron region. *Phys. Rev. Lett.* 68, 2512 (1992) (see p. 16).

[70] R. Landauer. Spatial Variation of Currents and Fields Due to Localized Scatterers in Metallic Conduction. *IBM J. Res. Dev.* 1, 223 (1957) (see p. 16).

[71] M. Büttiker, Y. Imry, R. Landauer, and S. Pinhas. Generalized many-channel conductance formula with application to small rings. *Phys. Rev. B* 31, 6207 (1985) (see p. 16).

[72] D. A. Ryndyk, R. Gutiérrez, B. Song, and G. Cuniberti. Green Function Techniques in the Treatment of Quantum Transport at the Molecular Scale. In: *Energy Transfer Dynamics in Biomaterial Systems* (eds I. Burghardt, V. May, D. A. Micha, and E. R. Bittner) (Springer, Berlin, Heidelberg, 2009) (see p. 16).

[73] H. Ness, L. K. Dash, and R. W. Godby. Generalization and applicability of the Landauer formula for nonequilibrium current in the presence of interactions. *Phys. Rev. B* 82, 085426 (2010) (see pp. 18, 20).

[74] T.-K. Ng. ac Response in the Nonequilibrium Anderson Impurity Model. *Phys. Rev. Lett.* 76, 487 (1996) (see p. 18).

[75] A. Ferretti, A. Calzolari, R. Di Felice, and F. Manghi. First-principles theoretical description of electronic transport including electron-electron correlation. *Phys. Rev. B* 72, 125114 (2005) (see p. 19).

[76] A. A. Aligia. Nonequilibrium self-energies, Ng approach, and heat current of a nanodevice for small bias voltage and temperature. *Phys. Rev. B* 89, 125405 (2014) (see p. 20).

[77] A. P. Jauho. Modelling of inelastic effects in molecular electronics. *J. Phys. Conf. Ser.* 35, 313 (2006) (see p. 20).

[78] G. Czycholl. *Theoretische Festkörperphysik Band 1. Grundlagen: Phononen und Elektronen in Kristallen* (Springer, Berlin, Heidelberg, 2016) (see p. 21).

[79] M. Rumetshofer. First-principles molecular transport calculations. Master's thesis (Graz University of Technology, Austria, 2016) (see pp. 21, 23, 44).
[80] P. Hohenberg and W. Kohn. Inhomogeneous Electron Gas. *Phys. Rev.* 136, B864 (1964) (see p. 21).
[81] W. Kohn and L. J. Sham. Self-Consistent Equations Including Exchange and Correlation Effects. *Phys. Rev.* 140, A1133 (1965) (see p. 21).
[82] M. Strange, I. S. Kristensen, K. S. Thygesen, and K. W. Jacobsen. Benchmark density functional theory calculations for nanoscale conductance. *J. Chem. Phys.* 128, 114714 (2008) (see pp. 23, 27).
[83] A. A. Mostofi, J. R. Yates, G. Pizzi, Y.-S. Lee, I. Souza, D. Vanderbilt, and N. Marzari. An updated version of wannier90: A tool for obtaining maximally-localised Wannier functions. *Comput. Phys. Commun.* 185, 2309 (2014) (see pp. 23, 44).
[84] J. M. Soler, E. Artacho, J. D. Gale, A. García, J. Junquera, P. Ordejón, and D. Sánchez-Portal. The SIESTA method for *ab initio* order-N materials simulation. *J. Phys. Condens. Matter* 14, 2745 (2002) (see pp. 24, 30, 63, 94).
[85] M. Brandbyge, J.-L. Mozos, P. Ordejón, J. Taylor, and K. Stokbro. Density-functional method for nonequilibrium electron transport. *Phys. Rev. B* 65, 165401 (2002) (see pp. 24, 63, 94).
[86] N. Papior, N. Lorente, T. Frederiksen, A. García, and M. Brandbyge. Improvements on non-equilibrium and transport Green function techniques: The next-generation transiesta. *Comput. Phys. Commun.* 212, 8 (2017) (see p. 24).
[87] M. P. López Sancho, J. M. López Sancho, and J. Rubio. Quick iterative scheme for the calculation of transfer matrices: application to Mo (100). *J. Phys. F* 14, 1205 (1984) (see pp. 24, 45).
[88] M. P. López Sancho, J. M. López Sancho, and J. Rubio. Highly convergent schemes for the calculation of bulk and surface Green functions. *J. Phys. F* 15, 851 (1985) (see p. 24).
[89] M. P. López Sancho, J. M. López Sancho, and J. Rubio. A nonorthogonal-basis calculation of the spectral density of surface states for the (100) and (110) faces of tungsten. *J. Phys. C* 18, 1803 (1985) (see p. 24).
[90] M. Thoss and F. Evers. Perspective: Theory of quantum transport in molecular junctions. *J. Chem. Phys.* 148, 030901 (2018) (see p. 25).
[91] S. Kurth and G. Stefanucci. Transport through correlated systems with density functional theory. *J. Phys. Condens. Matter* 29, 413002 (2017) (see pp. 25–27).
[92] H. B. Akkerman and B. de Boer. Electrical conduction through single molecules and self-assembled monolayers. *J. Phys. Condens. Matter* 20, 013001 (2007) (see p. 26).
[93] T. Yelin, R. Korytár, N. Sukenik, R. Vardimon, B. Kumar, C. Nuckolls, F. Evers, and O. Tal. Conductance saturation in a series of highly transmitting molecular junctions. *Nat. Mater.* 15, 444 (2016) (see p. 26).
[94] J. F. Janak. Proof that $\frac{\partial E}{\partial n_i} = \epsilon$ in density-functional theory. *Phys. Rev. B* 18, 7165 (1978) (see p. 26).

[95] H. Mera, K. Kaasbjerg, Y. M. Niquet, and G. Stefanucci. Assessing the accuracy of Kohn-Sham conductances using the Friedel sum rule. *Phys. Rev. B* 81, 035110 (2010) (see p. 26).

[96] G. Stefanucci and S. Kurth. Towards a Description of the Kondo Effect Using Time-Dependent Density-Functional Theory. *Phys. Rev. Lett.* 107, 216401 (2011) (see p. 26).

[97] J. P. Bergfield, Z.-F. Liu, K. Burke, and C. A. Stafford. Bethe Ansatz Approach to the Kondo Effect within Density-Functional Theory. *Phys. Rev. Lett.* 108, 066801 (2012) (see p. 26).

[98] P. Tröster, P. Schmitteckert, and F. Evers. Transport calculations based on density functional theory, Friedel's sum rule, and the Kondo effect. *Phys. Rev. B* 85, 115409 (2012) (see p. 26).

[99] P. Schmitteckert and F. Evers. Exact Ground State Density-Functional Theory for Impurity Models Coupled to External Reservoirs and Transport Calculations. *Phys. Rev. Lett.* 100, 086401 (2008) (see p. 26).

[100] N. Sai, M. Zwolak, G. Vignale, and M. di Ventra. Dynamical Corrections to the DFT-LDA Electron Conductance in Nanoscale Systems. *Phys. Rev. Lett.* 94, 186810 (2005) (see p. 26).

[101] L. Hedin. New Method for Calculating the One-Particle Green's Function with Application to the Electron-Gas Problem. *Phys. Rev.* 139, A796 (1965) (see p. 27).

[102] P. Darancet, A. Ferretti, D. Mayou, and V. Olevano. Ab initio *GW* electron-electron interaction effects in quantum transport. *Phys. Rev. B* 75, 075102 (2007) (see p. 27).

[103] S. Liu, A. Nurbawono, and C. Zhang. Density Functional Theory for Steady-State Nonequilibrium Molecular Junctions. *Sci. Rep.* 5, 15386 (2015) (see p. 27).

[104] P. Delaney and J. C. Greer. Correlated Electron Transport in Molecular Electronics. *Phys. Rev. Lett.* 93, 036805 (2004) (see p. 27).

[105] Q. Sun and G. K.-L. Chan. Quantum Embedding Theories. *Acc. Chem. Res.* 49, 2705 (2016) (see p. 28).

[106] J. E. Inglesfield. *The Embedding Method for Electronic Structure* (IOP Publishing, Bristol, 2015) (see p. 28).

[107] G. Kotliar, S. Y. Savrasov, K. Haule, V. S. Oudovenko, O. Parcollet, and C. A. Marianetti. Electronic structure calculations with dynamical mean-field theory. *Rev. Mod. Phys.* 78, 865 (2006) (see p. 28).

[108] M. Rumetshofer, D. Bauernfeind, E. Arrigoni, and W. von der Linden. First-principles quantum transport simulation of CuPc on Au(111) and Ag(111). *Phys. Rev. B* 99, 045148 (2019) (see pp. 29, 35, 59).

[109] F. Aryasetiawan, K. Karlsson, O. Jepsen, and U. Schönberger. Calculations of Hubbard U from first-principles. *Phys. Rev. B* 74, 125106 (2006) (see p. 32).

[110] M. Karolak, G. Ulm, T. Wehling, V. Mazurenko, A. Poteryaev, and A. Lichtenstein. Double counting in LDA + DMFT—The example of NiO. *J. Electron Spectrosc.* 181, 11 (2010) (see p. 33).

[111] K. Haule. Exact Double Counting in Combining the Dynamical Mean Field Theory and the Density Functional Theory. *Phys. Rev. Lett.* 115, 196403 (2015) (see p. 33).

[112] M. Caffarel and W. Krauth. Exact diagonalization approach to correlated fermions in infinite dimensions: Mott transition and superconductivity. *Phys. Rev. Lett.* 72, 1545 (1994) (see p. 33).
[113] K. G. Wilson. The renormalization group: Critical phenomena and the Kondo problem. *Rev. Mod. Phys.* 47, 773 (1975) (see pp. 33, 37).
[114] S. R. White. Density matrix formulation for quantum renormalization groups. *Phys. Rev. Lett.* 69, 2863 (1992) (see pp. 33, 35).
[115] N. S. Wingreen and Y. Meir. Anderson model out of equilibrium: Noncrossing-approximation approach to transport through a quantum dot. *Phys. Rev. B* 49, 11040 (1994) (see p. 33).
[116] A. A. Aligia. Nonequilibrium magnetotransport through a quantum dot: An interpolative perturbative approach. *Phys. Rev. B* 74, 155125 (2006) (see p. 33).
[117] P. Werner, A. Comanac, L. de'Medici, M. Troyer, and A. J. Millis. Continuous-Time Solver for Quantum Impurity Models. *Phys. Rev. Lett.* 97, 076405 (2006) (see pp. 33, 84).
[118] M. Zingl, M. Nuss, D. Bauernfeind, and M. Aichhorn. A real-frequency solver for the Anderson impurity model based on bath optimization and cluster perturbation theory. *Physica B* 536, 254 (2018) (see p. 33).
[119] G. J. Kraberger. Development of a full matrix ab-initio scheme for materials with strong spin-orbit coupling and Coulomb interactions. PhD thesis (Graz University of Technology, Austria, 2018) (see p. 34).
[120] P. Seth, I. Krivenko, M. Ferrero, and O. Parcollet. TRIQS/CTHYB: A continuous-time quantum Monte Carlo hybridisation expansion solver for quantum impurity problems. *Comput. Phys. Commun.* 200, 274 (2016) (see pp. 34, 84).
[121] L. Kouwenhoven and L. Glazman. Revival of the Kondo effect. *Phys. World* 14, 33 (2001) (see pp. 37, 39).
[122] W. de Haas, J. de Boer, and G. van dën Berg. The electrical resistance of gold, copper and lead at low temperatures. *Physica* 1, 1115 (1934) (see p. 37).
[123] P. W. Anderson and G. Yuval. Exact Results in the Kondo Problem: Equivalence to a Classical One-Dimensional Coulomb Gas. *Phys. Rev. Lett.* 23, 89 (1969) (see pp. 37, 41).
[124] N. Andrei. Diagonalization of the Kondo Hamiltonian. *Phys. Rev. Lett.* 45, 379 (1980) (see p. 37).
[125] P. B. Wiegmann. Exact solution of the s-d exchange model (Kondo problem). *J. Phys. C* 14, 1463 (1981) (see p. 37).
[126] H. Bethe. Zur Theorie der Metalle. *Z. Phys.* 71, 205 (1931) (see p. 37).
[127] I. Affleck, L. Borda, and H. Saleur. Friedel oscillations and the Kondo screening cloud. *Phys. Rev. B* 77, 180404 (2008) (see pp. 38, 61).
[128] Y.-S. Fu, S.-H. Ji, X. Chen, X.-C. Ma, R. Wu, C.-C. Wang, W.-H. Duan, X.-H. Qiu, B. Sun, P. Zhang, J.-F. Jia, and Q.-K. Xue. Manipulating the Kondo Resonance through Quantum Size Effects. *Phys. Rev. Lett.* 99, 256601 (2007) (see pp. 38, 61).
[129] A. A. Abrikosov. Electron scattering on magnetic impurities in metals and anomalous resistivity effects. *Physics Physique Fizika* 2, 5 (1965) (see p. 38).

[130] H. Suhl. Dispersion Theory of the Kondo Effect. *Phys. Rev.* 138, A515 (1965) (see p. 38).
[131] J. R. Schrieffer and P. A. Wolff. Relation between the Anderson and Kondo Hamiltonians. *Phys. Rev.* 149, 491 (1966) (see p. 40).
[132] P. W. Anderson. A poor man's derivation of scaling laws for the Kondo problem. *J. Phys. C* 3, 2436 (1970) (see p. 41).
[133] F. D. M. Haldane. Scaling Theory of the Asymmetric Anderson Model. *Phys. Rev. Lett.* 40, 416 (1978) (see pp. 42, 84).
[134] P. Jarillo-Herrero, J. Kong, H. S. J. van der Zant, C. Dekker, L. P. Kouwenhoven, and S. de Franceschi. Orbital Kondo effect in carbon nanotubes. *Nature* 434, 484 (2005) (see p. 42).
[135] L. Borda, G. Zaránd, W. Hofstetter, B. I. Halperin, and J. von Delft. SU(4) Fermi Liquid State and Spin Filtering in a Double Quantum Dot System. *Phys. Rev. Lett.* 90, 026602 (2003) (see p. 42).
[136] M. Eto. Enhancement of Kondo Effect in Multilevel Quantum Dots. *J. Phys. Soc. Jpn.* 74, 95 (2005) (see pp. 42, 69).
[137] A. L. Chudnovskiy. SU (4) vs. SU (2) Kondo effect in double quantum dot. *EPL* 71, 672 (2005) (see pp. 42, 69).
[138] A. J. Keller, S. Amasha, I. Weymann, C. P. Moca, I. G. Rau, J. A. Katine, H. Shtrikman, G. Zaránd, and D. Goldhaber-Gordon. Emergent SU(4) Kondo physics in a spin–charge-entangled double quantum dot. *Nat. Phys.* 10, 145 (2013) (see p. 42).
[139] M. Filippone, C. P. Moca, G. Zaránd, and C. Mora. Kondo temperature of SU(4) symmetric quantum dots. *Phys. Rev. B* 90, 121406 (2014) (see pp. 42, 69, 84).
[140] W. R. French, C. R. Iacovella, I. Rungger, A. M. Souza, S. Sanvito, and P. T. Cummings. Atomistic simulations of highly conductive molecular transport junctions under realistic conditions. *Nanoscale* 5, 3654 (2013) (see pp. 43, 54).
[141] Z. Qian, R. Li, S. Hou, Z. Xue, and S. Sanvito. An efficient nonequilibrium Green's function formalism combined with density functional theory approach for calculating electron transport properties of molecular devices with quasi-one-dimensional electrodes. *J. Chem. Phys.* 127, 194710 (2007) (see p. 43).
[142] P. Z. Coura, S. B. Legoas, A. S. Moreira, F. Sato, V. Rodrigues, S. O. Dantas, D. Ugarte, and D. S. Galvão. On the Structural and Stability Features of Linear Atomic Suspended Chains Formed from Gold Nanowires Stretching. *Nano Lett.* 4, 1187 (2004) (see p. 43).
[143] A. I. Yanson, G. R. Bollinger, H. E. van den Brom, N. Agrait, and J. M. van Ruitenbeek. Formation and manipulation of a metallic wire of single gold atoms. *Nature* 395, 783 (1998) (see p. 43).
[144] H. Ohnishi, Y. Kondo, and K. Takayanagi. Quantized conductance through individual rows of suspended gold atoms. *Nature* 395, 780 (1998) (see p. 43).
[145] I. Baldea. Important issues facing model-based approaches to tunneling transport in molecular junctions. *Phys. Chem. Chem. Phys.* 17, 20217 (2015) (see pp. 43, 54).

[146] M. Rumetshofer, G. Dorn, L. Boeri, E. Arrigoni, and W. von der Linden. First-principles molecular transport calculation for the benzenedithiolate molecule. *New J. Phys.* 19, 103007 (2017) (see p. 43).

[147] P. Giannozzi, S. Baroni, N. Bonini, M. Calandra, R. Car, C. Cavazzoni, D. Ceresoli, G. L. Chiarotti, M. Cococcioni, I. Dabo, A. Dal Corso, S. de Gironcoli, S. Fabris, G. Fratesi, R. Gebauer, U. Gerstmann, C. Gougoussis, A. Kokalj, M. Lazzeri, L. Martin-Samos, N. Marzari, F. Mauri, R. Mazzarello, S. Paolini, A. Pasquarello, L. Paulatto, C. Sbraccia, S. Scandolo, G. Sclauzero, A. P. Seitsonen, A. Smogunov, P. Umari, and R. M. Wentzcovitch. QUANTUM ESPRESSO: a modular and open-source software project for quantum simulations of materials. *J. Phys. Condens. Matter* 21, 395502 (2009) (see pp. 44, 94).

[148] A. Kokalj. Computer graphics and graphical user interfaces as tools in simulations of matter at the atomic scale. *Comput. Mater. Sci.* 28, 155 (2003) (see pp. 44, 60, 62, 70).

[149] J. P. Perdew and A. Zunger. Self-interaction correction to density-functional approximations for many-electron systems. *Phys. Rev. B* 23, 5048 (1981) (see p. 44).

[150] A. D. Corso. Pseudopotentials periodic table: From H to Pu. *Comput. Mater. Sci.* 95, 337 (2014) (see p. 44).

[151] A. Calzolari, N. Marzari, I. Souza, and M. Buongiorno Nardelli. *Ab initio* transport properties of nanostructures from maximally localized Wannier functions. *Phys. Rev. B* 69, 035108 (2004) (see p. 44).

[152] M. Shelley, N. Poilvert, A. A. Mostofi, and N. Marzari. Automated quantum conductance calculations using maximally-localised Wannier functions. *Comput. Phys. Commun.* 182, 2174 (2011) (see p. 44).

[153] D. A. Ryndyk, A. Donarini, M. Grifoni, and K. Richter. Many-body localized molecular orbital approach to molecular transport. *Phys. Rev. B* 88, 085404 (2013) (see pp. 45, 57, 58).

[154] G. Sclauzero, A. Dal Corso, and A. Smogunov. Interaction of CO with an Au monatomic chain at different strains: Electronic structure and ballistic transport. *Phys. Rev. B* 85, 165411 (2012) (see p. 46).

[155] K. Momma and F. Izumi. *VESTA3* for three-dimensional visualization of crystal, volumetric and morphology data. *J. Appl. Crystallogr.* 44, 1272 (2011) (see pp. 48, 51).

[156] L. A. Zotti, T. Kirchner, J. C. Cuevas, F. Pauly, T. Huhn, E. Scheer, and A. Erbe. Revealing the Role of Anchoring Groups in the Electrical Conduction Through Single-Molecule Junctions. *Small* 6, 1529 (2010) (see p. 49).

[157] T. Rangel, G.-M. Rignanese, and V. Olevano. Can molecular projected density of states (PDOS) be systematically used in electronic conductance analysis? *Beilstein J. Nanotechnol.* 6, 1247 (2015) (see p. 49).

[158] G. Sclauzero, A. Dal Corso, A. Smogunov, and E. Tosatti. Interaction of a CO molecule with a Pt monatomic wire: Electronic structure and ballistic conductance. *Phys. Rev. B* 78, 085421 (2008) (see p. 50).

[159] G. Cuniberti, G. Fagas, and K. Richter. Fingerprints of mesoscopic leads in the conductance of a molecular wire. *Chem. Phys.* 281, 465 (2002) (see p. 52).
[160] G. Cuniberti, F. Großmann, and R. Gutiérrez. The Role of Contacts in Molecular Electronics. In: *Advances in Solid State Physics* (ed B. Kramer) 42 (Springer, Berlin, Heidelberg, 2002) (see p. 52).
[161] C. J. O. Verzijl, J. S. Seldenthuis, and J. M. Thijssen. Applicability of the wide-band limit in DFT-based molecular transport calculations. *J. Chem. Phys.* 138, 094102 (2013) (see p. 52).
[162] L. van Hove. The Occurrence of Singularities in the Elastic Frequency Distribution of a Crystal. *Phys. Rev.* 89, 1189 (1953) (see p. 52).
[163] N. Sergueev, L. Tsetseris, K. Varga, and S. Pantelides. Configuration and conductance evolution of benzene-dithiol molecular junctions under elongation. *Phys. Rev. B* 82, 073106 (2010) (see p. 54).
[164] R. J. Bursill, C. Castleton, and W. Barford. Optimal parametrisation of the Pariser–Parr–Pople Model for benzene and biphenyl. *Chem. Phys. Lett.* 294, 305 (1998) (see p. 57).
[165] J. B. Neaton, M. S. Hybertsen, and S. G. Louie. Renormalization of Molecular Electronic Levels at Metal-Molecule Interfaces. *Phys. Rev. Lett.* 97, 216405 (2006) (see p. 57).
[166] M. Nuss, G. Dorn, A. Dorda, W. von der Linden, and E. Arrigoni. Master equation based steady-state cluster perturbation theory. *Phys. Rev. B* 92, 125128 (2015) (see p. 57).
[167] J. van den Brink and A. F. Morpurgo. Magnetic blue. *Nature* 450, 177 (2007) (see p. 59).
[168] T. Schwieger, H. Peisert, M. S. Golden, M. Knupfer, and J. Fink. Electronic structure of the organic semiconductor copper phthalocyanine and K-CuPc studied using photoemission spectroscopy. *Phys. Rev. B* 66, 155207 (2002) (see p. 59).
[169] V. Aristov, O. Molodtsova, V. Maslyuk, D. Vyalikh, V. Zhilin, Y. Ossipyan, T. Bredow, I. Mertig, and M. Knupfer. Electronic structure of pristine CuPc: Experiment and calculations. *Appl. Surf. Sci.* 254, 20 (2007) (see p. 59).
[170] N. Marom, X. Ren, J. E. Moussa, J. R. Chelikowsky, and L. Kronik. Electronic structure of copper phthalocyanine from G_0W_0 calculations. *Phys. Rev. B* 84, 195143 (2011) (see p. 59).
[171] G. V. Nazin, X. H. Qiu, and W. Ho. Visualization and Spectroscopy of a Metal-Molecule-Metal Bridge. *Science* 302, 77 (2003) (see p. 59).
[172] A. Calzolari, A. Ferretti, and M. B. Nardelli. Ab initio correlation effects on the electronic and transport properties of metal(II)-phthalocyanine-based devices. *Nanotechnology* 18, 424013 (2007) (see p. 59).
[173] M. M. Fadlallah, U. Eckern, A. H. Romero, and U. Schwingenschlögl. Electronic transport properties of (fluorinated) metal phthalocyanine. *New J. Phys.* 18, 013003 (2016) (see p. 59).

[174] A. Zhao, Q. Li, L. Chen, H. Xiang, W. Wang, S. Pan, B. Wang, X. Xiao, J. Yang, J. G. Hou, and Q. Zhu. Controlling the Kondo Effect of an Adsorbed Magnetic Ion Through Its Chemical Bonding. *Science* 309, 1542 (2005) (see p. 59).

[175] Z. Hu, B. Li, A. Zhao, J. Yang, and J. G. Hou. Electronic and Magnetic Properties of Metal Phthalocyanines on Au(111) Surface: A First-Principles Study. *J. Phys. Chem. C* 112, 13650 (2008) (see p. 59).

[176] S. Stepanow, A. Mugarza, G. Ceballos, P. Moras, J. C. Cezar, C. Carbone, and P. Gambardella. Giant spin and orbital moment anisotropies of a Cu-phthalocyanine monolayer. *Phys. Rev. B* 82, 014405 (2010) (see p. 59).

[177] S. Stepanow, P. S. Miedema, A. Mugarza, G. Ceballos, P. Moras, J. C. Cezar, C. Carbone, F. M. F. de Groot, and P. Gambardella. Mixed-valence behavior and strong correlation effects of metal phthalocyanines adsorbed on metals. *Phys. Rev. B* 83, 220401 (2011) (see p. 59).

[178] K. J. Franke, G. Schulze, and J. I. Pascual. Competition of Superconducting Phenomena and Kondo Screening at the Nanoscale. *Science* 332, 940 (2011) (see p. 59).

[179] A. Strozecka, M. Soriano, J. I. Pascual, and J. J. Palacios. Reversible Change of the Spin State in a Manganese Phthalocyanine by Coordination of CO Molecule. *Phys. Rev. Lett.* 109, 147202 (2012) (see p. 59).

[180] E. Salomon, P. Amsalem, N. Marom, M. Vondracek, L. Kronik, N. Koch, and T. Angot. Electronic structure of CoPc adsorbed on Ag(100): Evidence for molecule-substrate interaction mediated by Co 3*d* orbitals. *Phys. Rev. B* 87, 075407 (2013) (see p. 59).

[181] D. Jacob, M. Soriano, and J. J. Palacios. Kondo effect and spin quenching in high-spin molecules on metal substrates. *Phys. Rev. B* 88, 134417 (2013) (see p. 59).

[182] E. Minamitani, N. Tsukahara, D. Matsunaka, Y. Kim, N. Takagi, and M. Kawai. Symmetry-Driven Novel Kondo Effect in a Molecule. *Phys. Rev. Lett.* 109, 086602 (2012) (see p. 59).

[183] J. Kügel, M. Karolak, A. Krönlein, J. Senkpiel, P.-J. Hsu, G. Sangiovanni, and M. Bode. State identification and tunable Kondo effect of MnPc on Ag(001). *Phys. Rev. B* 91, 235130 (2015) (see p. 59).

[184] R. Hiraoka, E. Minamitani, R. Arafune, N. Tsukahara, S. Watanabe, M. Kawai, and N. Takagi. Single-molecule quantum dot as a Kondo simulator. *Nat. Commun.* 8, 16012 (2017) (see p. 59).

[185] J. Kügel, M. Karolak, A. Krönlein, D. Serrate, M. Bode, and G. Sangiovanni. Reversible magnetic switching of high-spin molecules on a giant Rashba surface. *npj Quantum Mater.* 3, 53 (2018) (see p. 59).

[186] J. M. Gottfried. Surface chemistry of porphyrins and phthalocyanines. *Surf. Sci. Rep.* 70, 259 (2015) (see p. 59).

[187] E. Wruss, G. Prokopiou, L. Kronik, E. Zojer, O. T. Hofmann, and D. A. Egger. Magnetic configurations of open-shell molecules on metals: The case of CuPc and CoPc on silver. *Phys. Rev. Mater.* 3, 086002 (2019) (see p. 59).

[188] R. Korytár and N. Lorente. Multi-orbital non-crossing approximation from maximally localized Wannier functions: the Kondo signature of copper phthalocyanine on Ag(100). *J. Phys. Condens. Matter* 23, 355009 (2011) (see pp. 60–62, 66, 69).

[189] I. Affleck and P. Simon. Detecting the Kondo Screening Cloud Around a Quantum Dot. *Phys. Rev. Lett.* 86, 2854 (2001) (see p. 61).

[190] J. Park, S.-S. B. Lee, Y. Oreg, and H.-S. Sim. How to Directly Measure a Kondo Cloud's Length. *Phys. Rev. Lett.* 110, 246603 (2013) (see p. 61).

[191] J. Heyd, G. E. Scuseria, and M. Ernzerhof. Hybrid functionals based on a screened Coulomb potential. *J. Chem. Phys.* 118, 8207 (2003) (see p. 61).

[192] A. Mugarza, N. Lorente, P. Ordejón, C. Krull, S. Stepanow, M.-L. Bocquet, J. Fraxedas, G. Ceballos, and P. Gambardella. Orbital Specific Chirality and Homochiral Self-Assembly of Achiral Molecules Induced by Charge Transfer and Spontaneous Symmetry Breaking. *Phys. Rev. Lett.* 105, 115702 (2010) (see p. 62).

[193] J. P. Perdew, K. Burke, and M. Ernzerhof. Generalized Gradient Approximation Made Simple. *Phys. Rev. Lett.* 77, 3865 (1996) (see pp. 63, 94).

[194] R. Bulla, T. A. Costi, and T. Pruschke. Numerical renormalization group method for quantum impurity systems. *Rev. Mod. Phys.* 80, 395 (2008) (see p. 63).

[195] F. A. Wolf, I. P. McCulloch, and U. Schollwöck. Solving nonequilibrium dynamical mean-field theory using matrix product states. *Phys. Rev. B* 90, 235131 (2014) (see p. 63).

[196] W. von der Linden, R. Preuss, and V. Dose. The Prior-Predictive Value: A Paradigm of Nasty Multi-Dimensional Integrals. In: *Maximum Entropy and Bayesian Methods* (eds W. von der Linden, V. Dose, R. Fischer, and R. Preuss) (Springer, Dordrecht, 1999) (see pp. 63, 84, 88).

[197] J. Skilling. Fundamentals of MaxEnt in data analysis. In: *Maximum Entropy in Action* (eds B. Buck and V. Macaulay) (Clarendon Press, Oxford, 1991) (see pp. 63, 84, 88).

[198] M.-S. Liao and S. Scheiner. Electronic structure and bonding in metal phthalocyanines, Metal=Fe, Co, Ni, Cu, Zn, Mg. *J. Chem. Phys.* 114, 9780 (2001) (see p. 64).

[199] S. L. Dudarev, G. A. Botton, S. Y. Savrasov, C. J. Humphreys, and A. P. Sutton. Electron-energy-loss spectra and the structural stability of nickel oxide: An LSDA+U study. *Phys. Rev. B* 57, 1505 (1998) (see p. 66).

[200] P. Wahl, L. Diekhöner, M. A. Schneider, and K. Kern. Background removal in scanning tunneling spectroscopy of single atoms and molecules on metal surfaces. *Rev. Sci. Instrum.* 79, 043104 (2008) (see p. 70).

[201] A. Ferris-Prabhu and D. Withers. Numerical analytic continuation using Padé approximants. *J. Comput. Phys.* 13, 94 (1973) (see p. 75).

[202] L.-F. Arsenault, R. Neuberg, L. A. Hannah, and A. J. Millis. Projected regression method for solving Fredholm integral equations arising in the analytic continuation problem of quantum physics. *Inverse Probl.* 33, 115007 (2017) (see p. 75).

[203] S. R. White. *Computer Simulation Studies in Condensed Matter Physics III* (eds D. P. Landau, K. K. Mon, and H.-B. Schüttler) (Springer, Berlin, 1991) (see p. 75).
[204] A. W. Sandvik. Stochastic method for analytic continuation of quantum Monte Carlo data. *Phys. Rev. B* 57, 10287 (1998) (see p. 75).
[205] A. S. Mishchenko, N. V. Prokof'ev, A. Sakamoto, and B. V. Svistunov. Diagrammatic quantum Monte Carlo study of the Fröhlich polaron. *Phys. Rev. B* 62, 6317 (2000) (see p. 75).
[206] K. S. D. Beach. Identifying the maximum entropy method as a special limit of stochastic analytic continuation. *ArXiv e-prints.* arXiv:cond-mat/0403055 (2004) (see p. 75).
[207] S. Fuchs, T. Pruschke, and M. Jarrell. Analytic continuation of quantum Monte Carlo data by stochastic analytical inference. *Phys. Rev. E* 81, 056701 (2010) (see p. 75).
[208] A. W. Sandvik. Constrained sampling method for analytic continuation. *Phys. Rev. E* 94, 063308 (2016) (see p. 75).
[209] K. Ghanem. Stochastic Analytic Continuation: A Bayesian Approach. PhD thesis (RWTH Aachen University, Germany, 2017) (see pp. 75, 77).
[210] R. N. Silver, D. S. Sivia, and J. E. Gubernatis. Maximum-entropy method for analytic continuation of quantum Monte Carlo data. *Phys. Rev. B* 41, 2380 (1990) (see p. 75).
[211] J. E. Gubernatis, M. Jarrell, R. N. Silver, and D. S. Sivia. Quantum Monte Carlo simulations and maximum entropy: Dynamics from imaginary-time data. *Phys. Rev. B* 44, 6011 (1991) (see p. 75).
[212] S. F. Gull and J. Skilling. Maximum entropy method in image processing. *IEE Proc. F (Communications, Radar and Signal Processing)* 131, 646 (1984) (see pp. 75, 77).
[213] F. Bao, Y. Tang, M. Summers, G. Zhang, C. Webster, V. Scarola, and T. A. Maier. Fast and efficient stochastic optimization for analytic continuation. *Phys. Rev. B* 94, 125149 (2016) (see p. 75).
[214] G. J. Kraberger, R. Triebl, M. Zingl, and M. Aichhorn. Maximum entropy formalism for the analytic continuation of matrix-valued Green's functions. *Phys. Rev. B* 96, 155128 (2017) (see p. 75).
[215] W. Metzner and D. Vollhardt. Correlated Lattice Fermions in $d = \infty$ Dimensions. *Phys. Rev. Lett.* 62, 324 (1989) (see p. 76).
[216] A. Georges and G. Kotliar. Hubbard model in infinite dimensions. *Phys. Rev. B* 45, 6479 (1992) (see p. 76).
[217] M. Rumetshofer, D. Bauernfeind, and W. von der Linden. Bayesian parametric analytic continuation of Green's functions. *Phys. Rev. B* 100, 075137 (2019) (see p. 76).
[218] J. Skilling. Classic Maximum Entropy. In: *Maximum Entropy and Bayesian Methods* (ed J. Skilling) (Springer, Dordrecht, 1989) (see p. 77).
[219] S. F. Gull and G. J. Daniell. Image reconstruction from incomplete and noisy data. *Nature* 272, 686 (1978) (see p. 77).

[220] S. F. Gull. Developments in Maximum Entropy Data Analysis. In: *Maximum Entropy and Bayesian Methods* (ed J. Skilling) (Springer, Dordrecht, 1989) (see p. 77).

[221] R. Fischer, W. von der Linden, and V. Dose. On the Importance of α Marginalization in Maximum Entropy. In: *Maximum Entropy and Bayesian Methods* (eds K. M. Hanson and R. N. Silver) (Springer, Dordrecht, 1996) (see p. 77).

[222] R. K. Bryan. Solving oversampled data problems by maximum entropy. In: *Maximum Entropy and Bayesian Methods* (ed P. F. Fougère) (Springer, Dordrecht, 1990) (see p. 77).

[223] J. Skilling. Nested sampling for general Bayesian computation. *Bayesian Anal.* 1, 833 (2006) (see p. 81).

[224] R. W. Henderson and P. M. Goggans. Parallelized nested sampling. *AIP Conf. Proc.* 1636, 100 (2014) (see p. 83).

[225] J. Skilling. Bayesian computation in big spaces-nested sampling and Galilean Monte Carlo. *AIP Conf. Proc.* 1443, 145 (2012) (see p. 83).

[226] S. Martiniani, J. D. Stevenson, D. J. Wales, and D. Frenkel. Superposition Enhanced Nested Sampling. *Phys. Rev. X* 4, 031034 (2014) (see p. 83).

[227] O. Parcollet, M. Ferrero, T. Ayral, H. Hafermann, I. Krivenko, L. Messio, and P. Seth. TRIQS: A toolbox for research on interacting quantum systems. *Comput. Phys. Commun.* 196, 398 (2015) (see p. 84).

[228] E. Koch. Analytic Continuation of Quantum Monte Carlo Data. In: *DMFT: From Infinite Dimensions to Real Materials* (eds E. Pavarini, E. Koch, A. Lichtenstein, and D. Vollhardt) 8 (Forschungszentrum Jülich, Jülich, 2018) (see p. 89).

[229] N. Troullier and J. L. Martins. Efficient pseudopotentials for plane-wave calculations. *Phys. Rev. B* 43, 1993 (1991) (see p. 94).

[230] P. Rivero, V. M. García-Suárez, D. Pereñiguez, K. Utt, Y. Yang, L. Bellaiche, K. Park, J. Ferrer, and S. Barraza-Lopez. Systematic pseudopotentials from reference eigenvalue sets for DFT calculations. *Comput. Mater. Sci.* 98, 372 (2015) (see p. 94).

[231] K. Binder. Introduction: Theory and "Technical" Aspects of Monte Carlo Simulations. In: *Monte Carlo Methods in Statistical Physics* (ed K. Binder) (Springer, Berlin, Heidelberg, 1986) (see p. 95).

[232] Y. Ogata. A Monte Carlo method for high dimensional integration. *Numer. Math.* 55, 137 (1989) (see p. 95).

[233] W. Romberg. *Vereinfachte numerische Integration* (F. Bruns Bokhandel, Trondheim, 1955) (see p. 95).